Title
Calibrated Ocean Bottom Pressure Measurements for Marine Geodesy

Author
Cook, Matthew James

Publication Date
2019

UNIVERSITY OF CALIFORNIA SAN DIEGO

Calibrated Ocean Bottom Pressure Measurements for Marine Geodesy

A dissertation submitted in partial satisfaction of the requirements for the degree
Doctor of Philosophy

in

Earth Sciences

by

Matthew James Cook

Committee in charge:

Mark Zumberge, Chair
Adrian Borsa
Robert Pinkel
David Sandwell
Glenn Sasagawa
Michael Todd

2019

The dissertation of Matthew James Cook is approved, and it is acceptable in quality and form for publication on microfilm and electronically:

Chair

University of California San Diego

2019

DEDICATION

For my family.

EPIGRAPH

Nobody ever figures out what life is all about, and it doesn't matter. Explore the world.

Nearly everything is really interesting if you go into it deeply enough.

– Richard Feynman

TABLE OF CONTENTS

LIST OF FIGURES

LIST OF TABLES

ACKNOWLEDGEMENTS

There is an enormous number of people that have made my experience at SIO wonderful and deserve thanks. While there are too many individuals to personally thank, all of their contributions in various forms have been greatly appreciated.

I am especially grateful to my advisor, Mark Zumberge, for the last six years. Mark has provided a tremendous amount of unwavering support, guidance, encouragement, and valuable research opportunities to ensure my success. I have grown academically and professionally under his mentorship.

I also thank Glenn Sasagawa for the significant amounts of time that he has spent providing technical and logistical assistance, conversations about life and research, and memorable quips. The other members of my committee, Adrian Borsa, Robert Pinkel, David Sandwell, and Michael Todd, have provided valuable advice, assistance, and conversations throughout the last several years, which I thank them for.

I thank the faculty, researchers, administrative staff, graduate office, and IT support at IGPP, SIO, and UCSD for their contributions to the success of myself and others.

During the course of my time here, I have had opportunities to teach and work on exciting research projects. I thank Geoff Cook, Kerry Key, Gabi Laske, and Anne Pommier for the opportunities to serve as a TA and develop my teaching skills. I would like to thank the University of Washington cohort of William Wilcock, David Schmidt, Emily Roland, Dana Manalang, Ken Feldman, and Erik Frederickson for their recurring help with calibrated pressure measurements in Cascadia and at Axial Seamount; William Chadwick and Scott Nooner for multiple opportunities to assist in pressure surveys at Axial Seamount in 2017 and 2018; and Bruce Appelgate for his help coordinating my UC Ship Funds Cruise.

I extend special thanks to my first-year cohort - John DeSanto, Adrian Doran, Dara Goldberg, Jessie Saunders, Wei Wang, and Yongfei Wang. We have spent an enormous amount of time together in tough times and good at SIO and all of it for the better. I would also like to thank Dara Goldberg for being a wonderful officemate for five years and Jessie Saunders for being a wonderful housemate for several years. I would also like to thank Wesley Neely, Susheel Adusumilli, Soli Garcia, Joe Kehrwald, Austen Michalak, and the group of SIO and IGPP surfers for all of the help, support, and good times both at and outside of SIO.

Finally, I would like to thank my entire family. Most of all, I thank my parents, Hank and Connie Strause, and my siblings, Andy, Anna, and Ryan, for all of the love, support, and encouragement from the beginning.

Chapter 3, in part, was published in IEEE Access: Sasagawa, G. S., M. A. Zumberge, and M. J. Cook (2018), Laboratory Simulation and Measurement of Instrument Drift in Quartz-Resonant Pressure Gauges, *IEEE Access*, 6, 57334-57340, https://doi.org/10.1109/ACCESS.2018.2873479. The dissertation author is a contributing investigator and author of this paper.

Chapter 4, in part, is a reformatted version of a publication in Earth and Space Science: Sasagawa, G., M. J. Cook, and M. A. Zumberge (2016), Drift-corrected seafloor pressure observations of vertical deformation at Axial Seamount 2013–2014, *Earth and Space Science*, 3(9), 381-385, https://doi.org/10.1002/2016EA000190. The dissertation author is not the primary investigator and author of this paper. Chapter 4, in another part, is currently being prepared for submission for publication. This work is coauthored with Mark Zumberge and Glenn Sasagawa. The dissertation author is a contributing investigator and author of this material.

Chapter 5, in full, is currently being prepared for submission for publication as Cook, M. J., G. S. Sasagawa, D. A. Schmidt, E. C. Roland, W. S. D. Wilcock, and M. A. Zumberge, Absolute Calibrated Seafloor Pressure Measurements for Geodesy in Cascadia, *in preparation*. The dissertation author is the primary investigator and author of this material.

Chapter 6, in part, is currently in revision for publication in Earth and Space Science as: Cook, M. J., and J. B. DeSanto (2019), Validation of geodetic seafloor benchmark stability using structure-from-motion and seafloor pressure data, *Earth and Space Science*, *in revision*. The dissertation author is the primary investigator and author of this material.

VITA

2013	B. S. in Physics, University of California Santa Barbara
2015	M. S. in Earth Sciences, University of California San Diego
2019	Ph. D. in Earth Sciences, University of California San Diego

PUBLICATIONS

Cook, M. J., G. S. Sasagawa, and M. A. Zumberge, Real-time drift-corrected seafloor pressure measurements for volcanic deformation monitoring at Axial Seamount, *in preparation*.

Cook, M. J., G. S. Sasagawa, D. A. Schmidt, E. C. Roland, W. S. D. Wilcock, and M. A. Zumberge, Absolute Calibrated Seafloor Pressure Measurements for Geodesy in Cascadia, *in preparation*.

Cook, M. J., and J. B. DeSanto (2019), Validation of geodetic seafloor benchmark stability using structure-from-motion and seafloor pressure data, *Earth and Space Science*, *in revision*.

Sasagawa, G. S., M. A. Zumberge, and M. J. Cook (2018), Laboratory Simulation and Measurement of Instrument Drift in Quartz-Resonant Pressure Gauges, *IEEE Access*, 6, 57334-57340, https://doi.org/10.1109/ACCESS.2018.2873479.

Sasagawa, G., M. J. Cook, and M. A. Zumberge (2016), Drift-corrected seafloor pressure observations of vertical deformation at Axial Seamount 2013–2014, *Earth and Space Science*, 3(9), 381-385, https://doi.org/10.1002/2016EA000190.

ABSTRACT OF THE DISSERTATION

Calibrated Ocean Bottom Pressure Measurements for Marine Geodesy

by

Matthew James Cook

Doctor of Philosophy in Earth Sciences

University of California San Diego, 2019

Mark A. Zumberge, Chair

The methods and tools available to make geodetic measurements offshore are still limited but increasingly important for studies of underwater subduction zones, volcanoes, and more. One method is to use ocean bottom pressure sensors, which can be used to measure vertical seafloor motion. While most pressure sensors inherently drift at rates that can exceed tectonic signals, some drift correction methods have been developed.

Self-calibrating pressure recorders (SCPR) correct sensor drift using a piston-gauge calibrator (PGC) that produces a reference pressure whose value can be determined with a high level of accuracy. Changes in the reference pressure observed by the pressure sensors are attributed to sensor drift and are removed from the seafloor pressure. The resulting drift-free pressure record can be used to infer seafloor height. We successfully demonstrated an SCPR at Axial Seamount between 2013 and 2015, and later connected it to real-time cabled infrastructure in 2018.

We also used an SCPR in campaign-style surveys to make absolute pressure measurements on seafloor benchmarks. In this absolute SCPR (ASCPR) we make accurate determinations of the parameters that affect the reference pressure to determine its absolute value. We use the true, absolute reference pressure and the difference between the observed reference and seafloor pressures to determine the absolute seafloor pressure. The measurements provide instrument-independent, fiducial values for calibrating nearby sensors or as individual points in long-term time series. We developed the campaign calibrated pressure measurements and conducted four surveys between 2014 and 2017 in the Cascadia subduction zone to measure the vertical deformation occurring offshore. The results serve as initial reference values that will be useful far into the future for marine geodesy and future surveys could be used to estimate the secular vertical deformation rate.

I investigated additional methods, models, and avenues related to seafloor pressure measurements and marine geodesy. I computed elastic half-space boundary element models for scenarios we may expect to see in Cascadia, which highlight the need for geodetic measurements offshore. I also conducted tests of structure-from-motion photogrammetry as a cost- and time-effective method to monitor small changes within geodetically instrumented seafloor sites. Finally, I explored ocean models and satellite data as potential solutions to the oceanographic noise problem present in many marine geophysical measurements.

Chapter 1

Introduction

Geodesy is the study of the shape, structure, and gravitational field of Earth. Through the advancement of geodesy, we have learned a great deal about a number of broad geophysical phenomena, such as the formation and evolution of tectonic plates, earthquake and volcanic cycles, hydrology, and more. Most of our knowledge of these processes comes from terrestrial geodetic studies, despite the fact that 70% of Earth's surface and many geophysical phenomena are covered by water. The world's oceans and other bodies of water act as an expansive, obscuring medium that is largely inaccessible to most land-based methods. As a result, a considerable gap in our knowledge exists. To fully characterize and understand the geophysical systems and their associated hazards, there is an increasing need to extend geophysical, namely geodetic, measurements into the offshore environment.

1.1 Motivation

The list of geophysical hazards and resources covered by water includes subduction zones, which generate large, damaging earthquakes and tsunamis, volcanoes located along mid-ocean ridges and near subduction zones, and oil extraction and carbon sequestration reservoirs. Although land-based measurements and terrestrial analogues can provide insights and answers to aspects of these systems, they are not enough to fully understand the geophysical processes occurring and characterize the hazards.

Subduction zones have produced a number of considerable, devastating earthquakes and tsunamis in the last decade, such as the 2010 and 2015 Chile, 2011 Japan, 2016 New Zealand, and

2018 Indonesia events. Even those that have not generated large earthquakes in the recent past, such as the Cascadia subduction zone in the United States Pacific Northwest, pose significant hazard to coastal communities around the world.

Subduction zones occur where tectonic plates meet and one subducts, or sinks, beneath the other. Trenches are seafloor features typically deeper than the surrounding region and indicate the point of plate convergence. The interface between the two plates can be locked together, or coupled, due to friction and accumulate strain as the two plates continue to collide. When the locked zone reaches critical failure, the strain releases and the plates slip along the fault as an earthquake. A greater area can rupture in brittle failure at subduction zones due to the shallow dip, or angle of the plate interface, compared to strike-slip faults.

To assess the potential hazard attributed to subduction zone earthquakes, we need to be able to determine the amount and the distribution of plate locking. The total area of the locked zone influences the magnitude of the earthquake. The portion of the locked zone that lies farther up the plate interface, closer to the trench, is considered the up-dip extent and generally plays a greater role in large tsunami generation. The area that lies farther down the interface is the down-dip part. Land-based measurements can provide some constraints on the down-dip extent but are inadequate for constraining up-dip areas of the locked zone. The up-dip part of the locked zone typically extends farther offshore and thus requires an offshore or amphibious approach. Increased marine geodetic measurements will continue to improve our knowledge of subduction zone structure and dynamics.

Volcanoes are another target area for geodetic studies. Many volcanoes around the world – on land and in the ocean – are monitored for activity and potential threat to nearby populations and infrastructure. As the chamber fills with magma, the crust above it swells or inflates. As the volcano erupts and the magma leaves the chamber, the ground subsides or deflates. The eruption can displace material or induce landslides and slope failure, which generate tsunamis, like the 2018 Anak Krakatau event. Although the US Geological Survey (USGS) and other international institutions monitor many volcanoes across the globe and the greatest hazards are generally attributed to terrestrial volcanoes, many more lie underwater and remain poorly monitored or not at all. One exception is Axial Volcano, or Axial Seamount, located along the Juan de Fuca Ridge in the Eastern Pacific. It has been extensively studied over the last few decades and presently is monitored in real-time by permanent, offshore, cabled infrastructure. While some similarities can be drawn between subaerial and submarine volcanoes, improved marine geodetic methods will substantially improve monitoring efforts and help address driving science questions regarding magma chamber dynamics and eruptive cycles, particularly in areas of thinner crust.

Another notable target area includes resource reservoirs for either extracting gas and oil or sequestering carbon dioxide. Often these reservoirs and fields are located beneath the seafloor, such as the Gulf of Mexico and the North Sea and are therefore a prime candidate for marine geodesy (Stenvold et al., 2006). The extraction or injection of fluids is often expensive and difficult, so the ability to monitor changes in the saturation, compaction, and subsidence of these reservoirs can provide useful considerations for project and risk (e.g. a CO_2 leak) management.

1.2 Geodetic Methods

Over the last several decades, we have developed and refined the tools and methods available for conducting geodesy. Measurements of the motion, deformation, and structure of the crust and subsurface variations are routinely achieved with mm- and cm-level resolution and accuracy. Much of geodesy is conducted on or over land, where techniques can leverage the unperturbed transmission of electromagnetic (EM) radiation and are not necessarily subject to considerably harsh operating conditions. Geodetic measurements in marine environments face a greater number of challenges, in part owing to the crust being submerged under and obscured by up to thousands of meters of water. Water strongly attenuates EM radiation, imparts great pressures at depth, and is corrosive to many metals typically used in instrument construction. As a result, some of the commonly-used terrestrial methods cannot be leveraged, and alternative methods are necessary to collect marine geodetic measurements. In recent decades, marine methods capable of achieving cm-level resolutions and accuracies comparable to terrestrial methods have been developed.

Terrestrial geodetic methods typically include the use of strainmeters, tiltmeters, gravimeters, interferometric synthetic aperture radar (InSAR), and Global Positioning System (GPS) or Global Navigation Satellite System (GNSS), although a number of other methods exist. Strainmeters can measure sub-μm deformations over baselines of tens of meters or more. Tiltmeters are capable of measuring changes in the surface inclination on the order of 10^{-9} radians. Gravimeters can determine variations in local gravity on the order of 10^{-9} g and therefore local vertical deformation or subsurface density changes. Once a GPS station or monument is setup, measurements with mm-level resolution can be made continuously or during intermittent surveys. InSAR produces interferograms from multiple SAR images to detect and measure surface changes with mm- to cm-scale resolution.

Many of the techniques used on land are inaccessible in marine settings due to the aforementioned limitations of EM radiation in water and the high pressure and corrosive conditions. Despite this, a number of methods tailored for use in water have been developed, notably acoustic ranging, multibeam bathymetry, sidescan sonar, the marine analogues to terrestrial strainmeters, tiltmeters, and gravimeters, and pressure sensors (Burgmann and Chadwell, 2014). Many of these methods are capable of achieving resolutions similar to land-based methods.

Although water is very limiting for methods that rely on EM radiation, it is conducive to methods that use acoustic waves, which can travel significantly farther than light in water. Acoustic methods are resolution-limited by imperfect determinations of the sound speed (only known to 1 part per 10,000 typically) and lateral variations throughout ocean. Acoustic ranging between one or several precision transponders is now routinely used to measure cm-level distances over several km. Tying acoustic ranging measurements from the seafloor to a ship or other surface vehicle, by ranging between transponders and a kinematic GPS-enabled ship, can be used to make globally referenced measurements with cm-level precision over a period of days. Other ship-based methods including multibeam bathymetry and sidescan sonar have footprints of tens of meters and are useful for surveying large areas with high spatial coverage. These methods have low resolution and are limited to m-scale offsets and deformation between surveys. Recent developments have seen the incorporation of multibeam and sidescan systems to autonomous underwater vehicles (AUVs) or remotely operated vehicles (ROVs) that can navigate tens of meters off of the seafloor and therefore achieve better resolution on the order of 10 to 20 cm.

A number of instruments commonly used on land, such as strainmeters, tiltmeters, and gravimeters, have been modified and demonstrated in the water. Seafloor fiber optic strainmeters have been used to make measurements of tens of nanostrain, which is comparable to their terrestrial counterparts (Blum et al., 2008; Zumberge et al., 2018). Marine tiltmeters can achieve 10^{-8} radian resolution but are limited by intrinsic drift and typically poorer coupling compared to those on land. Gravimeters have also been adapted for use in the ocean and are also capable of detecting μGal-level changes in subsurface mass distributions (Zumberge et al., 2008).

Pressure sensors are another established marine geodetic technique. Since water is nearly a thousand times denser than air, changes in the water column height produce readily measurable pressure changes. Pressure changes are commonly measured in kPa, and 0.1 kPa is equivalent to a 1 cm height change to within 2%. We can accordingly infer the vertical motion or deformation of the seabed. Pressure sensors are inherently limited by long-term drift that can be up to several kPa/year, or tens of cm/year, which can contaminate, if not completely overwhelm, expected vertical tectonic signals.

1.3 Outline of the Dissertation

This dissertation discusses my work on seafloor pressure instrumentation, measurements and data, results, and implications for marine geodesy.

Chapter 2 discusses the state of pressure instrumentation and provides background for the instruments used in the scope of this dissertation – notably, the self-calibrating pressure recorder (SCPR) and absolute self-calibrating pressure recorder (ASCPR).

Chapter 3 describes in-depth the metrology, accuracy, and uncertainty of the SCPR and ASCPR instruments as are relevant and necessary for geodetic measurements. Some of this work was published in *IEEE Access* in October 2018.

Chapter 4 discusses continuous SCPRs in the context of Axial Seamount, including (1) an autonomous deployment from 2013 – 2015 and (2) a long-term installation on the Ocean Observatories Initiative (OOI) Cabled Array in 2018 that is expected to continue to run until 2020 or longer. The first part of this chapter was published in *Earth and Space Science* in September 2016. The second part is being prepared for journal submission.

Chapter 5 describes the use of the ASCPR in campaign-style surveys to measure secular vertical deformation in the Cascadia subduction zone between 2014 and 2017. This chapter is being prepared for journal submission.

Chapter 6 summarizes additional considerations, methods, and their implications for geodetic seafloor pressure measurements and marine geodesy. A portion of this work is in revision for publication in *Earth and Space Science*.

Chapter 7 provides concluding remarks and future work for pressure sensors and marine geodesy.

Chapter 2

Pressure Sensors

Water pressure is a useful proxy for measuring vertical crustal motion since small height changes in the water column or seabed produce easily measurable pressure changes. In this dissertation, I present pressure in kPa and seafloor height in cm, where 0.1 kPa is approximately equivalent to 1 cm. Although pressure sensors are sensitive to changes of 0.01 kPa over short periods of time, they are unreliable for long-term measurements spanning weeks or more due to inherent drift. The root cause of sensor drift is not well-known, but a number of hypotheses suggest it may be attributed to any number and combination of mechanical creep, quartz crystal aging, outgassing, or pressure loading and unloading (Paros and Kobayashi, 2015b). Drift rates can be several kPa/year (tens of cm/year equivalent), which exceed expected vertical deformation rates in many locations. Rates vary in magnitude and direction (positive, negative) and depend on individual sensors, deployment depth, temperature, and other conditions. Thus, calibrations prior to or after deployments cannot reliably capture the drift signal. Long-term drift rates are generally considered to be linear, though suggested models include exponential-linear, power-law, logarithmic, or combined power-logarithmic functions (Polster et al., 2009; Watts and Kontoyiannis, 1990; Paros and Kobayashi, 2015a). While the most accessible and commonly used pressure sensors experience drift, a number of methods to characterize and correct sensor drift have been developed and demonstrated.

Most pressure sensors for deep oceanographic research use either a bellows or Bourdon tube construction to measure pressure. Early sensors commonly used bellows, which sense pressure changes based on an internal volume, but high uncertainties and drift rates led to the decline of bellows-based sensors. Bourdon tubes are roughly J-shaped tubes that deform as pressure is applied to the end pressure port or inlet, such that the curved portion will begin to straighten out. Many mechanical pressure gauges actuate an indicator needle attached to the moving end of the bourdon tube. In the Paroscientific DigiQuartz pressure sensors, which are some of the most widely used and most precise for oceanographic studies, a quartz crystal oscillator bridges the gap between the moving end of the Bourdon tube and the rigid base. The precise relationship between the quartz crystal oscillator frequency and applied pressure can be determined with parts per billion precision based on a well-defined equation. These types of sensors also exhibit drift, though less than their bellows-based counterparts. Presently, these are the most commonly used sensor types.

Paroscientific, Inc. pressure sensors are used in the sensors discussed in this dissertation. Different models including 2200A, 3000-, and 4000-series were used depending on cost, availability, and needs of the projects. In one experiment, Anderaa pressure sensors were also used for comparison purposes (Sasagawa et al., 2018). The sensors ranged in rated pressure from 50 kPa to 69,000 kPa.

2.1 Bottom Pressure Recorder (BPR)

Bottom pressure recorders (BPRs), also referred to as absolute pressure gauges (APGs), use Bourdon tubes and quartz crystal strain gauges. Sensors are typically deployed for months to years at a time and usually record data continuously at rates between 100 Hz (100 samples per second) and 0.0003 Hz (1 sample per hour). In some instances, BPRs are installed on permanent cabled infrastructure to provide real-time, continuous data and eliminate the challenge of battery storage. They can be purchased, configured, or built to suit the specific needs of projects. The largest limitations are sensor drift, sensitivity to dynamic and static temperature effects, and limited deployment durations.

Notable examples in the context of this dissertation include tide gauges built by the Gravity Lab at the Scripps Institution of Oceanography (SIO), BPRs built by the Applied Physics Laboratory (APL) at the University of Washington (UW), and those installed on cabled infrastructure, such as the United States' OOI Cabled Array or Japan's Dense Oceanfloor Network System for Earthquakes and Tsunamis (DONET).

2.2 Mobile Pressure Recorder (MPR)

The mobile pressure recorder (MPR) addresses the issue of sensor drift by performing circuitous, closed-loop surveys using a remotely operated vehicle (ROV) over a period of several hours to days within an array of seafloor benchmarks that includes a remote station located outside the region of expected deformation. The pressure at each station is measured relative to the remote station, whose value is considered stable over time. Any changes in the measured pressure at the reference station are attributed to sensor drift, which is then calculated and removed from the rest of the pressure measurements. Repeat surveys between years are used as single points in time series to estimate deformation or as constraints to characterize drift in co-located BPRs.

The MPR at the SIO consists of a pair of Paroscientific pressure sensors, a tilt sensor, and ancillary electronics. Redundant pressure sensors allow us to compare sensor behavior and average the measurements to reduce measurement error. The pressure sensors are sensitive to orientation and the tilt sensor allows us to calculate and correct the pressure changes caused by the orientation or rotation of the MPR. Pressure, temperature, and tilt data are recorded in real-time through the ROV to a computer. The ROV carries the MPR and places it on the benchmark, where pressure data are collected for 10 to 20 minutes at a time, and then moves to the next station. Once the data span two measurements at the reference station, a short-term drift rate can be estimated and removed from the other pressure measurements.

Some of the challenges encountered when using the MPR method include the fact that measurements are relative, require a stable, unperturbed seafloor benchmark, and similar to BPRs, can be highly sensitive to both static and dynamic temperature changes. Measurements are made relative to the remote station, which is assumed to have zero deformation. If that station is not in fact stable during the duration of a survey or between surveys, then results may be biased. Problems can arise from the use of seafloor benchmarks as well. If a benchmark is disturbed from its original position, then past and future measurements may be difficult to tie together, and the time series could be compromised.

This method has been successfully demonstrated in the North Sea and at Axial Seamount. In the North Sea, simultaneous gravity and pressure measurements were made starting in 1998 to monitor the gas reservoir compaction and subsidence (Stenvold et al., 2006; Zumberge et al., 2008). Since 2000, MPR measurements at Axial Seamount have been used to monitor the volcanic inflation and eruption cycle (Chadwick et al., 2006; Nooner and Chadwick, 2009; Chadwick et al., 2012; Nooner and Chadwick, 2016). These types of surveys can also be done on much smaller scales over a few hours to infer height differences between adjacent benchmarks, monuments, or platforms.

2.3 Self-Calibrating Pressure Recorder (SCPR)

The self-calibrating pressure recorder (SCPR) addresses the problem of sensor drift by intermittently performing in situ calibrations using a piston-gauge calibrator (PGC), otherwise known as a deadweight tester (DWT), whose pressure is proportional to a mass force divided by piston cross-sectional area (Sasagawa and Zumberge, 2013). A pair of pressure sensors normally observe seawater pressure and at a regular interval, a three-way valve switches the pressure source from seawater to the PGC for a short period of time. The pressure produced by the PGC is known with high precision and is considered to be stable over time. Therefore, any changes in the reference, or calibration, pressure observed by a quartz gauge are attributed to drift and sensor effects from which a drift rate can be calculated. Since drift is a common mode signal to observations of both seawater and calibration pressures, the calculated drift rate is removed from the seawater pressure record to produce a drift-free pressure record.

The schematic drawing in Figure 2.1 shows the key components of the SCPR. Two Paroscientific pressure sensors, which are included for redundancy and comparisons, are connected to a three-way selector valve (SV), which hydraulically connects the sensors to either the ambient seawater or the PGC. A two-way valve, the charge valve (CV), is connected only to the PGC can be controlled to allow the seawater pressure to pressurize and lift the piston-cylinder assembly off the bottom stop. A specific mass is custom-made so that the reference pressure produced is slightly less than the ambient seawater pressure for each deployment. By choosing a reference pressure close to seawater pressure, we believe we reduce any ambiguities that may be caused by different drift rates occurring at different operating pressures or larger magnitude and longer duration effects caused by hysteresis. The reference pressure to first order is proportional to the mass force over the piston area. However, it requires higher order corrections, so internal barometer, tilt, and piston-cylinder temperature, height, and rotation rate sensors are installed, which are detailed in Chapter 3. The SCPR also includes mechanisms to lock the mass in place, spin the mass, level the gimbals, and actuate valves, and electronic controllers to initiate calibrations and record data.

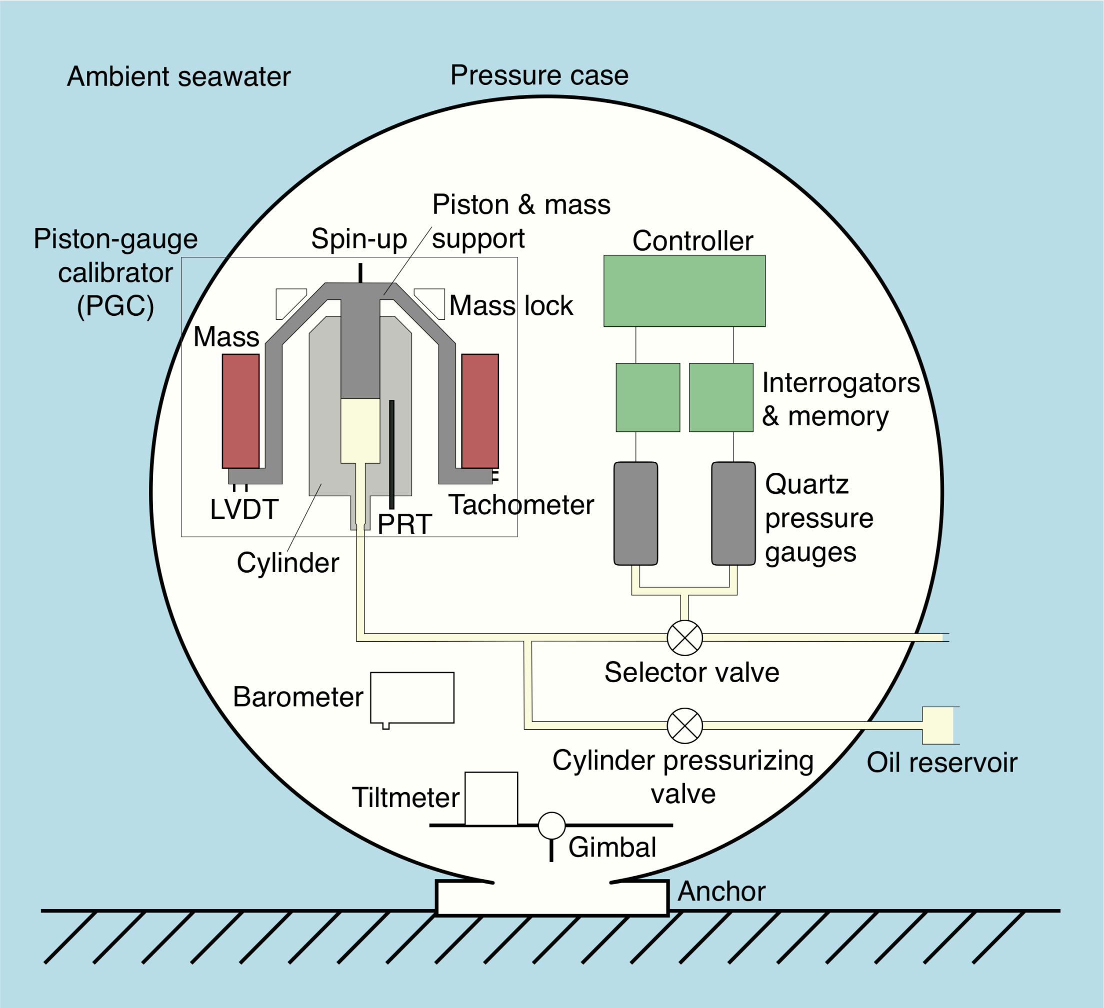

Figure 2.1 A schematic drawing of the SCPR and ASCPR highlighting key components.

Normally the pressure sensors observe the seawater pressure. At a regular, user-defined interval (e.g., 20 days), a calibration is initiated. The user-defined calibration period is typically about 20 minutes. Following deployment to the seafloor and unlocking the mass, the calibration sequence follows:

(1) The tiltmeters check the orientation and the gimbals level the instrument as needed.

(2) The CV is opened, which allows the seawater pressure to pressurize and raise the piston-cylinder off the bottom. It closes when a preset height is reached.

(3) The spin mechanism engages to spin the piston and mass around the vertical axis and disengages once fully spun up.

(4) The SV changes position so that the pressure sensors measure the reference pressure produced by the PGC.

(5) The reference pressure and the ancillary data required for corrections are recorded for the calibration period.

(6) If the mass rotation rate drops below a certain threshold, then the spin mechanism will briefly re-engage to spin up the piston and mass again.

(7) If the piston-cylinder height drops below a certain threshold, then the CV will briefly re-open to lift up the piston and mass again.

(8) Once the calibration period has been concluded, the SV changes position so that the pressure sensors resume measuring ambient seawater pressure. The piston drops to the bottom stop.

The pressure sensors continue to observe seawater pressure until the following calibration. Depending on the configuration of an autonomous or cabled SCPR, the calibrations can be done automatically through the controller, initiated acoustically, or manually controlled remotely. Likewise, data can be recovered acoustically, collected from the memory card when the instrument is recovered to the surface, or recorded in near real-time to a server.

In order to model the drift rate, we rely on the stability of the PGC reference value over time. The details of the reference pressure, higher order terms, and uncertainty analysis are discussed in Chapter 3. The total stability of the reference pressure value is approximately 10 ppm per calibration point, equivalent to 1 cm error at a deployment depth of 1 km. The calibration pressures are considered stable, so long-term observed changes in the calibration pressure are caused by drift in the observing pressure sensors. A combined exponential-linear function can be fit to the corrected calibration data to determine the drift rate. If insufficient calibrations exist, then a linear fit would capture the dominant long-term linear drift rate. The drift rate between observations of both pressure sources is the same since the reference pressure is chosen such that it is close to the ambient seawater pressure. This makes effects due to different drifts at different pressures negligible. By removing the drift rate from the seawater pressure, we produce a drift-corrected record of seafloor pressure that can be used to infer vertical seafloor height changes.

2.4 Absolute Self-Calibrating Pressure Recorder (ASCPR)

The absolute self-calibrating pressure recorder (ASCPR) uses the same PGC calibration method as the standard SCPR, but in campaign-style surveys instead of continuous deployments. Instead of addressing only the stability of the PGC reference pressure, its true value can be determined with an absolute accuracy of ~15 ppm, equivalent to a couple cm per 1 km depth. The difference between the true and observed reference pressures is used to determine the true, absolute seafloor pressure from the observed seafloor pressure. Absolute seafloor pressures provide important instrument-independent, fiducial values that provide value as single points in time series spanning decades or longer, or as calibration values for nearby continuous instrumentation.

Since the ASCPR performs calibrations using a PGC, its internal components are configured the same as the standard SCPR, notably the pressure sensors, PGC, three-way selector valve, two-way charging valve, and ancillary sensors. The schematic diagram is shown in Figure 2.1 and a photograph of the internal components is shown in Figure 2.2. However, the ASCPR is designed for campaign-style surveys, so a few notable differences were made to accommodate ROVs. The primary mechanical differences include a different frame with a smaller, triangular footprint and larger, more robust cage to support ROV handling and placement. Batteries, floats, and anchors are not included, since the instrument is tethered to the ROV. The ASCPR includes newer revisions of various controllers and electronics and an electrical penetrator through the pressure case to provide power and two-way serial communications with the ROV.

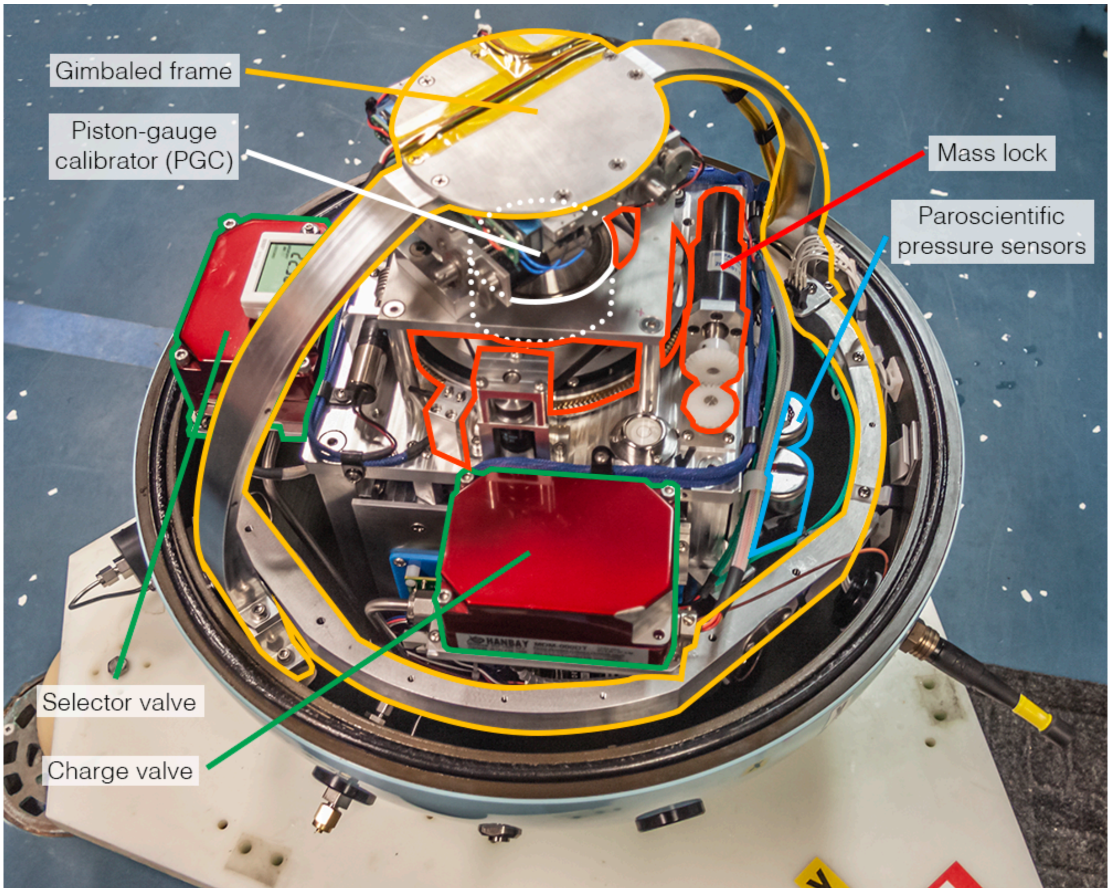

Figure 2.2 A photograph of the components inside the ASCPR with key components identified and labeled. The PGC is not visible from this view but is outlined with a dotted line.

The ASCPR is operated in the same way as the SCPR but requires manual oversight. The ROV carries the ASCPR to a benchmark installed on the seafloor and places the instrument on it. Alternating 10- to 20-minute-long seawater and calibration observations are made for 2 to 3 hours. The calibration sequence remains the same:

(1) The mass is unlocked, and the instrument is leveled.
(2) The CV is opened to lift the piston-cylinder off the bottom and closed when the piston-cylinder reaches a preset height.
(3) The piston and mass are spun up.
(4) The SV alternates the pressure sensors between ambient seawater pressure and the PGC reference pressure.
(5) The reference pressure, seawater pressure, and ancillary data are recorded for the duration of the benchmark occupation.
(6) The mass rotation rate and piston-cylinder height are monitored and adjusted as needed.
(7) At the end of the calibration period, the SV switches the pressure sensors back to ambient seawater pressure, the mass is locked, and the ASCPR is recovered back to the ROV.

Absolute pressure measurements require high-accuracy determinations of the factors that affect the reference pressure and do not rely on the stability of the values over time alone. The full reference pressure equation and uncertainties are addressed in Chapter 3. The total accuracy of the ASCPR system is approximately 15 ppm, or about 1.5 cm error at depths of 1 km and is traceable to NIST (National Institute of Standards and Technology) standards. The calibration pressures for a single survey are corrected first for higher order terms and then for sensor drift and thermal transients by fitting combined exponential-linear curves over each survey interval. The known, calculated reference pressure is differenced with the corrected, observed reference pressure. The offset between the reference pressures is also valid over the seafloor observations and is added to the observed seafloor pressure to determine the true, absolute seafloor pressure.

Measurements can be completed in a few hours so multiple benchmarks can be surveyed over a few days. Therefore, a single ASCPR surveying multiple benchmarks in a profile or array provides a greater spatial coverage of calibrated pressure measurements than a single continuous instrument would. The absolute measurements are instrument-independent and drift-free and can be used as individual points in long-term time series. Alternatively, continuous BPRs can be deployed or installed nearby or co-located with benchmarks to provide high-rate information spanning multiple surveys and mitigate aliasing tides and oceanographic effects.

2.5 Ambient-Zero-Ambient (A0A)

The ambient-zero-ambient (A0A or AZA) method was initially proposed during the development of the SCPR but has only recently been implemented in practice. These sensors use a three-way valve to control the pressure source observed by one or more pressure sensors similar to the SCPRs; however, the reference pressure is the “zero” internal air pressure of the housing, not the pressure produced by a mechanical PGC. The air pressure inside the pressure housing is measured by a barometer, which has a lower full-scale range and considerably less drift (mm/year or less). Regular, intermittent reference pressure observations punctuate an otherwise continuous record of seafloor pressure. The barometric pressure observations as measured by the pressure sensors are compared to the measurements from the barometer. Any deviations are attributed to long-term drift.

There is still debate whether or not switching the pressure sensors from full-scale pressure (thousands of m equivalent) to zero pressure (tens of m equivalent) affects the sensor behavior. Hysteresis has been observed before and could contaminate drift corrections. Similarly, this method assumes and relies on the fact that the sensor drift is the same at low and high pressures. In an initial 12-month laboratory test at pressures and temperatures closely simulating seafloor conditions, we found that the A0A calibration method was capable of correcting drift with mm/year precision (Sasagawa et al., 2018). Other laboratory and in situ tests suggest that this method may not actually be consistent and is highly sensitive to the valve switching mechanism and timing (Nishmagi et al., 2018; Wilcock et al., 2018). Finally, switching from high pressure to low pressure results in the fluid (oil) loss from the hydraulic line open to the inside of the pressure housing. Although losses are small and a large reservoir or compensator can be incorporated, this aspect imposes a limit on the deployment duration.

The A0A method is a promising solution to the drift problem that is smaller, cheaper, and more easily implemented than the SCPRs. Continued laboratory tests and some of the first in situ deployments offshore California, Oregon, Alaska, and New Zealand will produce data to assess the uncertainties and viability of A0A in practice.

Chapter 3

Instrument Metrology and Pressure Measurement Accuracy

3.1 Background

Pressure sensors are often calibrated using a PGC in laboratory settings with high levels of accuracy on the order of parts per million (ppm). The reference pressure can be accurately calculated if the mass, piston area, local gravitational acceleration, and other terms are accurately known. A standard PGC consists of a mounting post in which the piston-cylinder assembly is installed. A bell to support the mass rests on the top of the piston-cylinder assembly. The piston and mass are typically rotated, so the piston and cylinder are in a state of dynamic friction, which has a lower coefficient and is more stable than static friction conditions. Additional terms in the reference pressure become important at the ppm level but can be measured and corrected.

The reference pressure corrections and uncertainties can be classified into two types: relative and absolute. In the laboratory, many of the PGC parameters such as temperature, tilt, and barometric pressure, are accurately measured and controlled. However, a modified PGC in an enclosed pressure housing that is deployed to the bottom of the ocean inherently produces greater uncertainties than are encountered in the laboratory. The SCPR relies on the relative uncertainty, or stability, of the reference pressure over time to determine the drift of the pressure sensors. Alternatively, the ASCPR requires absolute determinations of the reference pressure parameters to produce instrument-independent absolute seafloor pressures.

In addition to the reference pressure produced by the PGC, other instrumental considerations are necessary for absolute measurements, though they are not as important for relative measurements (i.e., the SCPR). These includes factors such as the positioning and orientation of the pressure sensors relative to the PGC and seawater port, which introduce hydraulic head differences. The tilt and orientation of the sensor and seafloor benchmark can also introduce pressure changes due to height differences.

The following chapter documents the work done to perform both relative (i.e., stability) and absolute calibrations of the reference pressure parameters, ancillary sensors, and instrument design and operation. I describe absolute uncertainties using the notation δ, and relative uncertainties, or stabilities, using the notation $\Delta(t)$. All of the uncertainties listed represent 95% confidence intervals (CI) unless otherwise noted.

The PGCs we used in the laboratory, SCPR, and ASCPR are DH Instruments models PC-7300-2 (nominally 2,000 kPa/kg or 2 MPa/kg) and PC-7300-200 (nominally 200 kPa/kg), both of which use oil as the pressure medium.

3.2 Reference Pressure

The pressure, $P_{\text{reference}}$, produced by a PGC depends on a precision mass, M, the local gravitational acceleration, g, and the cross-sectional area of a piston assembly, A, and to first order and can be written:

$$P_{\text{reference}} = \frac{Mg}{A} \tag{3.1}$$

However, determining the true PGC pressure requires higher order corrections including internal air pressure, buoyancy of the mass, tilt, thermal expansion and elastic deformation of the piston assembly, and surface tension. The full reference pressure described in Bean (1994) is expressed:

$$P_{\text{reference}} = \frac{M\left(1 - \frac{\rho_{\text{air}}}{\rho_{\text{mass}}}\right) g \left(1 - \frac{\theta^2}{2}\right) + \gamma C}{A_0[1 + 2\alpha(T - T_0)](1 + bP_{\text{fluid}})} + P_{\text{baro}} \tag{3.2}$$

Each of these correction terms needs to be accounted for either relatively or absolutely. Many of the parameters can be measured directly, though some require indirect measurements or calculations. All of the terms are discussed in the following sections. They are described in Table 3.1.

Table 3.1 Variables used in the reference pressure equation.

Term	**Variable**
Pressure, total	P
Mass	M
Gravitational acceleration	g
Piston area	A_0
Density, internal air	ρ_{air}
Density, mass	ρ_{mass}
Angle with respect to vertical	θ
Surface tension	γ
Piston circumference	C
Linear coefficient of thermal expansion	α
Piston-cylinder temperature	T
Reference temperature	T_0
Coefficient of elastic deformation	b
Pressure, fluid	P_{fluid}
Pressure, internal air pressure	P_{baro}

3.3 Instrumental Considerations

3.3.1 Mass

The pressure produced by the PGC is largely determined by the selected mass. The total mass is the combination of the PGC components – the piston and the mass-carrying bell – and the selected mass. The total mass times the gravitational acceleration equals the mass force, which acts on the piston cross-sectional area to produce the reference pressure. Since a mass is specifically chosen to produce a reference pressure that closely matches the ambient seawater pressure, we required different masses for different deployment depths. Several masses were custom made out of stainless steel, aluminum, or a combination of the two, to conform to the instrument form factor and produce the desired values. The masses are identified by the name of station or deployment location. Masses O2, O3, O4, and O5/O6 were made for the stations described in Chapter 5, and the Axial mass was made for the SCPR deployed at Axial Seamount described in Chapter 4.

All of the custom masses were weighed against several standard masses and corrected for linear scale deviations and buoyancy to determine an accurate value. The masses were weighed using a Mettler Toledo model XP10002S scale (SN1130021829) against a number of calibration masses. The Mettler-Toledo scale was calibrated using known calibration masses. A linear regression was used to correct the measured values to the known mass values. Once the scale correction was applied, a buoyancy correction was needed to determine the absolute mass values of the aluminum masses since the scale was calibrated using stainless steel masses.

The Axial mass was calibrated in July 2013 against two McMaster Carr standard masses: (1) 1,000.12 ± 0.1 g (SN 1826) and (2) 2,996.47 ± 0.3 g (SN 1302). The other O2, O3, O4, and O5/O6 masses were calibrated in May 2016 against two class 1 calibration masses, which have a 0.010 g tolerance, and two McMaster Carr standard masses: (1) Mettler 2,000.00 ± 0.01 g (SN 2440), (2) Troemner 5,000.00 ± 0.01 g (SN 48482), (3) McMaster Carr 1,000.12 ± 0.1 g (SN 1826), and (4) McMaster Carr 3,000.07 ± 0.3 g (SN 8135).

The O1 mass was sent to Troemner in December 2014 where it was calibrated against NIST standards. The PGC component masses were measured by Fluke and with NIST-traceable standards. We used the values and uncertainties provided by Troemner and Fluke for these components, since they are better equipped to make measurements with greater accuracy. Table 3.1 lists the masses of the PGC components; Table 3.2 lists the values of the deployment masses; and Table 3.3 lists the total masses of the configured PGC, mass bell, and deployment mass.

Table 3.2 Mass values of the PGC components including the piston-cylinder assembly and the mass bell.

Name	**Variable**	**Mass Bell SN 904**	**Mass Bell SN 1086**	**PC-7300-200 SN 1791**	**PC-7300-2 SN 1963**	**PC-7300-2 SN1466**
Mass (g)	M	800.0119	800.0054	200.0014	200.0012	200.0009
	δM	0.008	0.008	0.003	0.003	0.003
Pressure (ppm)	δP	10	10	15	15	15

Table 3.3 Mass values of the deployment masses.

Name	**Variable**	**O1**	**O2**	**O3**	**O4**	**O5 & O6**	**Axial**
Mass (g)	M	13,648.20	8,539.05	5,544.40	2,029.42	2,509.20	6,634.35
	δM	0.01	0.04	0.01	0.01	0.01	0.02
Pressure (ppm)	δP	0.7	4.7	1.8	4.9	4.0	3.0

Table 3.4 Total mass values of the piston-cylinder assembly and deployment mass, and their effect on reference pressure.

Name	**Variable**	**O1**	**O2**	**O3**	**O4**	**O5 & O6**	**Axial**
Mass (g)	M	14,648.207	9,539.057	6544.407	3,029.427	3,509.207	7,634.363
	δM	0.013	0.041	0.013	0.013	0.013	0.022
Pressure (ppm)	δP	0.9	4.3	2.0	4.3	3.7	2.9

3.3.2 Local Gravitational Acceleration

Calculation of the mass force on the PGC requires knowledge of the local acceleration due to gravity, g. While absolute gravity has been measured on land for decades and is accurate on the order of 10^{-8} m/s^2, absolute gravity measurements on the seafloor are intrinsically more challenging. Absolute seafloor gravimeters have been proposed but yet to be reasonably and reliably demonstrated (Zumberge and Canuteson, 1995). Since absolute gravity measurements are not presently available, I calculated a gravitational acceleration using the international gravity formula, a global gravity anomaly model, and the seawater gradient with seafloor depth.

I used the international gravity formula described in Götze (2014), which gives a gravitational acceleration, g_ϕ, on the reference ellipsoid based on the latitude, ϕ. For each location discussed in this dissertation, I used the gravity anomaly, Δg, determined from the EGM2008 model (Pavlis et al., 2012) added to the international gravity value at a specified latitude, and then translated it to the seafloor using the known depth, z (in meters), and the average seawater gravity gradient (1/s^2):

$$g_\phi = 9.780327\left[1 + (0.0053024)\sin^2(\phi) - (0.0000058)\sin^2(2\phi)\right] \ m/s^2 \tag{3.3}$$

$$g = g_\phi + \Delta g + \left(2.22\times10^{-6}\right)z \ m/s^2 \tag{3.4}$$

I assumed the seafloor depth was accurate to ±5 m, which corresponds to 1.1 mGal, or 1.1×10^{-5} m/s^2. The EGM2008 gravity anomaly model has a nominal uncertainty of 2 mGal, or 2.0×10^{-5} m/s^2, over the oceans (Pavlis et al., 2012). A total uncertainty in the gravitational acceleration of 2.3×10^{-5} m/s^2 was used.

Absolute seafloor pressure measurements are not based on direct measurements of the absolute gravitational acceleration, but rather a model of gravity and some assumptions. However, the value of g used is documented and can be retroactively adjusted should absolute seafloor gravity measurements become available.

Table 3.5 An example value of the gravitational acceleration and its effect on reference pressure.

Name	**Variable**	**Effect**
Gravity (m/s^2)	g	9.81055
	δg	2.3×10^{-5}
Pressure (ppm)	δP	2.3

3.3.3 Piston-Gauge Calibrator Cross-Sectional Area

The PGC cross-sectional area determines the pressure that the mass force produces. Two sizes of PGCs were used depending on the target deployment depth and calibration pressure. The DH Instruments model PC-7300-200 is a larger sized PGC with a nominal area of 50 mm^2 that produces 200 kPa/kg was used in shallow depths of 100 m or less. The DH Instruments model PC-7300-2 is a smaller PGC with a nominal area of 5 mm^2 that produces 2,000 kPa/kg (2 MPa/kg) was used for deployments at depths of several hundred m or more. The cross-sectional areas were measured by Fluke in crossfloat tests with NIST-traceable standards. The values listed here were determined at a standard operating temperature of 20 °C. The effects of thermal expansion and elastic deformation on the area are discussed in Sections 3.3.5 and 3.3.8 respectively.

Table 3.6 The cross-sectional areas of the PGCs and their effect on the reference pressure.

Name	**Variable**	**PC-7300-200** **SN 1791**	**PC-7300-2** **SN 1963**	**PC-7300-2** **SN 1466**
PGC Area (m^2)	A_0	4.90216×10^{-5}	4.901758×10^{-6}	4.9034144×10^{-6}
	δA_0	6.9×10^{-10}	1.2×10^{-10}	1.2×10^{-10}
Pressure (ppm)	δP	14	25	25

3.3.4 Barometric Pressure

Barometric pressure is the largest correction term in the total reference pressure. We refer to the air pressure inside the pressure housing as the barometric pressure since it is measured with a barometer. Throughout this dissertation, I refer to the ambient air pressure inside the housing as barometric pressure. The barometric pressure is independent of the PGC and summed directly with the PGC pressure. Barometers have a lower full-scale range and experience drift several orders of magnitude less than deep water pressure sensors. Therefore, we can make direct barometric pressure measurements with high accuracy and less concern for sensor drift.

The SCPR and ASCPR both use a Vaisala PTB110 barometer. It has an operating range of 50.0 to 110.0 kPa with an accuracy of ±0.02 kPa. The barometer does experience drift at a rate of approximately 0.01 kPa/year. The repeatability or stability of the measurements is stated to be ±0.003 kPa.

The Vaisala PTB110 (SN K2650006) in the ASCPR was calibrated in May 2016 against our higher accuracy Paroscientific model 6016B barometer (SN 71692). Prior to the Vaisala calibration, the 6016B barometer was calibrated against a Paroscientific model 765-16B pressure standard (SN 101778) at the Marine Physical Laboratory. Even earlier, the Paroscientific 765-16B was calibrated by Fluke.

The Paroscientific 765-16B was calibrated across a range of 50.0 to 110.0 kPa and found to be accurate to better than ±0.0004 kPa, which was the same as the original calibration error. Our Paroscientific model 6016B barometer (SN71692) was calibrated against the Paroscientific 765-16B barometer across the range of 60.0 to 110.0 kPa. A linear correction function to our Paroscientific barometer was determined to be:

$$P_{\mathrm{6016B,true}} = \left(P_{\mathrm{6016B,measured}}\right)(0.999995) + 0.013991\ \ kPa \tag{3.5}$$

While the span is different, it corresponds to less than 0.001 kPa across the full range of the barometer. The 0.14 kPa offset was an important consideration for calibrating the Vaisala PTB110 however.

The Vaisala PTB110 was calibrated against the Paroscientific 6016B by connecting the two barometers to the same closed pressure source at room temperature. The air pressure inside the pressure source was controlled from 61 to 103 kPa. Two tests were completed, and the residuals were used to calculate the following linear correction function to the Vaisala barometer:

$$P_{\mathrm{Vaisala,true}} = \left(P_{\mathrm{Vaisala,measured}}\right)(0.997689) + 0.284061\ \ kPa \tag{3.6}$$

The 95% CI of the residuals was ±0.02 kPa. We updated the voltage-to-pressure conversion values and used them consistently for all of our barometric pressure measurements. The barometric pressure uncertainty we determined agrees with the manufacturer specified uncertainty.

3.3.5 Thermal Expansion of the Piston-Cylinder Assembly

The PGCs installed in the SCPR and ASCPR are subject to greater temperature changes than are commonly found in laboratory settings. The thermal expansion (or contraction) of the piston-cylinder assembly affects the cross-sectional area and the produced pressure for a given force. If the temperature increases, then material expands and the area increases, producing a smaller pressure. Similarly, if the temperature decreases, then the material contracts and the area decreases, producing a greater pressure. At common deepwater seafloor temperatures of a few °C, the thermal expansion effect can produce about 150 ppm effect in the total reference pressure, while variability in the effect are typically about 1 ppm.

The expansion or contraction depends on the material properties of the piston and the cylinder and the amount of temperature change relative to a standard operating temperature, T_0. The linear coefficient of thermal expansion, α_{material}, is the relative length change of a material per °C. The amount of thermal expansion of the cross-sectional area of the piston depends on the coefficients of thermal expansion of both the cylinder and piston materials. Since the values of α_{cylinder} and α_{piston} are small and identical (several ppm/°C), the combined areal thermal expansion effect can be approximated by a sum of the linear coefficients. The thermal expansion pressure effect can be expressed:

$$\begin{aligned} P &= \frac{Mg}{A_0[1 + 2\alpha(T - T_0)]} \\ &= P_0 \frac{1}{[1 + 2\alpha(T - T_0)]} \end{aligned} \tag{3.7}$$

We use a value of 20°C for T_0, which is the standard temperature for DHI measurements and the international standard temperature. This effect relies on an accurate value of the coefficient of thermal expansion, α, and measurements of the piston-cylinder temperature, T. The temperature of the PGC is measured with a platinum resistance thermometer (PRT) located inside the mounting post and was calibrated twice. DH Instruments provides a linear coefficient of thermal expansion of 4.5×10^{-6} °C^{-1}; however, other studies (e.g., Okaji and Imai, 1984; Jain et al., 2003) and data from laboratory experiments and seafloor deployments (Cook, 2015) suggested that the true value of α is different than the value provided by DH Instruments. The cumulative thermal expansion pressure effect is listed in Table 3.6.

The PRT temperature is a combination of two responses: the PRT temperature-resistance (*T*-*R*) response and the ThermOptics DN405 resistance temperature detector signal controller resistance-voltage (*R*-*V*) plus analog-to-digital (A-D) converter response. The two responses of the 100-ohm Fluke PRT (SN 999) temperature measurements were calibrated in April 2016. The temperature and resistance response of the PRT was verified against a previously calibrated Rosemount PRT. The resistance and voltage response of the DN405 and A-D was calibrated using a decade resistor module (DRM). The cumulative PRT temperature-voltage response (*T*-*V*) was determined from the combination of those two calibrations. The Fluke PRT used in the ASCPR (SN 999) previously had significant offsets in the temperature measurements, which were traced back to the use of the PRT and DN405 nominal coefficients.

The *T*-*R* response of the ASCPR PRT was calibrated against a Rosemount 162CE PRT (SN 3058,100419), which was calibrated in January 2015 using the ITS-90 standards of the triple point of water and a Gallium melt-point cell. That PRT was found to be accurate to better than ±0.03°C over a range of 0°C to 29°C and ±0.01°C from 5°C to 25°C. The two PRTs were vertically suspended side-by-side in a water bath whose temperature was controlled using a TRONAC PTC-41 controlled and Fisher-Scientific ISOTEMP1028S circulating chiller, and then covered with an insulating lid. We assumed that the distance between the PRTs (less than 5 cm laterally and 2 cm vertically) was small enough such that temperature gradients in the water bath could be neglected.

The water temperature was modulated and held at fourteen points between 0.5°C and 29°C over the course of several hours. The ASCPR PRT resistance, R (Ω), was measured with an Agilent 34401A digital multimeter (SN MY47000764; calibrated by Anmar Tech. earlier in April 2016) using a four-wire connection. The Rosemount PRT temperature, T (°C), was measured and displayed on a dedicated box. A linear least squares fit to the ASCPR resistance and Rosemount temperature was used to determine the nominal resistance, R_0, and temperature sensitivity, β, of the ASCPR PRT, such that:

$$R = R_0 + \beta T \tag{3.8}$$

Fluke provided values of 99.998 Ω for R_0 and 0.3896 Ω/°C for β. We determined values for R_0 of 100.013 ± 0.001 Ω and β of 0.3896 ± 0.0001 Ω/°C. The difference in the nominal resistance corresponded to a temperature difference of 0.039°C.

The R-V response of the ThermOptics DN405 and A-D were calibrated using a DRM (SN 121963) connected to the ASCPR circuit board. The actual DRM resistances were previously measured to ±0.02 Ω using a four-wire connection to the Agilent 24401A digital multimeter. Then the DRM was connected to the four-wire PRT pins on the circuit board and resistances from 98.0 Ω to 110.0 Ω (corresponding to a temperature range of -5°C to +25°C) in 0.2 Ω increments were tested every 30 seconds. The voltages recorded by the ASCPR were recorded to a laptop and then trimmed to remove transients caused by adjusting the DRM. A linear regression to the DRM resistances and voltages measured by the ASCPR was used to determine the voltage-resistance relationship:

$$V = \varepsilon R + V_0 \tag{3.9}$$

where ε is the sensitivity (V/Ω), R is the input resistance (Ω), and V_0 is the nominal voltage at 0 Ω. The calculated values of ε and V_0 were 2.5776 ± 0.0005 mV/Ω and 11.27 ± 0.06 mV respectively, which were updated slightly from the previous values of 2.578 mV/Ω and 11.49 mV. These values roughly corresponded to a 0.07 Ω, or 0.027°C, difference in the PRT values, which was still within the objective ±0.1°C accuracy.

Finally, the complete T-V solution for the entire PRT pathway was determined by combining equations 3.8 and 3.9 and rearranging the result to the form:

$$T = (V - V_{\text{null}})\lambda \tag{3.10}$$

Where V_{null} is the null voltage (V) and λ is the sensitivity (°C/V). We calculated a value of V_{null} of 0.246526 ± 0.00005 V, compared to the old value of 0.24627 V and the nominal value of 0.24570 V and a value of λ of 995.9 ± 0.2 °C/V, compared to the old value of 993.8 °C/V and nominal value of 1,000.0 °C/V. Overall, the calibrations of the PRT coefficients corrected the 0.1°C offset and 0.1°C span in temperature measurements. The coefficients for converting ASCPR PRT voltage to temperature were updated to this calibration and are used to date.

In March 2018, an experiment to measure the coefficient of thermal expansion was designed and conducted. In the experiment, two model DH Instruments PC-7300-2 PGCs were tested. PGC A (SN 1466) was setup open to the laboratory while PGC B (SN 1963) was setup in an insulated, temperature-controlled housing. The temperature of PGC-A was held stable at 22 ± 1°C, while the temperature of PGC-B was varied from 2°C to 25°C. Alternating measurements of the pressure produced by PGC-A and PGC-B were recorded, and the difference in pressure was used to quantify the thermal expansion coefficient and effect on pressure of PGC-B.

Both PGCs were operated near 28,000 kPa, as equipment availability did not allow identical masses and pressures to be achieved. PGC-A used a 13.648 kg mass generating 29,254 kPa and PGC-B used three masses totaling 13.000 kg and generating 27,969 kPa. We chose to use large mass values so that the small proportional pressure changes in pressure would be more readily detectable. Both PGCs were connected to a single ram pump through a selectable manifold. The piston-cylinder temperatures were monitored using PRTs located in the mounting posts. PGC-B was open to the laboratory through a 1/4 inch port and desiccating cannister to allow it to maintain the same barometric pressure and control the humidity inside the housing. Barometric pressure, ambient air temperature, piston height, tilt, and other ancillary measurements were recorded electronically to a computer or independent sensors.

A pair of Paroscientific pressure sensors model 46K (SN 132670 and 132671) were connected to the two PGCs through a manually operated three-way valve that allowed observations of one at a time. The pressure sensors were held at room temperature (22 ± 1 °C). Over a two-week period, we varied the temperature of PGC-B from 2°C to 25°C in approximately 2 °C increments with ±0.1°C stability using a Thermo Scientific M33 circulating chiller both in an increasing and decreasing fashion. Typically, measurements were allowed an equilibration time of 12 hours before making calibration measurements to reduce the possibility of transient signals. Each session consisted of five to seven alternating, 5-minute observations of the pressures from PGC-A and PGC-B. The standard corrections in equation 3.2 were used, except for the thermal expansion term.

The pressure sensors and PGC-A temperatures were considered stable and close to the reference temperature, so those thermal effects were minimized and negligible. Therefore, the only changing variable was the temperature of PGC-B. The pressure difference:

$$\Delta P = P_{\mathrm{A}} - P_{\mathrm{B}} \tag{3.11}$$

reflected the pressure change caused by thermal expansion of PGC-B. Then fractional change in pressure due to thermal expansion, $\Delta P/P_{\mathrm{B}}$, and the PGC-temperature difference from the reference temperature, T_0, were used to estimate a coefficient of thermal expansion. Figure 3.1 plots the fractional pressure change against the PGC-B temperature change. A linear least squares fit was used to estimate the slope, whose value is the areal coefficient of thermal expansion. The slope was found to be 7.8 ± 0.2 ppm/°C. Since the pressure change due to thermal expansion depends on a factor of 2α (equation 3.7), the linear coefficient of thermal expansion, α, of the tungsten carbide piston-cylinders was determined to be 3.9 ± 0.1 ppm/°C. This is the linear coefficient of thermal expansion value used for our corrections.

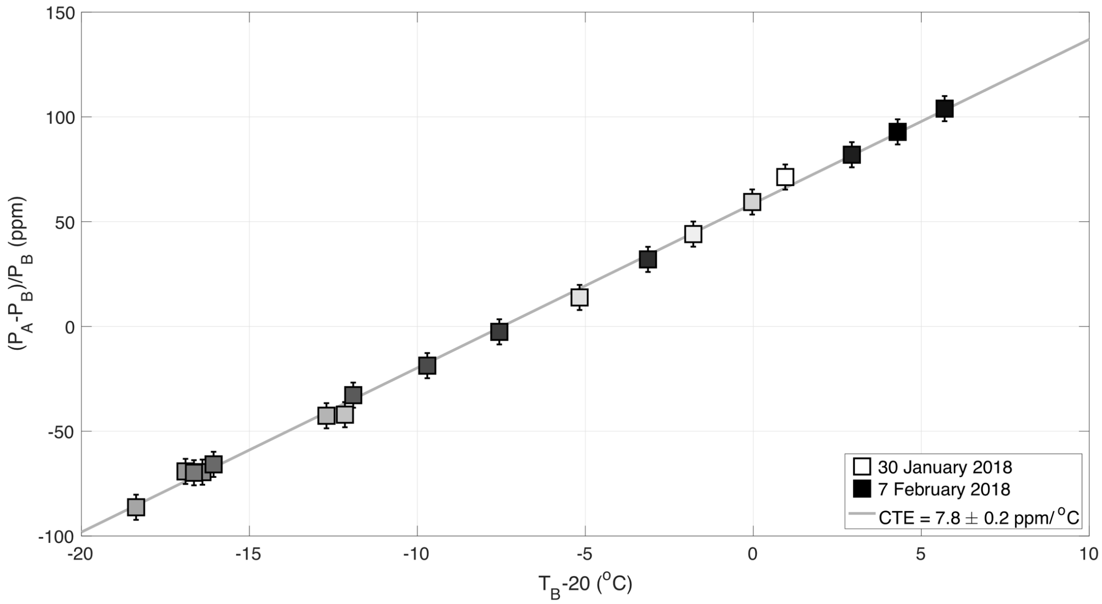

Figure 3.1 The fractional pressure difference vs. temperature change. The slope represents the areal thermal expansion coefficient.

Table 3.7 The effect of thermal expansion of the PGC cross-sectional area on the reference pressure.

Name	**Variable**	**Tungsten Carbide**
Linear Coefficient of Thermal Expansion (1/°C)	α	3.9×10^{-6}
	$\delta\alpha$	0.1×10^{-6}
Temperature (°C)	T	3
	δT	0.1
Pressure (ppm)	P	156
	δP	4.1

3.3.6 Buoyancy

The air displaced by the mass produces a positive buoyant force reducing the effective mass force applied on the PGC. The buoyancy force can be described using the ratio of the densities of two materials. The difference between the initial force and the density ratio-scaled force represents the net force. In the pressure equation, it can be expressed:

$$P = \frac{M\left(1 - \frac{\rho_{\mathrm{air}}}{\rho_{\mathrm{mass}}}\right) g}{A_0}$$

$$= P_0 \left(1 - \frac{\rho_{air}}{\rho_{mass}}\right) \tag{3.12}$$

The densities of the air and mass can be determined or are known, and the total buoyancy effect can be controlled at the level of a few ppm. The buoyancy over time is considered very stable, since the density of the mass is constant, and the density of the air may change very slowly due to drift in the internal barometer.

We can calculate the air density inside the ASCPR using the ideal gas law. The air inside is partially evacuated and backfilled with nitrogen gas five to seven times before deployment and we assume that the air inside is completely dry. We use the ideal gas law with the specific gas constant for dry air, $R_{\mathrm{dry\ air}}$ (J kg^{-1} K^{-1}), temperature, T (K), and internal air pressure, $P_{\mathrm{barometric}}$ (Pa), to calculate the air density, ρ_{air} (kg/m^3).

$$\rho_{\mathrm{air}} = \frac{P_{\mathrm{barometric}}}{R_{\mathrm{dry\ air}} T} \tag{3.13}$$

Nominally, the internal air pressure is about 75 kPa and the internal air temperature is about 3 °C; these values are actually measured in situ during each calibration. $R_{\mathrm{dry\ air}}$ has a value of 287.058 J kg^{-1} K^{-1}. Therefore, we find a nominal air density of 0.946 kg/m^3. Given the uncertainties of the actual measurements of internal air pressure and temperature, the uncertainty in the air density is ±0.001 kg/m^3.

The density of the mass depends on the material used, but typical ranges of values are known for specific grades of metals. The masses are machined out of 304 stainless steel or 6061 aluminum. This grade of stainless steel has a density of 7920 kg/m^3 and the aluminum is 2700 kg/m^3. Variations in the metallurgy process can produce slight difference in densities for the same material. Uncertainty estimates of 100 kg/m^3 for 304 stainless steel and 25 kg/m^3 for 6061 aluminum are used.

Table 3.7 lists the values and uncertainties for the buoyancy effect on the reference pressure for the two types of metals. The signal is about 119 ppm of the total reference pressure when using stainless steel and 350 ppm when using aluminum. The absolute pressure uncertainties attributed to buoyancy are about 1.5 ppm for stainless steel and 3.3 ppm for aluminum. The stability is less than 1 ppm for both materials.

Table 3.8 Two examples of buoyancy of the aluminum and stainless steel masses and the effect on the reference pressure.

Name	Variable	304 Stainless Steel	6061 Aluminum
Density, air (kg/m^3)	ρ_{air}	0.946	0.946
	$\delta\rho_{\text{air}}$	0.001	0.001
Density, mass (kg/m^3)	ρ_{mass}	7,920.	2,700.
	$\delta\rho_{\text{mass}}$	100.	25
Pressure (ppm)	P	119	350.
	δP	1.5	3.3

3.3.7 Tilt of the Piston-Gauge Calibrator

The orientation, or tilt from vertical, of the instrument affects a number of measurement parameters, notably the reference pressure produced by the PGC. The pressure depends on the component of the g vector aligned with the cylinder axis. An angular offset translates to a gravitational acceleration vector not in line with the PGC wherein only a component of the vector is used to calculate the mass force. A 0.1° tilt contributes less than 2 ppm to the total pressure while the uncertainty, assuming a tilt uncertainty of 0.1°, is greater – a few ppm. The tilt is considered very stable, even in areas of high expected tectonic tilt rates, which are still below the tilt sensor accuracy – hundreds of microradians per year – and correspond to better than 1 ppm stability.

The ASCPR has internal tilt sensing and leveling systems. The instrument itself can level up to ±10° in each of two components, though accommodating these angles has not been necessary. A Jewell model 900 biaxial tilt sensor (SN 12028) accurate to 0.1° measured the tilt and the gimbaled internal frame corrected the orientation to within 0.1°.

The vertical component of the gravitational acceleration can be calculated using the cosine of the angle from vertical. We can use the small angle approximation for cosine to calculate the projection of the gravitational acceleration, g, or more simply, the total nominal PGC pressure, P_0:

$$\begin{aligned} P &= \frac{Mg\left(1 - \frac{\theta^2}{2}\right)}{A_0} \\ &= P_0\left(1 - \frac{\theta^2}{2}\right) \end{aligned} \tag{3.14}$$

Values of the tilt, uncertainty, and the total pressure effect are listed in Table 3.8. An example tilt of 0.1° (1.8×10^{-3} radians) is used, which corresponds to the maximum tilt permitted to initiate a calibration.

Table 3.9 An example of a PGC tilt and its effect on the reference pressure.

Name	Variable	Effect
Angle (radians)	θ	1.8×10^{-3}
	$\delta\theta$	1.8×10^{-3}
Pressure (ppm)	P	1.6
	δP	3.2

3.3.8 Elastic Deformation of the Piston

The piston assembly is subject to elastic deformation caused by high pressures exerted on it. Under pressure, the piston and cylinder deform such that the cross-sectional areas change proportionally to the materials' elastic deformation constants, b, and the fluid or operating pressure, P_{fluid}. The deformation causes an area change which affects the total reference pressure in the amount of:

$$\begin{aligned} P &= \frac{Mg}{A_0(1 + bP_{\text{fluid}})} \\ &= P_0 \frac{1}{(1 + bP_{\text{fluid}})} \end{aligned} \tag{3.15}$$

The total pressure effect is proportional to the acting fluid pressure, which depends on the deployment depth. The effect contributes less than 1 ppm to the total pressure and absolute uncertainty and stability values that are negligible (i.e., less than 1 ppm).

The elastic deformation constant, *b*, depends on material properties of the piston and cylinder. The deformation constant can be written:

$$b_{\mathrm{i}} = \frac{3(\mu - 1)}{Y} \tag{3.16}$$

where *b* is the total elastic deformation. It is made of tungsten carbide, which has a Poisson ratio, μ, of 0.218 and a Young's modulus, *Y*, of 6.2×10^{-11} N/m^2 specified by the manufacturer. We calculated a value of -1.12×10^{-12} Pa^{-1} and assume an uncertainty of 10%.

It is important to note that even though the deformation affects the cross-sectional area, the expression can be simplified such that the nominal area factors out. As a result, the elastic deformation effect is independent of the cross-sectional area and therefore the specific PGC model used. However, the pressure change also depends on the acting fluid pressure, which is typically close to the nominal reference pressure, P_0. The resulting proportional pressure change (ppm) varies depending on the magnitude of the fluid pressure and therefore the operating depth. Table 3.9 lists the values used to calculate the piston deformation effect on the PGC reference pressure. The table applies to both model PC-7300-200 and PC-7200-2 PGCs. Two example depths of 100 m (1,000 kPa) and 3,000 m (30,000 kPa) are used to illustrate the magnitude of the deformation effect.

Table 3.10 Two examples of the elastic deformation effect on the reference pressure.

Name	**Variable**	**Low pressure**	**High pressure**
Deformation constant (Pa^{-1})	b	-1.12×10^{-12}	-1.12×10^{-12}
	δb	0.11×10^{-12}	0.11×10^{-12}
Example Depth		**100 m**	**3,000 m**
Nominal pressure (kPa)	P_0	1,000.	30,000.
Fluid pressure (kPa)	P_{fluid}	1,000.	30,000.
	$\delta P_{\mathrm{fluid}}$	0.1	0.1
Pressure (kPa)	P	1.1×10^{-6}	1.0×10^{-3}
	δP	1.0×10^{-7}	1.0×10^{-4}
Pressure (ppm)	P	1.1	0.03
	δP	0.10	0.00

3.3.9 Surface Tension of the Oil Medium

An additional force is produced by the surface tension of the pressure carrying fluid in the piston-cylinder annulus. It is proportional to the surface tension of the fluid, γ, and the circumference of the piston, C. The surface tension force depends on the specific PGC used but is independent of and much less than the dominant mass force such that its total effect on the reference pressure is very small. The surface tension pressure is expressed as an additional term, not as a proportional factor, in the reference pressure equation and can be isolated as:

$$P_{\text{surface tension}} = \frac{\gamma C}{A_0} \tag{3.17}$$

Its total effect depends on the specific model and size of the PGC used and its proportional effect depends on the deployment depth. At shallow depths, the surface tension effect is on the order of 10 ppm with an accuracy of a couple ppm while at deeper depths, its effect is less than a few ppm and its uncertainty is less than 1 ppm. We assume the PGC size and oil properties do not change over time and therefore the surface tension contributes zero effect to the stability of the reference pressure.

We use two different PGC models for different deployment depths. At depths of a few hundred m or more, we use a high-pressure PGC with a small cross-sectional area that nominally produces 2 MPa/kg (model PC-7300-2, SN 1963). In shallower waters of 100 m or less, we use a larger, lower pressure PGC that generates 200 kPa/kg (model PC-7300-200, SN 1791). Both models use diethyl hexyl sebacate oil as the pressure carrying medium. Since two different PGCs are used, each produces a different surface tension effect.

The additional pressure due to surface tension does not scale with pressure (i.e., depth). For example, using the PC-7300-200 PGC at a 100 m water depth, the surface tension effect is 0.015 kPa, or 0.15 cm, and the pressure uncertainty is 0.002 kPa, or 0.2 cm, which correspond to a 15 ppm effect and 2 ppm uncertainty. At a depth of 1,000 m, the effect is still 0.015 kPa and the uncertainty is still 0.002 kPa, which instead represent a 0.5 ppm effect and less than 0.1 ppm uncertainty. Table 3.10 below summarizes the important values used to calculate the surface tension effect.

Table 3.11 The surface tension effect on reference pressure for each of the two PGC models.

Name	Variable	PC-7300-200	PC-7300-2
Surface tension (N m)	γ	0.031	0.031
	$\delta\gamma$	0.003	0.003
Circumference (m)	C	2.48198×10^{-2}	7.84839×10^{-3}
	δC	3×10^{-8}	2×10^{-8}
PGC Area (m^2)	A_0	4.90216×10^{-5}	4.901758×10^{-6}
	δA_0	6.9×10^{-10}	1.2×10^{-10}
Pressure (kPa)	P	0.015	0.050
	δP	0.002	0.005
Example Depth		**100 m**	**3,000 m**
Pressure (ppm)	P	15	1.7
	δP	2	0.2

3.4 Additional Considerations

3.4.1 Hydraulic Head Pressure Differences

In an absolute system, careful determinations of the relative heights of the pressure sensors, PGC, and seawater input are important to take into account to produce instrument-independent pressure measurements. In the standard SCPR, measurements are relative, and we assume that the instrument remains geometrically stable throughout time and the hydraulic pressure heads do not vary with time, so this component can be neglected. The measured pressure differs from the true pressure by an amount proportional to the height difference, gravity, and density of the pressure medium (in this case, diethyl hexyl sebacate oil has a density of 912 kg/m^3). The PGC pressure is determined at a height indicated by fiducial line along the mounting post and the seawater pressure is measured from the seawater inlet. The height differences between the PGC and seawater input were determined from mechanical drawings of the mounting post, base plate, side plates, gimbaled frame, and so on. The corresponding pressure difference between the pressure sensing port and the pressure sources follows:

$$P = \rho g z \tag{3.18}$$

for given values of oil density, ρ, gravity, g, and the height offset, z.

On level a level surface, the height difference between the PGC and the seawater inlet port is 11.1 cm, approximately equivalent to 1.12 kPa, where the PGC is located above the seawater port. In most cases however, the instrument is placed on benchmarks that are not perfectly level and the internal gimbals accommodate the tilt to maintain PGC verticality. As a result, the positions of the PGC fiducial line, seawater input, and pressure sensors in space are different and the relative heights have changed. We recover the actual height differences by rotating the coordinates of these points in space along the instrument X and Y axes by the recorded tilt amounts. The height differences are used to determine the pressure head between the points.

3.4.2 Benchmark Tilt

Instrument-independent, absolute measurements also require translating not only the pressure from the PGC to the seawater port, but also from the seawater port to the benchmark surface. This correction is not needed for relative measurements, such as when using the standard SCPR. The seafloor pressure is translated from the ASCPR seawater port to the top of the benchmark using the height determined from mechanical drawings of the instrument housing and frame using equation 3.18 and the density of bottom seawater.

As previously mentioned, most benchmarks are not perfectly level, so the height from the seawater port to the center of the benchmark requires a correction similar to the hydraulic head rotation correction. The height difference on a level surface is 30.7 cm, which is equivalent to 3.10 kPa. The coordinates of the benchmark center and the seawater port are rotated in space relative to the benchmark center using the measured benchmark tilts to recover the actual height difference between the two points.

3.5 Total Accuracy and Stability of the Piston-Gauge Calibrators

Reference pressure measurements have absolute uncertainties, which are only important for accurate measurements of absolute pressure, and relative uncertainties or stabilities, which affect the ability to precisely measure pressure changes over time. The ASCPR requires total accuracy of the PGC reference pressure value to produce instrument-independent measurements of absolute seafloor pressure. The SCPR only requires stability of the PGC to reliably resolve drift and therefore pressure changes over time.

The total absolute uncertainty for the reference pressure depends on three factors: (1) the PGC model (i.e., PC-7300-200 or PC-7300-2), (2) the mass value, and (3) the mass material. Table 3.11 summarizes the uncertainties of the individual components of the reference pressure. Each of the individual reference pressure uncertainties were propagated together as a quadrature sum to determine the total uncertainty:

$$\delta P = \sqrt{\delta M^2 + \delta g^2 + \delta A_0^2 + \ldots} \tag{3.19}$$

However, the uncertainties for the barometric pressure and the surface tension are defined, non-proportional values. The total measurement uncertainty is given for three scenarios: (1) a shallow water measurement at 100 m, (2) a medium-depth water measurement at 1,000 m, and (3) a deepwater measurement at 3,000 m. In the first scenario, uncertainties for the larger PC-7300-200

PGC and a stainless steel mass were used. In the second and third, uncertainties for the PC-7300-2 PGC and a stainless steel mass were used.

At a depth of 100 m, an accuracy of about 25.3 ppm is achievable, which is approximately equivalent to 0.3 cm. In the medium depth case (1,000 m), we could achieve an accuracy of about 26.0 ppm, or 2.6 cm equivalent. In deeper water (3,000 m), we find an accuracy of about 25.6 ppm, which corresponds to about 7.7 cm. An individual measurement accuracy of 1 cm would allow us to reliably detect rates of 1 cm/year after two years, while 5 cm accuracy would require surveys spanning over a decade. Regardless, as the span of the time series increases, the uncertainty in the rate estimates improves.

However, if we consider using the same instrument configured with the exact same components, then the uncertainties can be vastly improved since several of the parameters become fixed. The stability, or relative uncertainty, of the reference pressure depends only on a subset of the accuracies listed in Table 3.11. The mass, PGC area, buoyancy, elastic deformation, gravitational acceleration, and surface tension effects should not change at a significant level on timescales between an individual calibration and the duration of the instrument's deployment. However, the thermal expansion, tilt, and barometric pressure effects vary at a significant level on those timescales. Therefore, they contribute toward the total relative uncertainty or stability of the reference pressure. We do not account for the gravity tides, which have an amplitude of 300 μGal, are aliased between measurements. We also assume that secular changes in gravity are negligible. The tilt of the instrument may change by about 0.02°/year over a period of months at an underwater volcano but could change as much as 0.1° over the course of one day during peak activity (Nooner and Chadwick, 2016). In subduction zones, we would expect secular tilt of the seafloor or instruments would not change at a level detectable by our tilt sensors. The thermal expansion of the PGC area, which depends on the temperature, and barometric pressure both vary on the timescale of a single calibration therefore incorporate their uncertainties into the total stability. Table 3.12 summarizes the relative uncertainties.

Table 3.12 The total accuracy of the reference pressure measurements. Some uncertainties depend on a specific mass, PGC, or material, so different combinations that reflect our usage are given.

Name	**Variable**	**Accuracy (ppm)**	**Example: 100 m**	**Example: 1,000 m**	**Example: 3,000 m**
Mass	M	(Minimum 14.648 kg) 0.9	3.7	4.3	0.9
		(Maximum 3.029 kg) 4.3			
Gravitational Acceleration	g	1.9	2.3	2.3	2.3
PGC Area	A	(PC-7300-200) 14	14	25	25
		(PC-7300-2) 25			
Thermal Expansion	$[1+2\alpha(T - T_0)]$	4.1	4.1	4.1	4.1
Buoyancy	$\left(1 - \frac{\rho_{\text{air}}}{\rho_{\text{mass}}}\right)$	(Stainless Steel Mass) 1.5	1.5	1.5	1.5
		(Aluminum Mass) 3.3			
Tilt	$\left(1 - \frac{\theta^2}{2}\right)$	1.6	1.6	1.6	1.6
Elastic Deformation	$(1+bP_0)$	(PC-7300-200) 1.1	1.1	0.1	0.03
		(PC-7300-2) 0.03			
Surface Tension	γC	(PC-7300-200) 0.002 kPa	2	0.5	0.17
		(PC-7300-2) 0.005 kPa			
Barometric Pressure	P_{baro}	0.02 kPa	20.	2.0	0.67
Quadrature Sum Total (ppm)	—	—	**25.3**	**26.0**	**25.6**

Table 3.13 The total relative uncertainty of the reference pressure measurements.

Name	**Variable**	**Accuracy (ppm)**	**Example: 100 m**	**Example: 1,000 m**	**Example: 3,000 m**
Gravitational Acceleration	g	1.9	2.3	2.3	2.3
Thermal Expansion	$[1+2\alpha(T - T_0)]$	4.1	4.1	4.1	4.1
Tilt	$\left(1 - \frac{\theta^2}{2}\right)$	1.6	1.6	1.6	1.6
Barometric Pressure	P_{baro}	0.02 kPa	20.	2.0	0.67
Quadrature Sum Total (ppm)	—	—	**20.6**	**5.4**	**5.0**

When the same instrument is used, some uncertainties drop out and the total uncertainty decreases. At a depth of 100 m, we can achieve measurements with about 20.6 ppm uncertainty, which is approximately equivalent to 0.2 cm. In a medium depth case (1,000 m), we could achieve about 5.4 ppm, or 0.5 cm equivalent. In deeper water (3,000 m), we find an accuracy of about 5.0 ppm, which corresponds to about 1.5 cm. An individual measurement accuracy of 1 cm would allow us to reliably detect rates of 1 cm/year after two years, while 5 cm accuracy would require surveys spanning over a decade. Regardless, as the span of the time series increases, the uncertainty in the rate estimates improves.

The statistical noise of the recording electronics is not included in the uncertainties described here, but it is incorporated into the quadrature sum of data analyses. In a typical 10-minute session, the root-mean-square statistical noise is about 0.1 kPa.

3.6 Acknowledgements

Chapter 3, in part, was published in IEEE Access: **Sasagawa, G. S., M. A. Zumberge, and M. J. Cook (2018), Laboratory Simulation and Measurement of Instrument Drift in Quartz-Resonant Pressure Gauges, *IEEE Access*, 6, 57334-57340, https://doi.org/10.1109/ACCESS.2018.2873479**. The dissertation author is a contributing investigator and author of this paper.

We would like to acknowledge Jerome Paros for suggesting a test of the monitor crystal system and providing insight into the physical mechanisms of pressure sensor drift. We also acknowledge William Wilcock for providing an additional number of gauges for testing. Additional technical support and guidance was provided by Douglas Alden, Carl Mattson, and David Price. Funding was provided by the National Science Foundation under award OCE-1536424.

Chapter 4

Drift-Corrected Pressure Records at Axial Seamount

4.1 Background

Axial Seamount, otherwise known as Axial Volcano, lies on the Juan de Fuca Ridge approximately 460 km off the coast of Oregon. It is an active submarine volcano that has erupted three times in the last twenty years, most recently in 2015. Presently, it is a site of considerable scientific interest, having hosted a number of interdisciplinary geophysical, geochemical, biological, and geodetic studies.

The center of the Axial Seamount caldera is located at 45.96 N, -130.01 E. The caldera is about 3 km across and 7 km long and sits at depth of about 1,500 m. The caldera walls rise up to a depth of 1300 m and the surrounding basin is approximately 1700 m deep. Figure 4.1 shows a map of Axial Seamount.

The volcano erupts frequently and hosts several hydrothermal vent fields in the caldera and surrounding region. Many of the vent fields have been surveyed and sampled extensively since its discovery. The crust is young and thin, so it is believed that the volcanic inflation and deflation may follow a more regular eruptive pattern. The magma chamber has been imaged using multichannel seismic (MCS) data (Arnulf et al., 2014; Arnulf et al., 2018). AUV-based repeat bathymetry surveys to monitor ground deformation have been done since 2006 (Caress et al., 2012). Geodetic monitoring of the eruptive cycle using BPRs has been conducted since 1987, with the introduction of MPR surveys starting in 2006, and a 2-year deployment of our SCPR in 2013 (Chadwick et al., 2006; Nooner and Chadwick, 2016; Sasagawa et al., 2016). These provided estimates on the magma chamber and also input to eruption forecasts. Several geodetic and seismic instruments – BPRs, tiltmeters, OBS, self-calibrating tilt and accelerometer, and our SCPR – were installed on the OOI Cabled Array spanning the central and eastern parts of the caldera and surrounding region to the south. These instruments provide continuous, real-time data that benefit volcanic and seismic monitoring at Axial Seamount and act as a valuable instrument testbed.

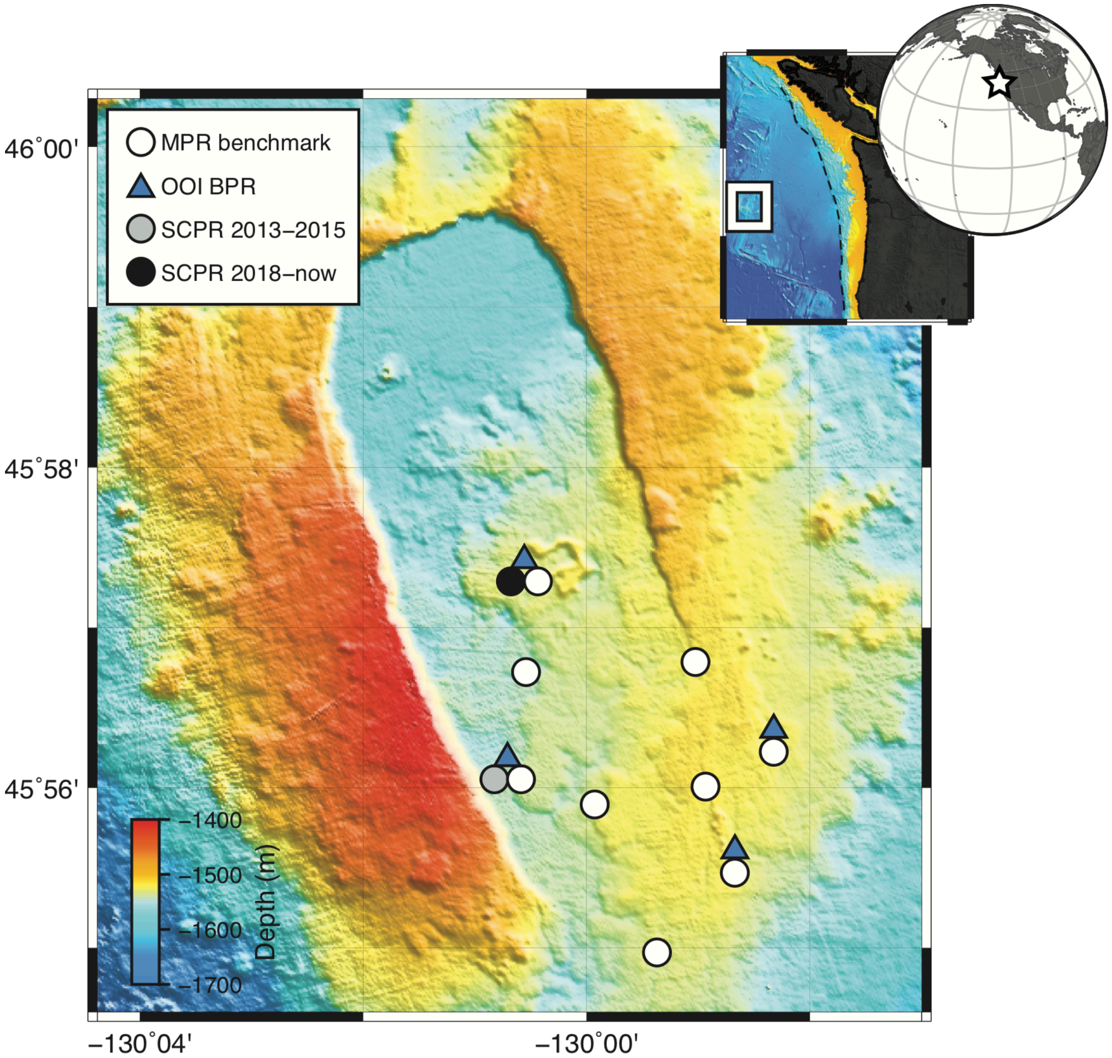

Figure 4.1 A map of some of the long-term instrumentation and benchmarks at Axial Seamount. The original SCPR (unit 001) deployment is shown by a grey circle and the recent installation of the SCPR (unit 001) on the OOI Cabled Array is shown by a black circle.

Axial Seamount is a site of ongoing and continuing research. A follow-up to the 2002 MCS cruise is planned for June 2019. Continued pressure measurements and MPR surveys to monitor the volcano are planned for 2020 and 2022. The installation of additional principal investigator-owned A0A sensors at the central caldera adjacent to the existing instruments is planned for 2021 and beyond.

4.2 2013 – 2015 Deployment

The first SCPR (unit 001) was deployed at Axial Seamount on 7 September 2013 at 45.93438 N, -130.01178 E to a depth of 1,540 m. This is located in the southwestern region of the caldera near the Axial Seamount Hydrothermal Emissions Study (ASHES) vent field and shown in Figure 4.1. A subset of the data was acoustically recovered in 2014. The instrument was released to the surface by the ROV Jason and recovered on 23 August 2015 after a 24-month long deployment. Figure 4.2 is a photograph of the instrument before its recovery.

The instrument weighed 135 kg in air, or 32 kg in water, including the frame, anchor, batteries, and floats. The frame had an outer diameter of 90 cm. The pressure housing is comprised of two anodized aluminum hemispheres, 2.5 cm thick, with eight penetrator ports made of either brass or aluminum that were evenly spaced around the bottom hemisphere. Three of the penetrators were used to connect the electrical lines and hydraulic lines open to seawater pressure. The penetrator ports were not electrically insulated from the hemisphere and rather relied on sacrificial zinc anodes attached to the base of the pressure hemisphere to prevent galvanic corrosion between the dissimilar metals. Due to the placement of the sacrificial anodes far from the contacts between the penetrator ports and hemisphere, the brass penetrators experienced corrosion. Several of the penetrator ports were corroded and one in particular corroded significantly enough to allow the slow and intermittent ingress of seawater into the pressure case. Additional sacrificial anodes were attached to the painted aluminum frame as an extra measure to ensure the frame integrity was not compromised by corrosion.

It included a pair of Paroscientific pressure sensors model 410K (SN 116504 and SN 118710), a DH Instruments PC-7300-2 piston-gauge calibrator (SN 1468) that nominally produced 2 MPa/kg, and a 6.63436 kg stainless steel mass.

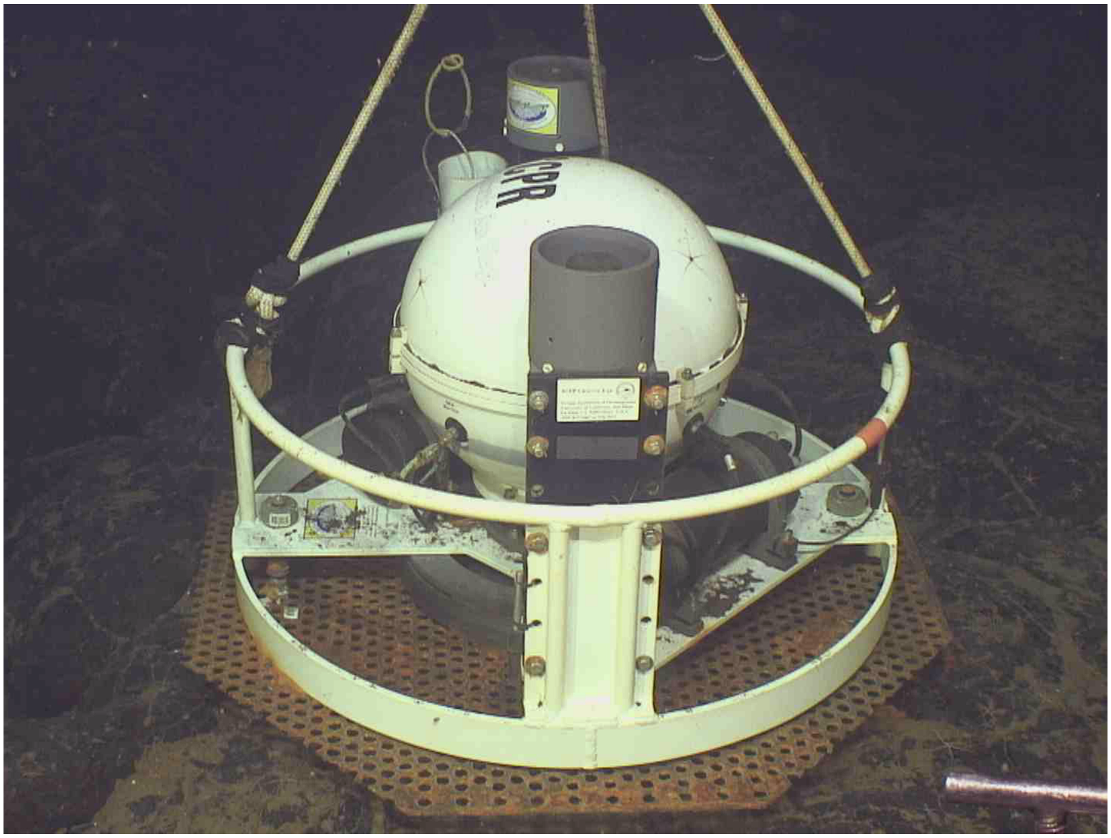

Figure 4.2 A photograph of the SCPR deployed near the ASHES vent field prior to its recovery. The frame is covered with small amounts of volcanic ash from the 2015 eruption.

4.2.1 Data

The SCPR recorded the Paroscientific pressure and temperature periods integrated over 100-second intervals. Auxiliary PRT temperature, barometric pressure, tilt, piston rotation rate, and piston cylinder height data were also recorded during calibrations. Initial calibrations were performed upon deployment and then scheduled regularly once every 20 days for a period of 20 minutes. The data were written to a compact flash memory card located on one of the main circuit boards.

Pressure measurements and calibrations occurred successfully for the first 12 months. At some point between 7 October 2014 and 27 October 2014, galvanic corrosion between a brass electrical penetrator and the anodized aluminum pressure case allowed an intrusion of seawater to enter the instrument. An increase in internal air pressure observations was consistent with the intrusion of 0.7 L of seawater. A second intrusion of 0.6 L of seawater was observed between 20 January 2015 and 9 February 2015. After February 2015, one of the two pressure sensors exhibited unexpected offsets in both pressure and temperature, rendering its data unusable after this point, which we attributed to the seawater intrusion. An additional 0.3 L of seawater entered after internal air pressure observations ceased in March 2015 or during the recovery to the surface. Inspection after recovery revealed the corrosion and about 1.6 L of seawater at the bottom of the pressure case.

Around 21 November 2014, the second Paroscientific pressure sensor (SN 118710) experienced spurious offsets and anomalous behavior, likely due to the seawater. About 19 months after deployment on 21 March 2015, both of the pressure sensors were cut off from both seawater and calibration pressure sources. We considered this duration to be the full-length record of the pressure data. The batteries were mostly depleted and the low battery voltages prevented the motor-controlled selector valve from rotating out of the closed position. We considered this the end of the pressure data, even though the sensors continued to record temperature until the SCPR was recovered.

We assumed a pressure sensor drift function, *D(t)*, comprised of a combined exponential-linear model, as proposed by Polster et al. (2009) and Watts and Kontoyiannis (1990), in the form:

$$D(t) = Ae^{-\frac{t - t_0}{\tau}} + B(t - t_0) + C \tag{4.1}$$

Drift is common to both calibration and seawater observations and its behavior is assumed to be unaffected by switching between pressure sources of similar magnitude. Since the true calibration pressure corrected for secondary effects, $P_{\mathrm{cal}}(t)$, is stable over time, any changes in the observed reference pressure $P'_{\mathrm{cal}}(t)$, are attributed to sensor drift. The difference between the observed and the true calibration pressures, $\Delta P_{\mathrm{cal}}(t)$, revealed the drift and was used to determine the coefficients A, B, C, and τ.

$$P'_{\mathrm{cal}}(t) = P_{\mathrm{cal}} + Ae^{-\frac{t - t_0}{\tau}} + B(t - t_0) + C \tag{4.2}$$

$$\begin{aligned} \Delta P_{\mathrm{cal}}(t) &= P'_{\mathrm{cal}}(t) - P_{\mathrm{cal}}(t) \\ &= Ae^{-\frac{t - t_0}{\tau}} + B(t - t_0) + C \end{aligned} \tag{4.3}$$

We used 24 calibrations to calculate the drift rates of each sensor. Each calibration session consisted of twelve 100-second pressure samples that were averaged to a single point. Pressure values were converted to seafloor height equivalent in centimeters using a seawater density of 1030 kg/m^3 and a local gravitational acceleration of 9.814 m/s^2. The series start time, t_0, was chosen as 21 September 2013. The nonlinear drift model, *D(t)*, was fitted using a commercial

Nelder-Mead simplex search algorithm (MATLAB *fminsearch* function). The drift functions for each sensor were also removed from the seafloor pressure time series.

4.2.2 Results

Three time series with significance for the Axial Seamount region were collected and produced: seafloor pressure, calibration pressure and drift functions, and seafloor temperature. Raw seafloor pressure time series were collected and converted into equivalent seafloor height. Drift functions for each of the sensors were determined and used to correct the raw records and produce a drift-free record of seafloor height that was compared to other sensors around the volcano. The pressure sensors also recorded temperature, which was used to confirm observations made at other locations, notably the 2015 eruption.

The calibration time series and the best fitting drift functions are plotted in Figure 4.3. The calibration observation uncertainties represent the standard errors of the cumulative uncertainties described in Chapter 3.6 and statistical uncertainties. The distribution of the residuals indicates that our uncertainty estimates of the calibrations are reasonable even if the individual 100-sec pressure samples are not statistically independent. Table 4.1 presents the estimated drift coefficient values.

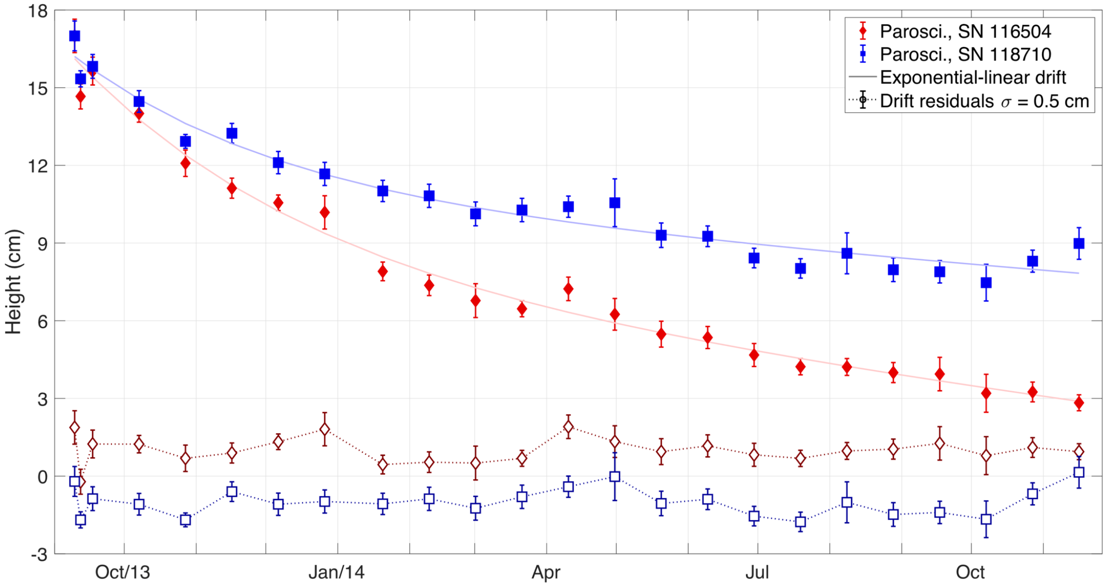

Figure 4.3 Exponential-linear pressure drift functions (solid markers and lines) and drift function residuals (open markers and dashed lines) for each of the pressure sensors. The RMS of the residuals is 0.5 cm with no distinct pattern, which supports the validity of our corrections method.

Table 4.1 Pressure drift function coefficients for the 2013 – 2015 deployment.

Combined Linear-Exponential Coefficients	**Variable**	**Sensor #1 Paroscientific 410K SN 116504**	**Sensor #2 Paroscientific 410K SN 118710**
Exponential Amplitude (cm)	A	8.1	3.4
Exponential Time Constant (days)	τ	98.6	40.2
Linear Rate (cm/year)	B	-4.4	-5.1
Offset (cm)	C	0.5	0.4

The seafloor pressure time series, converted to seafloor height equivalent (cm), were corrected for ocean tides using Some Programs for Ocean Tide Loading (SPOTL) (Agnew, 2012) and low-pass filtered using a 4th order Butterworth filter. The pressure records were trimmed to 17 months to exclude the initial temperature changes and filtering artifacts. Then, the best-fit pressure drift functions were removed. Figure 4.4 shows the seafloor pressure time series, with and without drift corrections, and the differences between the two sensors. The difference before drift corrections increased over time, which was due to different drift rates of each of the sensors. The difference after drift corrections is nearly flat, though small (~2 cm) step functions are present. These are known to be caused by artifacts of our recording system (it has since been improved), which utilized a temperature-compensated quartz oscillator whose digital compensation scheme adjusts the frequency in discrete steps as the temperature changes. Otherwise, the sensors show good agreement, which is an indication of the effectiveness of the drift correction method.

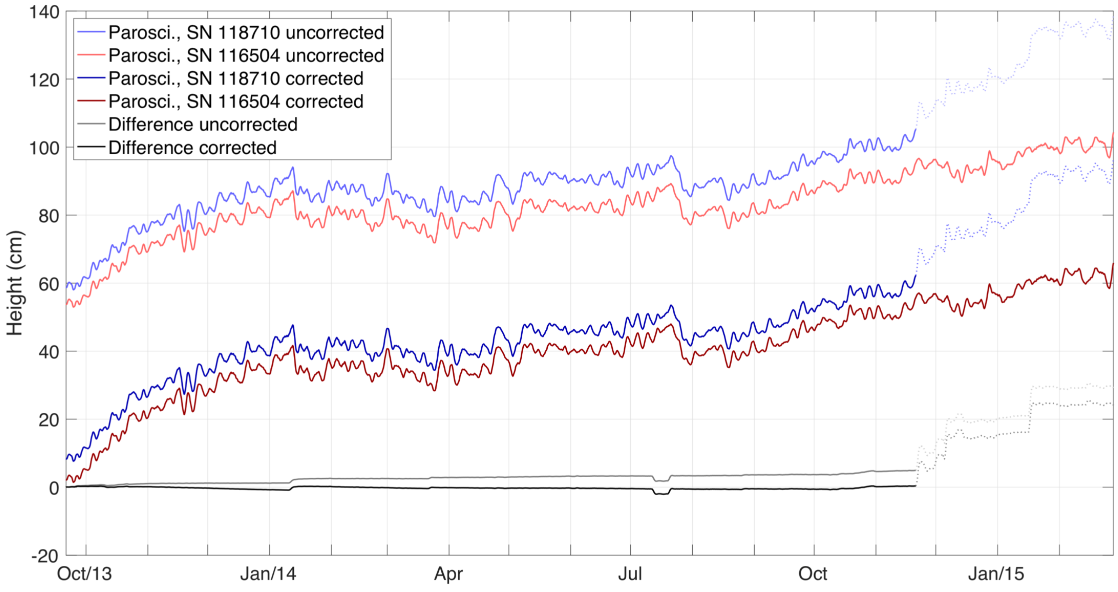

Figure 4.4 The seafloor pressure time series for each of the pressure sensors. The raw, low-pass filtered data are plotted in light red and blue. The drift-corrected, low-pass filtered data are plotted in dark red and blue. The differences between the two sensors for the raw data (grey) and drift-corrected data (black) are also plotted. The data for Parosci. SN 118710 after 21 November 2015, when the sensor showed poor behavior, are plotted with a dotted line.

Variations in the long-term inflation rate over time scales of a few months were observed, similar to measurements at subaerial volcanoes, e.g., Long Valley (Hill, 2006) and Kilauea (Poland et al., 2012). Variability and offsets over periods of weeks were also observed, which implied the signals were real physical signals, not artifacts of sensor behavior. An average deformation rate of 42.4 cm/year was measured, for a total of ~60 cm over the 17-month long pressure records. These results were compared to data from other BPRs in the volcano, some of the which were drift-corrected using the MPR method. Those data showed some similarities to our data, mostly as small events (~10 cm) and variability on the order of days to weeks. At longer periods of months and more, we interpreted differences and poorer agreement to be caused by spatial variability of deformation and differences in the calibration methods used. All of the sensors captured the rapid inflation leading up to the 24 April 2015 event. Unfortunately, the SCPR had ceased to record pressure, so we could not assess our data in eruptive and post-eruptive contexts.

The temperature time series, plotted in Figure 4.5, show expected variability on the order of 0.1 °C. A small temperature offset between the two sensors is expected and caused by imperfect temperature conversion coefficients. Following the start of the 24 April 2015 eruption, the temperature increased sharply by nearly 0.7 °C before falling back to the typical ambient seawater temperature over the next two months. The temperature response was observed in a number of other sensors throughout the volcano. It has been suggested that the temperature increases were correlated with diffuse vent activity and a slow release of heated water throughout the volcano and could potentially be attributed to the delayed response observed by Caplan-Auerbach et al. (2017).

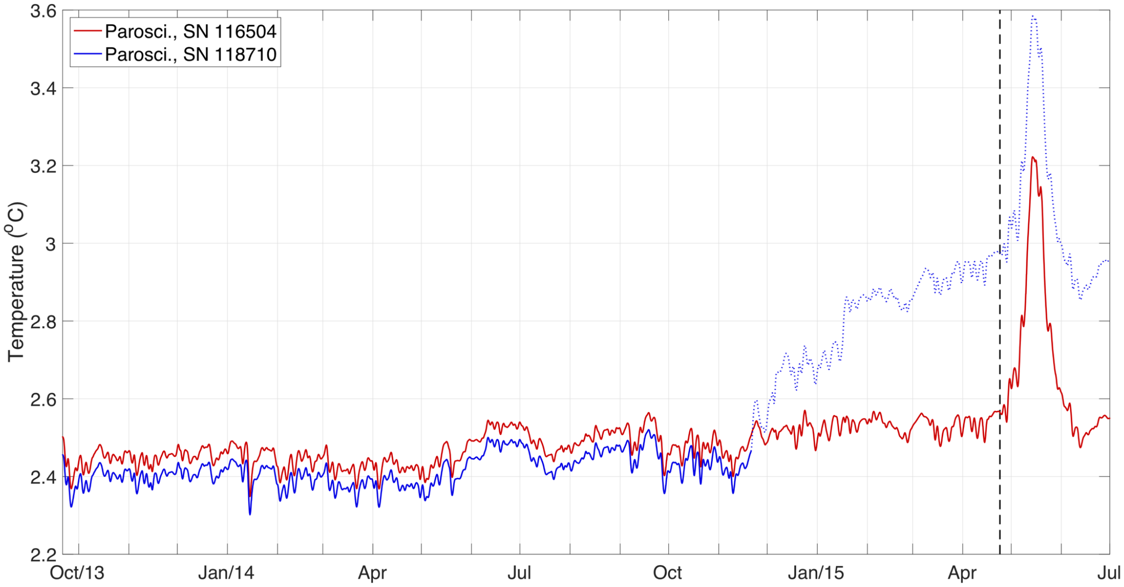

Figure 4.5 The temperature time series of the two Paroscientific pressure sensors. The temperature data for Parosci. SN 118710 when the sensor showed poor behavior starting on 21 November 2014 is plotted with a dotted line. The eruption on 24 April 2015 is indicated by the dashed black line.

4.2.3 Conclusions

The SCPR successfully demonstrated the importance of sensor drift control for geodetic seafloor pressure studies. These results represent the first continuous seafloor height time series without any ambiguities due to instrument drift. Over 60 cm of uplift was recorded over a 17-month period, corresponding to an average rate of about 42 cm/year, which would have otherwise been obscured by about 4 to 5 cm/year of instrumental drift. During this deployment at Axial Seamount, the pressure sensor drift rates for these specific two sensors were different than the measured linear drift rates from a previous deployment offshore La Jolla (Sasagawa and Zumberge, 2013). This supports the idea that drift rates can be highly variable, depend on a number of conditions such as depth and temperature, and therefore cannot be effectively characterized prior to or after a deployment.

Technical issues were encountered in the first long-term deployment, but solutions were identified that would produce longer time-series. These include addressing the corrosion between different materials by using the either aluminum or titanium consistently between the hemisphere, penetrator ports, and connections; employing an improved recording system to reduce spurious offsets in data; and increasing the size and capacity of batteries. Several of these changes were made for the subsequent installation of the SCPR on the OOI Cabled Array, which provides power and data for near-real-time monitoring capability.

No geophysical interpretation was attempted in this study. Modeling of the magma chamber is best done by incorporating deformation data collected by all of the instruments at Axial Seamount.

4.3 2018 Ocean Observatories Initiative Cabled Array Installation

Following the April 2015 eruption and the successful recovery and demonstration of the SCPR, it was funded for installation on the OOI Cabled Array at Axial Seamount to provide improved geodetic monitoring of the volcano. Several modifications to the SCPR (unit 001) were made to address previous issues and improve the overall performance and robustness of the instrument, notably the use of a new titanium pressure housing. The cabled SCPR provides near real-time data and is controlled remotely when performing calibrations or other adjustments.

The SCPR was connected to the medium power junction box located at in the Central Caldera area. It was placed about 15 m away at 45.95491 N, -130.00928 E at a depth of 1525 m shown in Figure 4.1. It is within about 20 m of a nearby bottom pressure and tilt (BOTPT) sensor and a self-calibrating tilt accelerometer, which enable valuable geodetic comparisons using different instruments.

The cabled SCPR uses a pair of Paroscientific pressure sensors model 44.4K and 46K (SN 136576 and SN 132123 respectively), which are different from the original deployment, the same SCPR DH Instruments PC-7300-2 piston-gauge calibrator (SN 1468), and the same 6.63436 kg stainless steel mass. Figure 4.6 is a photograph of the instrument in the central caldera region. A titanium pressure housing was used instead of the previous painted aluminum pressure case to reduce opportunities for galvanic corrosion to occur. Only four ports (rather than the ten originally designed) were made and used for the electrical and communications cable, the vent seal port, and hydraulic lines for seawater observations and pressurizing the PGC. The first two ports use adapters also made of titanium, greatly reducing the likelihood of galvanic corrosion. The hydraulic line adapters are made of stainless steel, but adapter spacers made of Delrin were used to isolate the titanium pressure case from the stainless steel adapters. We expect no galvanic corrosion, similar to that described in Section 4.2, to occur with these modifications in place.

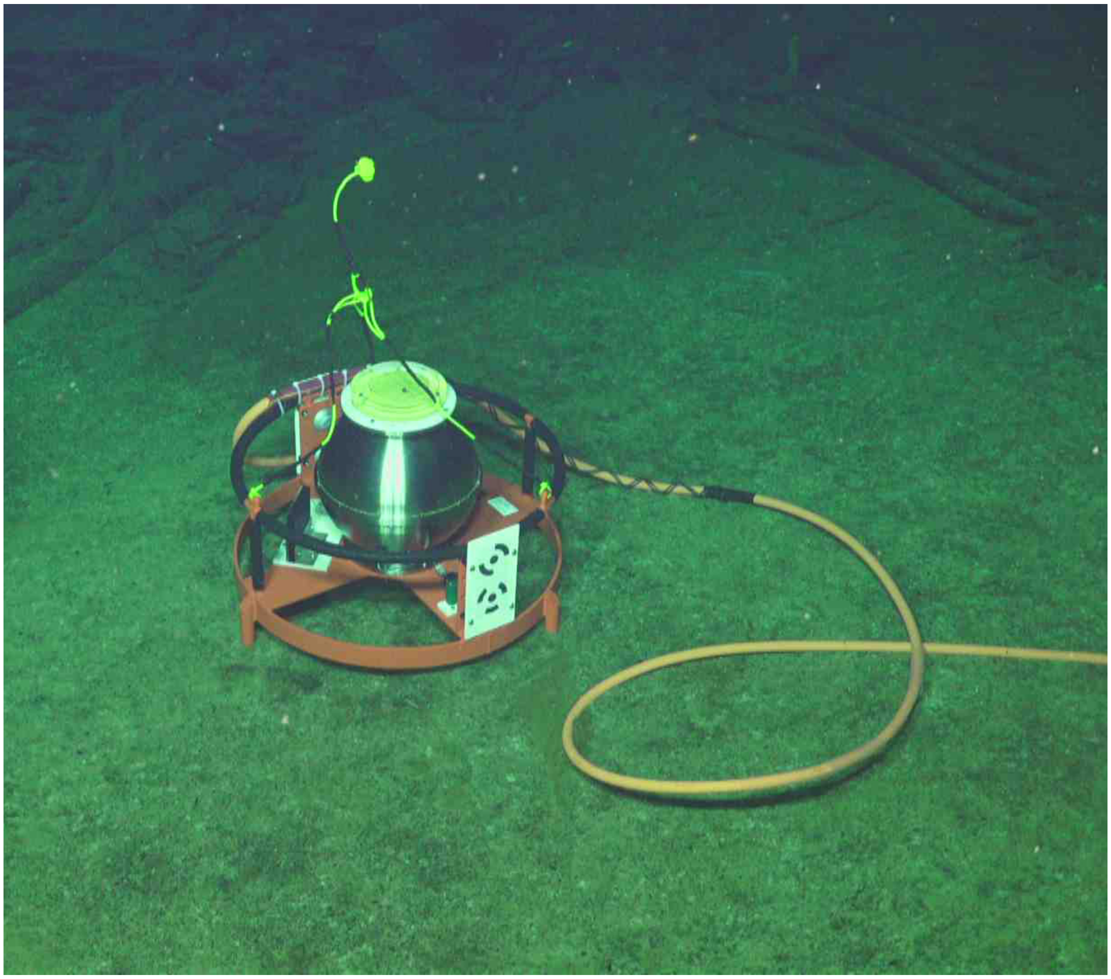

Figure 4.6 A photograph of the cabled SCPR connected to the OOI Cabled Array in the caldera center. A subsea level was installed on the top to ensure level placement within a few degrees. The cable runs about 15 m out of the photograph frame to the junction box.

4.3.1 Data

The OOI Cabled Array provides continuous power and data to the SCPR, so data can be sampled at higher rates than compared to an autonomous deployment where battery storage and capacity are important considerations. The cabled SCPR records the Paroscientific temperature and pressure periods and converted temperature and temperature-compensated pressure at 1 Hz. Additional PRT temperature, barometric pressure, and tilt data are recorded at 1 Hz. The piston rotation rate and piston cylinder height data are recorded only during calibrations to minimize unnecessary power dissipation and internal heating.

We adopted an evolving calibration schedule to accommodate an exponential-linear drift rate and the finite volume of the oil compensator. The period between calibrations started off small and increased over time. This uses oil conservatively and allows us to capture the exponential component more reliably while still collecting a sufficient number of points to constrain the linear long-term signal. The calibration interval remained the same at 20 minutes.

An initial calibration was conducted on 6 July 2018, after the SCPR was first connected to the junction box to ensure nominal performance. A second calibration as another check occurred about 14 hours later the same day. Between 9 July 2018 and 5 October 2018, calibrations occurred approximately once every 7 days. After 5 October 2018, calibrations were scheduled about once a month until 4 January 2019. Since that time, calibrations are scheduled for once every two months. As of 3 April 2019, we have performed 18 calibrations, of which 14 are considered valid. Three calibrations were removed due to the large temperature change during the first three days of deployment; one scheduled calibration was missed during the last week of August 2018 due to network-wide power failures and missing data; and one was removed because ancillary sensors were not set to a low power mode, which caused unexpectedly large temperature gradients that could not be reliably resolved and corrected.

Consistent with previous SCPR work, we assumed the same combined exponential-linear drift function. The difference between all of the corrected calibration pressures, $P_{\mathrm{cal}}(t)$, and the observed reference pressures, $P'_{\mathrm{cal}}(t)$, reveals the sensor drift, $D(t)$. The coefficients of the drift function, A, B, C, and τ, are calculated using equation 4.1.

Each calibration interval lasts ~20 minutes and produces ~18 minutes, or ~1080 data points, of usable pressure data. The pressure samples for each calibration session are corrected and then averaged to a single value. Then the calibration pressure time series is used to calculate the drift coefficients. The series start time, t_0, was chosen as 24 July 2018, corresponding to the first calibration after instrument to come to thermal equilibrium with the ocean. The nonlinear drift functions for each sensor, D(t), are fitted using a Nelder-Mead search algorithm (MATLAB *fminsearch*). The respective drift functions are removed from the seafloor pressure records, which are converted to seafloor height equivalent to produce a drift-free record of vertical seafloor deformation.

4.3.2 Results

The cabled SCPR has collected almost a year of near real-time continuous seafloor pressure data. Since then, we have performed 19 calibrations, 15 of which were used to characterize the pressure sensor drift. The temperature records from the PRT and pressure sensors are also useful for looking at variability leading up to and following eruptions.

The calibration time series and best-fit drift functions for the two pressure sensors are shown in Figure 4.7. The uncertainties represent standard errors. Since there is no distinct signal in the residuals, we believe our error estimates are appropriate even though an assumption of statistical independence is not completely valid. The residuals for each of the sensors are strongly correlated, which suggests that the observed signals are real and not attributed to sensor noise. The drifts exhibit exponential decay with a time constant of about 3 weeks, 23 days for the first sensor and 22 days for the second sensor. The long-term linear drift rates are 7.5 cm/year and 5.1 cm/year respectively. The full set of drift coefficients are listed in Table 4.2.

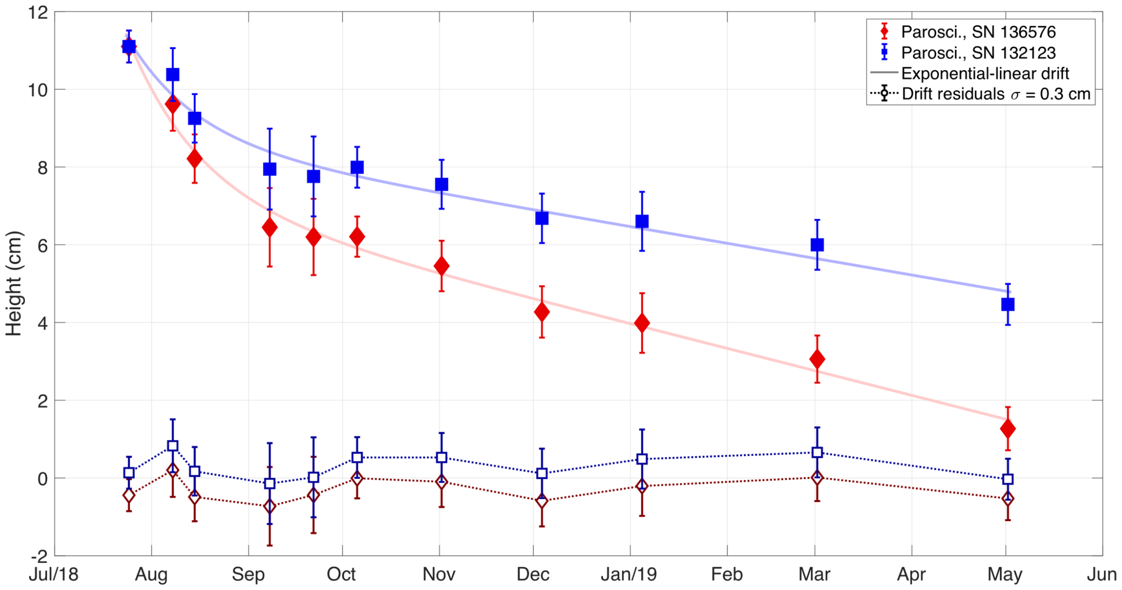

Figure 4.7 Exponential-linear pressure drift functions (solid markers and lines) and drift function residuals (open markers and dashed lines) for each of the pressure sensors.

Table 4.2 Pressure drift function coefficients for two pressure sensors in the SCPR connected to the OOI Cabled Array. The pressure sensors are different than the previous deployment, so a direct comparison of the coefficients between deployments cannot be made.

Combined Linear-Exponential Coefficients	**Variable**	**Sensor #1 Paroscientific 44.4K SN 136576**	**Sensor #2 Paroscientific 46K SN 132123**
Exponential Amplitude (cm)	A	4.0	2.6
Exponential Time Constant (days)	τ	22.7	21.8
Linear Rate (cm/year)	B	-7.5	-5.1
Offset (cm)	C	4.2	2.9

After the seafloor pressure records are corrected for sensor drift, they are corrected for ocean tides using a tidal harmonic analysis algorithm in MATLAB, t_tide (Pawlowicz, 2012). After corrections, pressure is converted to equivalent seafloor height using a seawater density of

1030 kg/m^3 and the local gravitational acceleration. The de-tided records are low-pass filtered using a FIR filter with a passband at 1.7×10^{-6} Hz (0.143 cycles/day) and a stopband at 3.9×10^{-6} Hz (0.333 cycles/day) and trimmed to remove filtering artifacts. We also calculate the difference between the two sensors, which reveals remaining differential drift or anomalous behavior between the sensors. Figure 4.8 shows the de-tided records in light colors, the de-tided and low-pass filtered records in dark colors, and the differences between the two sensors in grey (light grey represents the de-tided only difference and dark grey represents the de-tided and filtered difference).

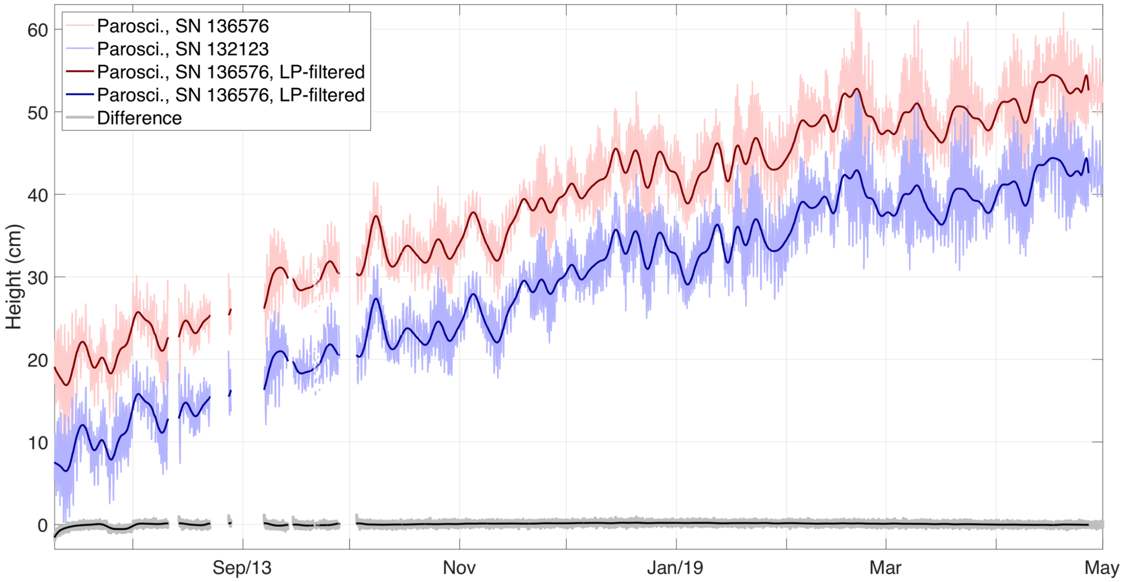

Figure 4.8 The drift-corrected seafloor pressure records converted to seafloor height equivalent. The raw data for the two sensors are plotted in light red and blue and the low-pass filtered data are plotted on top in dark red and blue. The difference between the two is plotted in grey.

The difference between the two records is essentially flat at zero after a small (~2 cm) exponentially decaying difference in the first few weeks. This supports the effectiveness of the drift correction method and the improvements since the last SCPR iteration. The disagreement in the first few weeks is likely due to unaddressed and poorly constrained exponential thermal and drift effects.

A total of 33 cm of uplift has been measured over a 9-month long period, for an average rate of 44.0 ± 0.7 cm/year. The NOAA Pacific Marine Environment Laboratory (PMEL) collects and curates geodetic data for forecasting purposes. They report 4-, 8-, and 12-week average inflation rates. When the SCPR results were compared to BPR measurements adjusted for drift using MPR surveys, deformation rate variations of several cm over a few weeks were observed in both. However, the 8- and 12-week inflation rates estimated from the SCPR at the same location and for the same time interval are consistently higher by about 20 cm/year. The discrepancy is probably due to the limited drift constraints that the MPR method provides but further comparisons are needed to verify these observations. If this result persists, then it will have an important impact on models of volcanic inflation.

The temperature records for the two pressure sensors and the internally mounted PRT are plotted in Figure 4.9. An offset of about 0.2 °C between the two pressure sensors is not unexpected and is due to the imperfect conversion coefficients. The PRT temperature curve is about 1.5 °C warmer than the temperature measured by the pressure sensors. We attribute this difference to thermal gradients within the instrument. The pressure sensors sit on the outside of the internal components and are exposed to more of the colder air in contact with the cold walls of the titanium housing. The PRT is mounted inside the bulk of the PGC mechanism and is surrounded by circuit boards that generate a small amount of heat. This additional heat coupled with the poor circulation inside the housing allows the PGC mounting post to remain slightly warmer than the pressure sensors. Overall, the temperature variations measured by all of the sensors are on the order of 0.1 °C, which agrees with typically expected seafloor temperature variations. A step in all three curves occurred in the last two weeks of July. An incorrect recording setting caused the instrument to use extra and unnecessary sensors in the background and generate additional heat that caused the internal temperature to rise. This was identified and corrected for future measurements. A seasonal signal is present, but longer records are necessary to reliably characterize the magnitude of the signal. Since there has not been an eruption since the SCPR was installed, no other signals of volcanic significance have been observed.

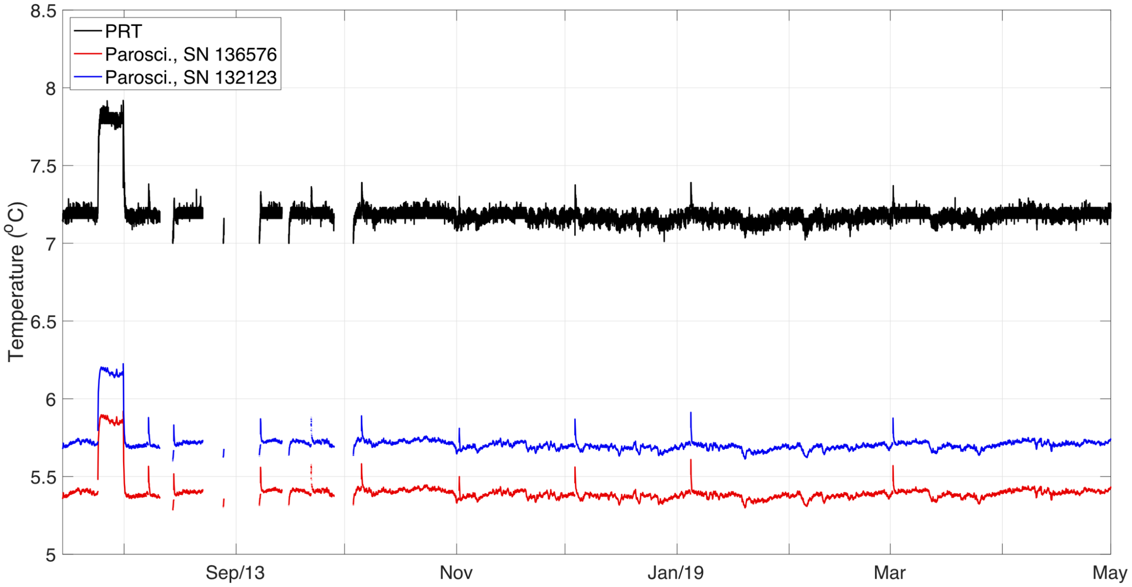

Figure 4.9 The temperature time series of the two Paroscientific pressure sensors and the PRT located inside the PGC mounting post. The offsets are real recorded differences between sensors.

4.3.3 Conclusions

The initial SCPR deployment at Axial Seamount in 2013 demonstrated the success and importance of in situ pressure calibrations for geodetic purposes. The follow-up SCPR was installed on the OOI Cabled Array to improve the geodetic monitoring work being done. The cabled SCPR has been collecting drift-corrected seafloor pressure for nearly a year and provides a valuable, calibrated reference record of vertical deformation. Thus far, we have recorded a total average inflation rate of 44.0 ± 0.7 cm/year.

Although the SCPR deformation rate differs from other drift-corrected pressure measurements based on MPR surveys over the same time period by a factor of about 2, the discrepancy likely reflects differences in the drift compensation method. The MPR method relies on the assumption that the reference station is stable, but any deformation occurring at the reference station which may vary between surveys, would be folded into a drift estimate and bias the deformation estimate. Additionally, the assumption of a purely linear drift rate could introduce additional error if a strong exponential pressure drift signal were present in any of the continuous BPRs. The current eruptive cycle model based on MPR surveys and BPR data suggests that the volcano erupts within a relatively repeatable threshold height or volume. If actual deformation rates are greater and closer to those measured by our SCPR, then this suggests that the volcano is growing in height and rather that eruptions occur at the same incremental increase in height to within a few meters, not the same height. This idea is worth investigating in the future as additional geodetic measurements at Axial Seamount are added since the existing datasets are limited.

A geophysical interpretation of the volcanic cycle and magma chamber modeling falls outside the scope of this work, but the data are being used and in conjunction with other data to guide monitoring and forecasting work at Axial Seamount done by NOAA and others. The SCPR is planned to be incorporated into future pressure surveys, since its known reference pressure could likely provide a better reference value and eliminate the need for a remote station outside of the expected area of deformation.

This project marks the third successful demonstration of the SCPR. The high-precision drift-corrected seafloor pressure, and seafloor height by proxy, data provide a valuable asset to geodetic studies in many target regions around the world. In the presence of cabled infrastructure, the continuous and real-time availability of data increase the utility of these instruments for monitoring efforts.

4.4 Acknowledgements

Chapter 4, in part, is a reformatted version of a publication in **Earth and Space Science: Sasagawa, G., M. J. Cook, and M. A. Zumberge (2016), Drift-corrected seafloor pressure observations of vertical deformation at Axial Seamount 2013–2014,** ***Earth and Space Science*****, 3(9), 381-385, https://doi.org/10.1002/2016EA000190**. The dissertation author is not the primary investigator and author of this paper. Chapter 4, in another part, is currently being prepared for submission for publication. This work is coauthored with Mark Zumberge and Glenn Sasagawa. The dissertation author is a contributing investigator and author of this material.

We thank Michael Davis, Michael Kirk, David Price, Joel White, and Heinz Wuhrmann for engineering assistance. Scientific support was provided by William Chadwick and Scott Nooner. We would also like to acknowledge the crew of the R/V Thomas G. Thompson and the ROV Jason team for their technical support and encouragement. Funding was provided by the National Science Foundation under award OCE-0851540.

We again thank Michael Kirk, David Price, and Heinz Wuhrmann for engineering assistance. We would like to thank Dana Manalang, Ken Davis, Deb Kelley, and the rest of the OOI cohort at the UW for technical assistance, guidance, and continued maintenance of the SCPR on the OOI Cabled Array. We acknowledge the crew of the R/V Roger Revelle and the ROV Jason team for the resources and support provided. Funding was provided by the National Science Foundation under award OCE-1657797.

Chapter 5

Absolute Pressure Surveys in the Cascadia Subduction Zone

5.1 Background

The Cascadia subduction zone, where the Juan de Fuca plate subducts beneath the North America plate, poses a considerable seismic and tsunami hazard to coastlines along the United States Pacific Northwest and British Columbia, Canada. It stretches nearly 1,100 km from Mendocino, CA to Vancouver Island, BC. Tsunami inundation records, turbidite flows, and paleoseismic evidence reveal that large tsunamigenic earthquakes have ruptured large areas of the subduction zone several times in the past, most recently in 1700 (Atwater et al., 1995; Goldfinger et al., 2003; Goldfinger et al., 2012; Nelson et al., 2006). The recurrence interval of large earthquakes is believed to be a few hundred to a thousand years. However, the present state of stress in the subduction zone is not well-known. More information regarding the structure and deformation of the fault are needed to characterize the seismic and tsunami hazards in Cascadia. Land-based studies investigating interseismic deformation and slow slip phenomena have increased in recent decades, but those data alone are insufficient for constraining the up-dip extent of locking distributions. A greater offshore geophysical presence is needed to be able to characterize more of the subduction zone system.

A number of marine geodetic methods including acoustics, pressure, gravity, strain, and tilt have been developed and successfully demonstrated over the last few decades. Acoustics, notably GPS- and GNSS-Acoustic, can measure horizontal motion at the cm-level and are used to measure plate motion in Japan, Cascadia, and other regions (Spiess et al., 1998; Matsumoto et al., 2008). Seafloor (ocean bottom) pressure has also been widely used to measure vertical motion and deformation of the seafloor. Seafloor pressure is a proxy for height since a 0.1 kPa pressure change corresponds to a 1 cm height change. While pressure sensors can detect mm-level signals at short periods, they are unreliable for long-term measurements spanning months or longer due to inherent drift. Pressure sensor drift contaminates and often exceeds long-term tectonic signals of interest and is difficult to reliably characterize before or after a deployment (Polster et al., 2009). Methods developed to correct sensor drift include MPR surveys, SCPRs, and recently developed A0A sensors. The MPR method requires a stable reference site outside the area of expected deformation and measures pressure changes relative to that site (Stenvold et al., 2006; Chadwick et al., 2006; Nooner and Chadwick 2009). The SCPR continuously records seafloor pressure and intermittently calibrates the pressure sensors against a reference pressure produced by a piston-gauge calibrator (Sasagawa and Zumberge, 2013; Sasagawa et al., 2016). The A0A sensor also measures seafloor pressure and intermittently vents to the internal air pressure as a reference value used to characterize sensor drift (Wilcock et al., 2018).

The SCPR was developed to address the issue of sensor drift in situ by using a mechanical piston-gauge-calibrator. The pressure sensors normally record seafloor pressure and are intermittently switched to observe the reference pressure produced by the PGC. The reference pressure value is considered stable over time and its value can be precisely determined. Changes in the reference pressure observed by the pressure sensors are therefore attributed to sensor drift. The instrument design and operation are detailed in Sasagawa and Zumberge (2013) and Sasagawa et al. (2016). In an alternative fashion, we address the metrology and measurements parameters of the full instrument against absolute standards, such as those traceable to NIST. We can therefore make instrument-independent measurements of seafloor pressure with an absolute level of accuracy that serve as individual points in long-term time series or calibration values for co-located sensors. We refer to this system as the absolute SCPR, or ASCPR.

We conducted absolute pressure surveys with an ASCPR along a trench-perpendicular profile in the Cascadia subduction zone over a four-year period from September 2014 to September 2017 to measure the vertical deformation associated with secular strain accumulation. We present the design and methods of the instrument and surveys, as well as absolute seafloor pressure values, which will serve as longstanding benchmark values for future studies and estimated secular rates.

5.2 Methods

5.2.1 Survey Profile

Absolute calibrated pressure surveys require benchmarks on the seafloor for the ASCPR to reoccupy. A series of concrete benchmarks was installed on the seafloor in a trench-perpendicular profile off of the coast of Oregon between 2014 and 2016. Figure 5.1 is a map of the locations of our benchmarks. The farthest west station, O1, is located 105 km off the coast on the Juan de Fuca Plate side of the trench at a depth of 2,900 m. The other stations, O2, O2B, O3, O4, O5, and O6, are located on the North American plate and are separated by approximately 15 km from each other heading towards shore. The closest station to shore, O6, is about 20 km off the coast at a depth of 70 m. Each station was equipped with an autonomous, continuous BPR attached to the benchmark or located within a couple meters of the site. Table 5.1 lists pertinent information for absolute pressure measurements about each site.

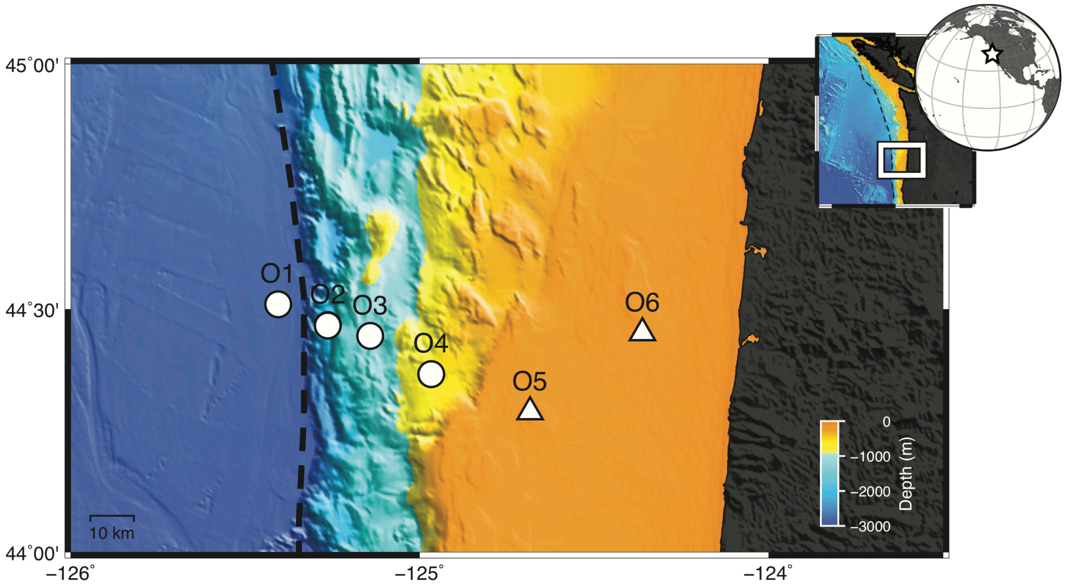

Figure 5.1 A map of the ASCPR profile located offshore Oregon at about 44.5 °N. The shape of the station marker indicates the type of seafloor benchmark at that station (standard, circular or triangular, trawl-resistant). The trench is indicated by the dashed line.

Two types of solid concrete benchmarks were used depending on the terrain and expected trawling activity in the area. The benchmarks located in deeper water where less trawling is expected (i.e., O1, O2, O2B, O3, and O4) are based on a design used for GPS-Acoustic transponders (Segawa et al., 1988; Chadwell, 2016). These are circular in shape with a diameter of 76.2 cm, have three legs about 15.2 cm tall, and weight 66.7 kg in water. The ones located at O1 and O2 have a red-orange stripe painted around the edge and three radial black lines at 120° to allow for more consistent relocation and orientation. The shallow water benchmarks (i.e., O5 and O6) use a larger, trawl-resistant design with a triangular base that slopes up to a triangular platform 71.1 cm on each side. These benchmarks weigh 354 kg in water. Figure 5.2 includes photographs of each of the types of benchmarks and Figure 5.3 includes photographs of the ASCPR making a measurement on each.

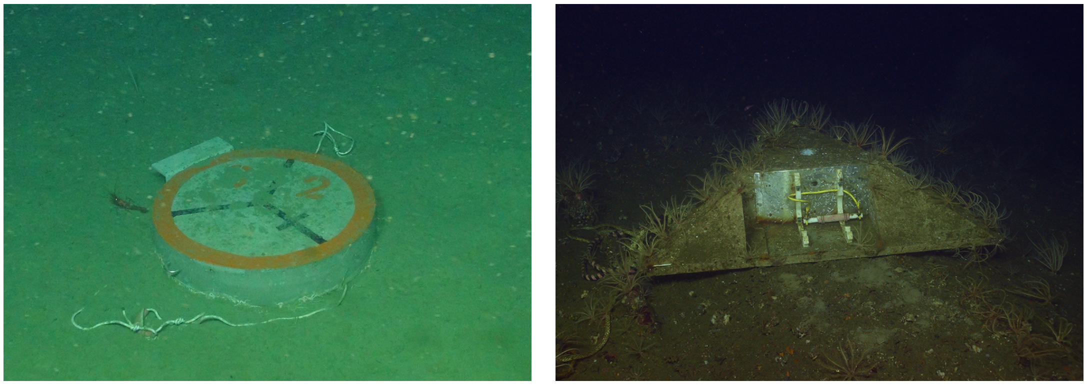

Figure 5.2 Photographs of the concrete seafloor benchmarks used for absolute pressure surveys. The left image is the circular benchmark used in waters deeper than a couple hundred meters. The right image is the triangular trawl-resistant benchmark used in shallow waters. An autonomous BPR was secured by the bungee handle in the cutout in the shallow benchmark but has since been replaced.

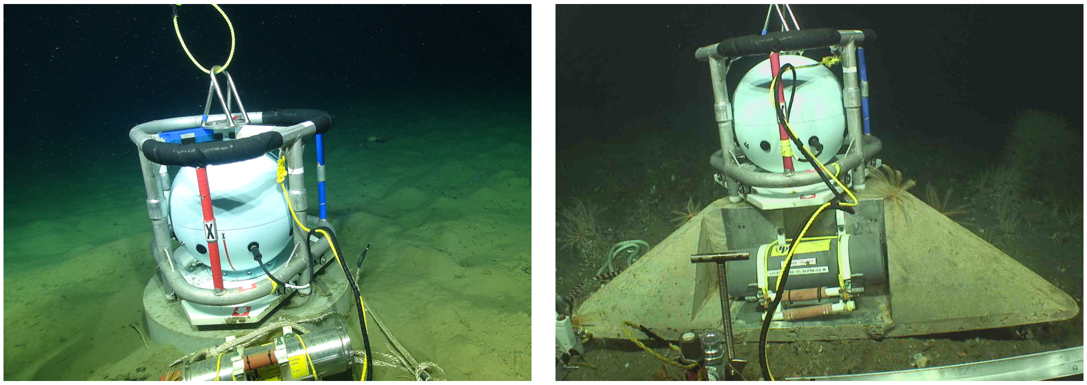

Figure 5.3 Photographs of the ASCPR making a measurement on each of the seafloor benchmarks.

The value of the gravitational acceleration was not directly measured at each location. Rather, we calculated gravity using the international gravity formula, added the EGM 2008 gravity anomaly, and translated the value from the sea surface down to the seafloor using the seawater gravity gradient, as described in equation 3.4 (Götze, 2014; Pavlis et al., 2012). These values of gravity are listed in Table 5.1.

The seafloor is covered by a relatively flat, thick layer of sediments between stations O1 and O4. The circular benchmarks were lowered over the side of the ship and released at depth.

After falling and settling into the sediments, a couple benchmarks were tilted by more than 10°, so they were adjusted using the ROV manipulators. In shallower waters, the seafloor had less sediment cover and the rocky substrate was exposed in many areas. It also appeared to be conducive to more life in the form of sessile, benthic organisms, such as those pictured in Figure 5.2. Benchmarks O5 and O6 were also placed on the seafloor over the side of the ship. The benchmarks had three points of contact near each of the corners but were not as easy to level due to the rocky bottom terrain. The total tilt of each benchmark was measured using the ASCPR and, for some benchmarks, validated with MPR tilt measurements; the values are included in Table 5.1.

Table 5.1 Location, depth, age, mass load including the PGC assembly, gravity, and tilt of the benchmarks at each station.

Station	Latitude (°N)	Longitude (°E)	Depth (m)	Established (year)	Mass (kg)	Gravity (m/s^2)	Benchmark Tilt (°)
O1	44.5099	-125.4056	2,907	2014	14.64821	9.80496	4.01
O2	44.4670	-125.2636	1,909	2014	9.53906	9.80522	0.43
O2B	44.4661	-125.2637	1,910	2015	9.53906	9.80522	0.95
O3	44.4450	-125.1418	1,315	2016	6.54441	9.80540	3.42
O4	44.3666	-124.9670	620	2016	3.02943	9.80553	0.32
O5	44.2889	-124.6838	79	2016	3.50921	9.80555	3.55
O6	44.4512	-124.3616	70	2016	3.50921	9.80555	2.78

5.2.2 Absolute Calibrated Pressure Measurements

The ASCPR is used to make campaign-style absolute seafloor pressure measurements. Like the standard SCPR, it relies on the PGC to produce a reference pressure that is used to calibrate the pressure sensors. However, absolute pressure measurements require accurate determinations of the absolute reference pressure value, not only its stability. The difference between the true reference pressure and the reference pressure observed by the pressure sensors reveals static offsets and transients attributed to the pressure sensor, which can be characterized and corrected. The same corrections are applied to the observed seafloor pressures to produce absolute seafloor pressure values.

The ASCPR is connected and tethered to an ROV and is placed on the seafloor benchmarks. Once on the benchmark, the instrument is leveled, and the mass is unlocked. The charge valve is opened to raise the piston-cylinder and mass off the bottom and closed once the piston reaches a preset height. Then the mass is spun. For the duration of the benchmark occupation, typically about 2 hours, the selector valve alternates the pressure sensors observations between the PGC and the ambient seawater for 10- to 15-minute intervals. Figure 5.4(a) shows what the collected pressure data look like for a typical ASCPR survey. The mass rotation rate and piston-cylinder are monitored and corrected as needed. At the end of the calibration period, the SV switches back to the ambient seawater, the mass is locked, and the ASCPR is recovered back to the ROV before returning to the ship or moving to the next site.

The reference pressure produced by the PGC, including higher order corrections is defined in equation 3.2. Prior to or during deployment, each of the correction terms was measured or calculated. Many of the sensors were calibrated against metrological standards, some of whose accuracies are NIST-traceable. We used the difference between the reference pressure calculated from known standards and the reference pressure as measured by a pressure sensor to determine the pressure sensor offsets and transients, which are likely due to imperfect calibrations, thermal shock, and short-term pressure sensor drift. We calculated a static offset and fit an exponential-linear curve to the pressure difference, which captures the short-term drift due to loading and thermal shock. The corrections from the observed reference pressure to the known reference pressure are then applied to the observed seafloor pressures to produce absolute seafloor pressures. Figure 5.4 (b) shows the reference pressure measurements as measured on the left and corrected according to equation 3.2. The exponential-linear curve used to estimate sensor effects is also shown. Figure 5.4 (c) shows the seawater pressure observations, including the tides on the left, and with the tides removed on the right. The fit curve is plotted over the de-tided seawater pressure and removed in the next step. Figure 5.4 (d) shows the final, corrected reference pressure and the final corrected seawater pressure. We then calculated the difference between the measured reference and seawater pressures. Finally, we used the true, absolute reference pressure, whose value we have carefully calculated, and the difference between the observations to determine the absolute seafloor pressure measured by the ASCPR.

The resulting absolute seafloor pressure is the value as measured at the base of the pressure sensor. We used instrument drawings, measurements, and orientations to translate the pressure to the center of the seafloor benchmark. First, hydraulic head differences between the reference line of the PGC and the seawater input line were calculated using the orientation of gimbaled frame and the benchmark tilt. Then, the pressure at the point of the external seawater input line was translated to the center of the benchmark using the vertical pressure gradient defined in equation 3.18. The seawater density at the seafloor was measured as 1.030 kg/m^3 using ship- and ROV-based CTDs.

Figure 5.4 Example data for an absolute pressure survey. (a) The left shows the entire series of alternating reference and seafloor pressure observations; the right shows the survey period subset. (b) The left plot (raw) shows the measured reference pressure; the middle plot (adjusted) shows the shows the pressure adjusted for terms in the reference pressure equation and the exponential-linear fit to gauge effects; the right plot (corrected) shows the pressure corrected for gauge effects. (c) The left (raw) shows seafloor pressure including tides; the middle (de-tided) shows the pressure with tides removed and the fit curve determined from the reference pressures; the right (corrected) shows the pressure corrected for gauge effects. (d) The left shows the recombined series of corrected reference and seafloor pressure observations including the offset between the two. An offset was determined, and since the true reference pressure value is known, the difference is used to calculate the absolute seafloor pressure.

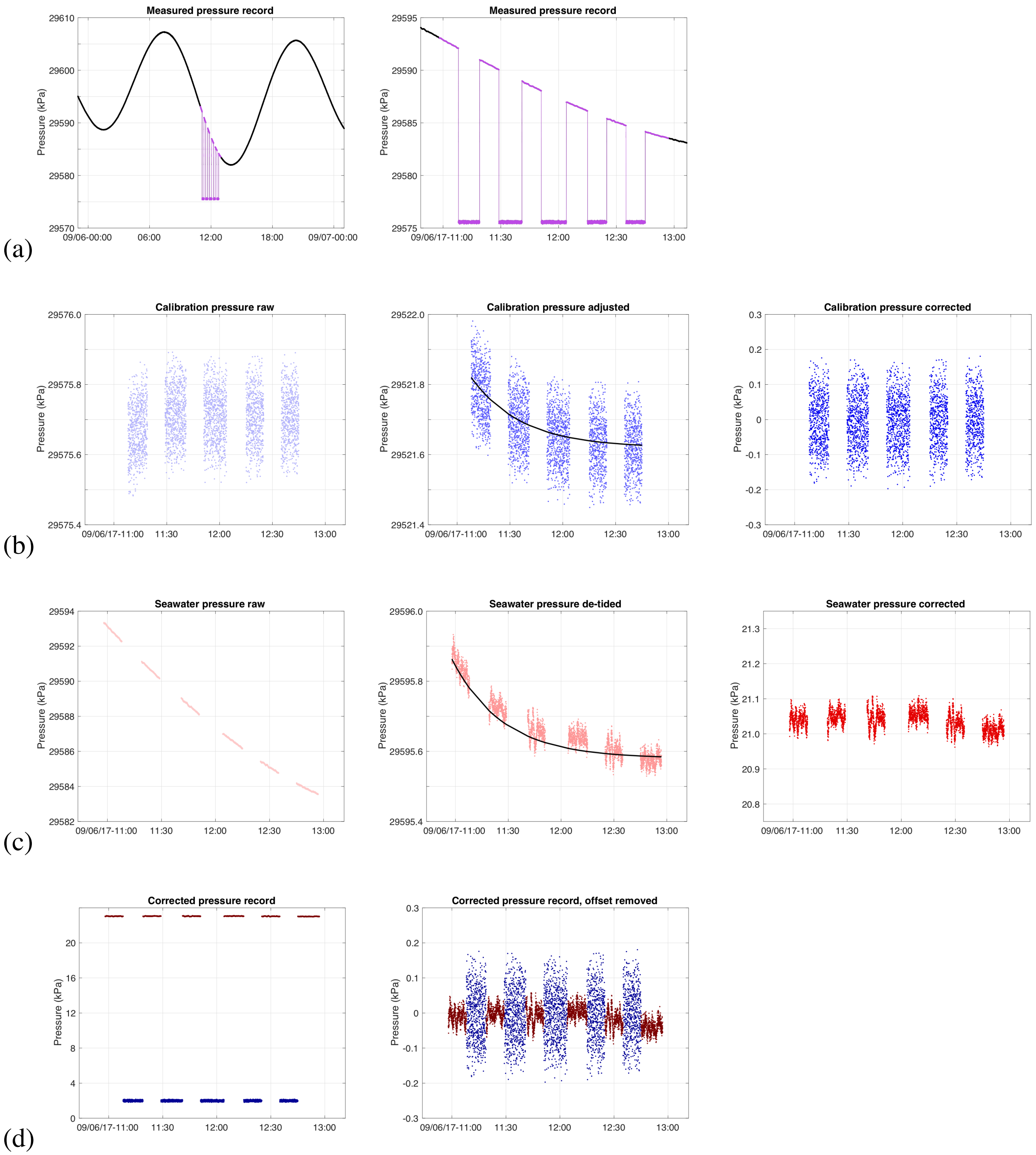
Measured pressure record
Pressure (kPa)
29610
29600
29590
29580
29570
09/06-00:00
06:00
12:00
18:00
09/07-00:00
(a)
Measured pressure record
29595
29590
29585
29580
29575
09/06/17-11:00
11:30
12:00
12:30
13:00
Calibration pressure raw
29576.0
29575.8
29575.6
29575.4
Calibration pressure adjusted
29522.0
29521.8
29521.6
29521.4
Calibration pressure corrected
0.3
0.2
0.1
0
-0.1
-0.2
-0.3
(b)
Seawater pressure raw
29594
29592
29590
29588
29586
29584
29582
Seawater pressure de-tided
29596.0
29595.8
29595.6
29595.4
Seawater pressure corrected
21.3
21.2
21.1
21.0
20.9
20.8
(c)
Corrected pressure record
20
16
12
8
4
0
Corrected pressure record, offset removed
(d)

5.2.3 Continuous Pressure Data

Noise driven by physical oceanographic processes can contribute several cm of noise at periods from hours to decades. These signals can eclipse tectonic signals of interest such as secular strain accumulation or slow slip events. When we infer the seafloor height from the absolute pressure surveys, we have aliased a number of oceanographic processes across a range of periods. In long time series spanning several decades, these signals are averaged out. Over shorter time periods, the absolute pressure surveys can be improved by including continuous pressure data to capture the oceanographic signals that are otherwise aliased. Individual surveys provide well-known values that can be used to calculate and remove the drift of continuous sensors, which can then be used to estimate deformation rates. A continuous BPR was deployed at or near each site to provide high-rate data between surveys. Different BPR instruments, all of which used Paroscientific quartz pressure sensors, were used to accommodate different depths, durations, and logistic needs. Figure 5.5 provides an overview of what BPR instrumentation was located at each station.

Two of the BPRs used were constructed at the SIO at UCSD. Each of these were deployed at O2 for non-overlapping 12-month periods. They used Paroscientific model 46K pressure sensors inside anodized aluminum and painted pressure cases. Data were integrated over 100-sec intervals and recorded to an internal memory card. The data were recovered from the internal memory after the instruments were physically recovered.

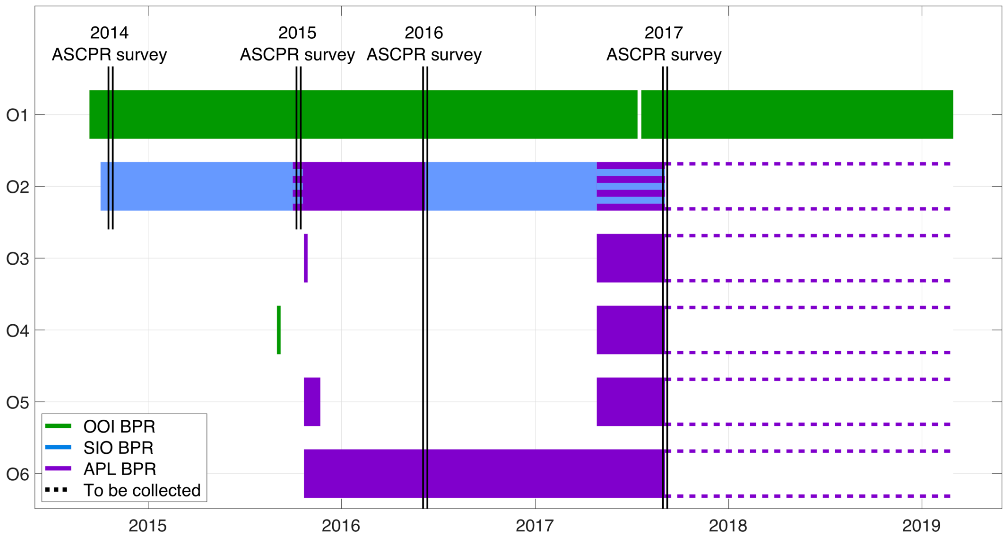

Figure 5.5 A timeline outlining the ASCPR surveys and continuous BPR data coverage at each station. The blue and purple stripes indicate when two BPRs overlapped in time.

Another five BPRs were built by the APL at UW. Two were designed for O5 and O6 in shallow water less than 100 m depth and used Paroscientific model 2200A pressure sensors inside PVC pressure cases. The other three were designed for greater depths ranging from 600 m to 1,900 m and used Paroscientific model 31K, 42K, and 43K pressure sensors housed inside titanium pressure cases. They all recorded at 15-sec intervals to internal memory. Data were recovered wirelessly using a radio frequency (RF) antenna to prevent disturbing the instruments when possible. In other instances, the data were recovered from internal memory after the instrument was recovered.

One other BPR from UW APL was installed on the OOI Cabled Array in September 2014. It housed a Paroscientific model 46K pressure sensor in a titanium housing. Data were recorded at 1-sec intervals and telemetered to shore in real-time at the OOI Data Portal.

5.2.4 Additional Geodetic Monumentation

The concrete benchmarks placed on the seafloor act as our primary measurement markers. In 2017, we installed secondary geodetic monuments as a way to monitor small height changes within the seafloor site. The additional monuments consisted of 4 m of aluminum pipes inserted 3 m deep into the seafloor sediment so that 1 meter extended above the seafloor, at O1, O3, and O4. The pipe is better coupled to the sediment at depth and provides a stable comparison monument within a few meters of the primary benchmark. The pipe was painted with alternating 15.0 cm long black and yellow stripes to increase visibility and provide a vertical length scale. A 15.3 cm by 40.3 cm metal plate with yellow-painted edges was fastened to the top of the pipe with a firehose coupling to support an MPR.

A total of four alternating, 5-minute long seafloor pressure measurements between the primary benchmark and secondary pole-mounted plate were made using the MPR. The pressure difference, a proxy for the relative height difference, was calculated after a computed tide model using SPOTL and a combined exponential-linear drift were removed (Agnew, 2012). The MPR measured height differences are listed in Table 5.2.

Table 5.2 Pressure differences (kPa) between primary benchmarks and secondary geodetic monuments measured by the MPR. The difference is taken as the pressure at the primary station minus the pressure measured at the secondary reference. Uncertainties are ±0.1 kPa for each.

Station	Secondary Reference	Pressure Difference (kPa)
O1	O1-pole	10.0
O2	O2B	-6.6
O2B	O2-APL benchmark	6.5
O3	O3-pole	12.6
O4	O4-pole	-2.9
O5	O5-APL benchmark	-20.5

5.3 Results

We present a table of true, absolute seafloor pressure values at the center of each benchmark, which form the basis for future decadal-scale absolute seafloor pressure measurements. These instrument-independent, fiducial measurements form the foundation for long-term surveys and studies of secular rates caused by tectonics and sea level rise. We also provide estimated secular deformation rates using surveys as individual points in long-term time series. Although each measurement has several cm of uncertainty, most of it is attributed to oceanographic processes whose effects will average out over long time spans of decades or more. Thus, the uncertainty of the estimated rates will improve with future measurements since it is inversely proportional to the span of the data. Secular rate estimates based on continuous BPR data corrected for sensor drift using the absolute pressure surveys as calibration points are also included for stations O1, O2, and O6. The BPRs at O3, O4, and O5 failed due to pressure housing leaks and we were unable to recover data for those sites. The cause was identified, and the instruments were modified and re-deployed. The continuous data availability is summarized in Figure 5.A.

Table 5.3 lists the absolute seafloor pressure value at the center of each benchmark averaged over the survey interval. The date, time, and duration of each survey are listed. Two pressure values are provided: (1) the seawater pressure including the ocean tides and (2) the seawater pressure with a computed SPOTL tide model removed (Agnew, 2012). The uncertainty of the pressure with tides included, σ_{PGC}, represents the quadrature sum of the 95% CI reference pressure uncertainty, which is described in Chapter 3 and summarized in Table 3.11, and statistical noise. The uncertainty of the pressure corrected for tides, σ_{total}, also incorporates the RMS of the tidal residuals at that location. The tide-corrected absolute pressure values and corresponding secular rate estimates are plotted for each station in Figure 5.6.

We leveraged the available continuous pressure data to provide better secular rate estimates. The individual surveys served as calibration values used to calculate and remove the drift from the continuous records, which contain information on non-tidal oceanographic signals at periods shorter than the interval between surveys (8 to 12 months). A linear least squares fit to the difference between the absolute survey data and continuous data was used to calculate the drift rate of the BPR, which was then removed from the continuous pressure record. The resulting drift-free pressure records were resampled to 30-minute intervals, de-tided using t_tide (Pawlowicz et al., 2012), and then lowpass filtered using a FIR filter with a passband at 1.2×10^{-6} Hz (0.10 cyc/day) and stopband at 7.7×10^{-6} Hz (0.067 cyc/day). Linear deformation rates were estimated from these records by linear least squares.

Stations O1 and O6 each had a single continuous BPR that spanned all of the surveys conducted. These records were calibrated as previously described. Stations O2 and O2B had three separate BPR deployments, each of which lasted between 8 and 15 months and overlapped with the previous BPR record by a few days. These three BPR records were combined into a single record by removing the first 90 days to remove any exponential drift component, detrended, and concatenated. Detrending each record removed long-term linear signals attributed to instrumental drift, but also removed secular tectonic and oceanographic signals. The real, physical secular tectonic and oceanographic signals were recovered by comparing the absolute pressure surveys with the combined pressure record. Stations O3, O4, and O5 are not included in this analysis since complete records were not available. The drift-free pressure records and estimated secular rates are plotted in Figure 5.7.

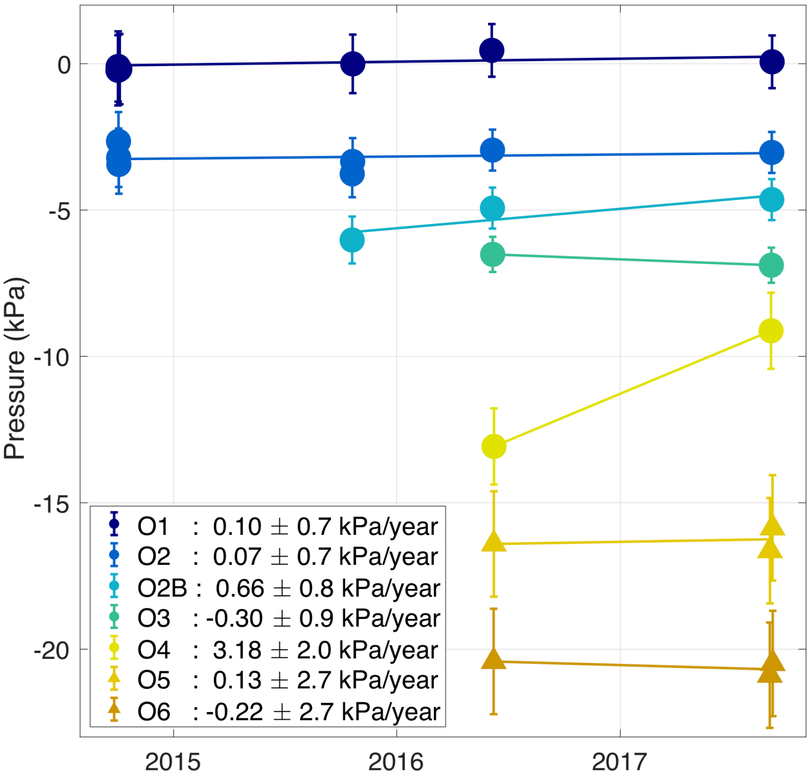

Figure 5.6 Pressure survey results from all of the stations. Estimated rates based on the surveys are listed. The plotted shapes indicate the benchmark form factor (standard or trawl-resistant).

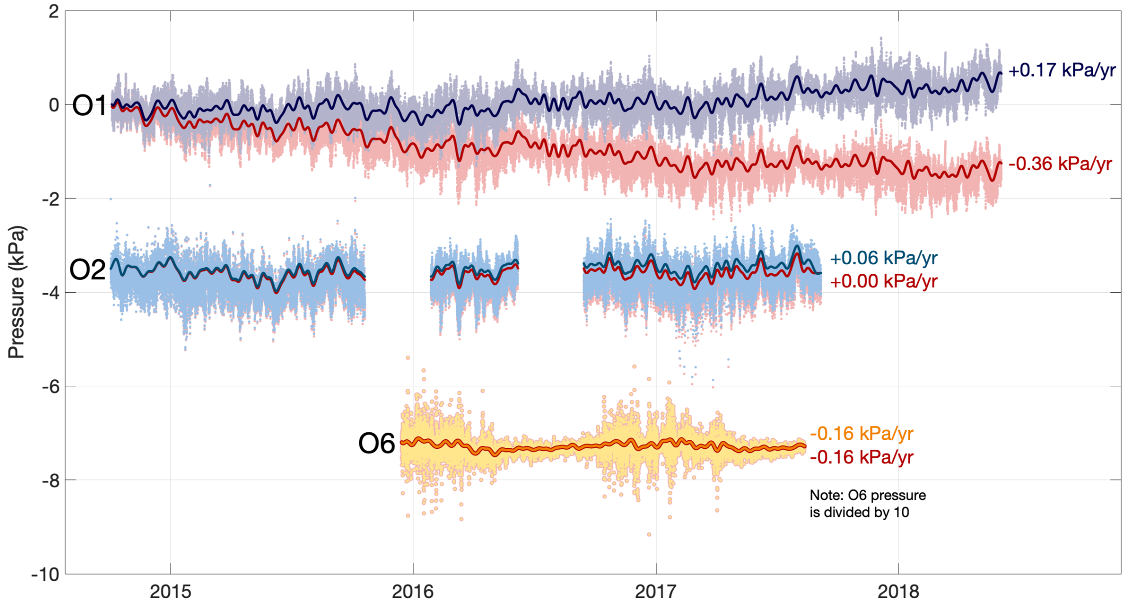

Figure 5.7 Continuous pressure records at three sites (O1, O2, and O6) that have been corrected for sensor drift using absolute pressure surveys as calibration values. The pressure record for site O6 has been scaled down by a factor of 10 and arbitrary offsets are plotted for clarity. Pressure records without any drift corrections are plotted in red and drift-corrected records are plotted in a different color.

Table 5.3. Absolute seafloor pressures averaged over the survey interval are reported with tides and with tides removed using a SPOTL tide model. The σ_{PGC} uncertainty represents the quadrature sum of the 95% CI reference pressure uncertainty and statistical noise, while σ_{total} also incorporates the RMS of the tidal residuals.

Date	Time (UTC)	Duration	Pressure with tides (kPa)	Pressure without tides (kPa)	σ_{PGC} (kPa)	σ_{total} (kPa)
Station O1						
2014-10-01	22:43	1:50	29,594.25	29,586.18	1.2	1.2
2014-10-02	06:15	1:50	29,576.03	29,586.31	1.2	1.2
2014-10-04	21:25	6:03	29,589.78	29,586.22	1.2	1.2
2015-10-21	05:05	2:03	29,578.67	29,586.40	1.0	1.0
2016-06-04	15:57	2:25	29,586.86	29,586.86	0.8	0.9
2017-09-06	10:58	1:58	29,578.66	29,586.47	0.8	0.9
Station O2						
2014-10-02	19:09	1:50	19,423.80	19,425.92	0.9	1.0
2014-10-03	01:21	1:56	19,433.47	19,425.36	0.9	1.0
2014-10-03	09:31	1:51	19,416.30	19,425.13	0.9	1.0
2015-10-20	23:56	1:50	19,431.58	19,425.23	0.7	0.8
2015-10-20	06:51	1:50	19,415.70	19,424.81	0.7	0.8
2016-06-05	21:44	1:46	19,429.81	19,425.62	0.6	0.7
2017-09-05	20:47	1:52	19,429.95	19,425.54	0.6	0.7
Station O2B						
2015-10-20	04:10	1:50	19,422.48	19,430.76	0.5	0.8
2016-06-05	19:11	2:21	19,440.66	19,431.85	0.5	0.7
2017-09-05	20:47	1:52	19,436.55	19,432.14	0.5	0.7
Station O3						
2016-06-06	05:05	2:14	13,407.22	13,396.35	0.3	0.6
2017-09-05	05:46	2:09	13,406.51	13,395.98	0.3	0.6
Station O4						
2016-06-08	08:05	1:47	6,395.33	6,383.03	0.3	1.3
2017-09-04	17:35	2:07	6,393.94	6,386.93	0.3	1.3
Station O5						
2016-06-08	01:58	1:58	887.71	891.48	0.3	1.8
2017-09-02	23:50	2:29	891.16	891.25	0.3	1.8
2017-09-07	02:33	2:39	889.18	892.03	0.3	1.8
Station O6						
2016-06-07	18:30	2:11	814.28	814.53	0.3	1.8
2017-09-02	15:55	1:45	818.12	814.06	0.3	1.8
2017-09-07	12:27	1:35	803.44	814.46	0.3	1.8

5.4 Conclusions

Absolute seafloor pressure measurements possess inherent value on their own as fiducial values. The ASCPR measurements can be used as longstanding benchmark values that can be incorporated into future geodetic studies. Each survey acts as a point in a long-term time series that could span decades or more and elucidate secular signals associated with tectonics or sea level rise. Additionally, the measurements' utility is improved if co-located with continuous BPR data, and they can be used to determine the long-term drift rate of the BPR. Continuous pressure data also provide high-rate information useful for reducing aliasing and estimating long-period (daily to annual) oceanographic signals.

The disagreement between rates estimated using only individual surveys and rates from calibrated continuous data is attributed to aliased signals driven by physical oceanography. Most tidal analysis methods can remove up to 98% of the tidal signal, which still leaves several cm of uncertainty in each survey. Second, any non-tidal effects from mesoscale eddies, currents, thermal fluctuations, or other causes are not addressed, which also contributes several cm of uncertainty in each survey. As such, over shorter time periods (e.g., a few years) or when expected deformation rates are small (e.g., cm/year), the preferred method includes the use of co-located BPRs. If significantly longer time periods (e.g. decades) are expected or if expected deformation rates are large (e.g., tens of cm/year), then single point pressure surveys can suffice on their own. In both cases, the estimated rate uncertainties will improve as the span of time between the first and last measurement increases.

These results demonstrate the capability of absolute seafloor pressure measurements for seafloor geodesy. Establishing additional time series of absolute measurements would be valuable for investigating other tectonic and oceanographic processes, such as global sea level rise. Our results do not yet allow us to clearly discern between different expected vertical deformation rates associated with different models or studies that incorporate additional geodetic data to produce stronger geophysical interpretations, but that is outside the scope of this paper. However, the results do establish baseline vertical geodetic measurements in Cascadia and that, when compared to similar measurements in the future, will be able to establish secular vertical deformation rates.

5.5 Acknowledgements

Chapter 5, in full, is currently being prepared for submission for publication as **Cook, M. J., G. S. Sasagawa, D. A. Schmidt, E. C. Roland, W. S. D. Wilcock, and M. A. Zumberge, Absolute Calibrated Seafloor Pressure Measurements for Geodesy in Cascadia, *in preparation***. The dissertation author is the primary investigator and author of this material.

We thank Michael Kirk, David Price, and Heinz Wuhrmann for engineering assistance. We would like to thank Dana Manalang, Ken Davis, Deb Kelley, and the rest of the OOI cohort at the UW for technical assistance, guidance, and continued maintenance of the SCPR on the OOI Cabled Array.

We acknowledge the crews and teams of the R/V Roger Revelle, R/V Thomas G. Thompson, R/V Sikuliaq, ROV ROPOS, and ROV Jason. Funding was provided by the National Science Foundation under award OCE-1558468 and gift funds from the University of Washington.

Chapter 6

Incorporation of Additional Modeling

6.1 Poly3D

I used the 3D polygonal, boundary element code *Poly3D* to compute a range of models that estimated expected vertical deformation signals in various regions of interest in Cascadia. These models were used for illustrative purposes within the scope of the ASCPR pressure project. *Poly3D* solves for stress and displacement changes in an elastic half-space given stresses or displacements on a fault surface (Thomas, 1993).

The plate interface is represented as a three-dimensional dislocation surface based on the plate geometry of McCrory et al. (2012) and was produced by Professor David Schmidt at the University of Washington. A number of studies believe that the range of reasonable expected lower locking limits falls between 20 to 35 km depth (Li et al., 2018; McCrory et al., 2012; Schmalzle et al., 2014). I used a value of 20 km for the lower locking limit transitioning to slipping at 25 km depth. The depth of the upper edge of the locked zone determines the width of the locked zone. I varied the depth of the upper edge and transition zone to create different locked zone scenarios. Figure 6.1 is an illustration of a subduction zone and the parameters described. Other factors such as the lower locking limit depth and along-strike variations also influence the expected deformation but have a negligible effect on the deformation along a single profile and were not investigated.

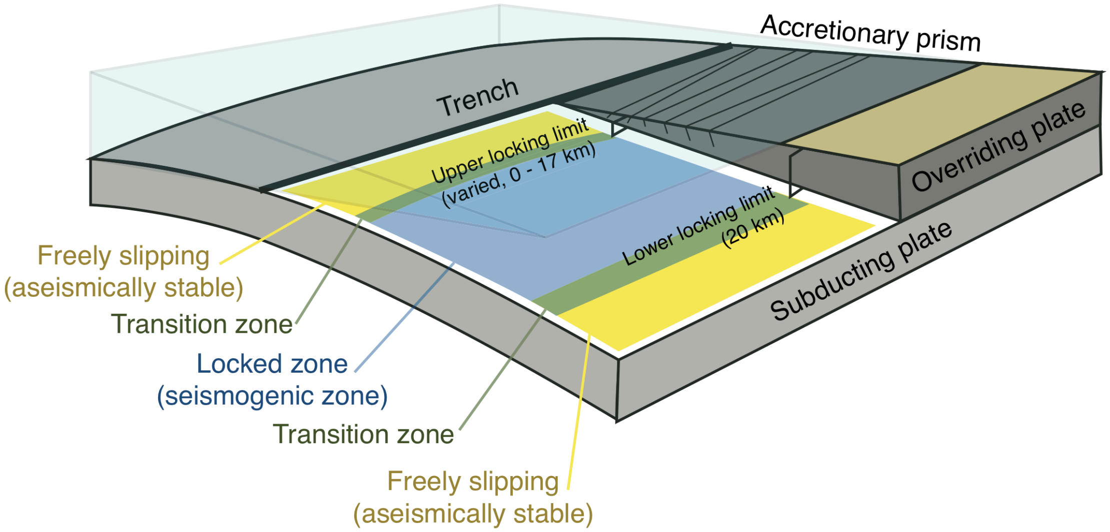

Figure 6.1 An illustration of a subduction zone. Locked areas of the plate interface are shown in blue, and transition (green) to freely slipping regions (yellow). The lower locking limit was set at a depth of 20 km and transitioned to slipping at 25 km depth. The upper limit was varied between 17 km depth to 0 km depth (locked at the surface, or to the trench).

Professor David Schmidt generously shared MATLAB scripts that call *Poly3D* using the Cascadia subduction zone plate geometry. I modified his MATLAB scripts to predict uplift for three locking scenarios along the Cascadia subduction zone.

6.1.1 Locking Models and Expected Deformation Rates

Three primary models of interest were investigated that represent a range of possible locking distributions from a narrow locked zone to full locking to the trench. The expected vertical deformation distribution was generated for each of the cases, as well as a plot of the locking and deformation along our ASCPR benchmark profile. In all three models, the lower limit of the locked zone transitions from locked at 20 km depth to freely slipping at 25 km depth and the upper limit of the locked zone was varied to control the width of the locked zone. We infer locking from the backslip rate, or the slip deficit along the fault interface. In central Cascadia, the plate convergence rate is approximately 4 cm/year. Therefore, a backslip rate of 4 cm/year means that the plates are locked and backslip of 0 cm/year means that the plates are freely slipping.

The first model examines the case of a narrow locked zone. Figure 6.2 shows a map of the locking, map of the expected vertical deformation rate, and the backslip and vertical rates along our profile at 44.5 °N. The plate interface is locked from a depth of 20 km depth up to 17 km. Then, it transitions to freely sliding at 10 km depth and above. This model produces a strong subsidence of nearly 1 cm/year about 50 km off the coast and a moderate uplift of about 0.5 cm/year at the coast.

The second model illustrates a medium locked zone. Figure 6.3 includes a map of the locking, map of the expected vertical rate, and the backslip and vertical rates for our profile. The plate interface is locked between 20 km and 12 km depths. It transitions to freely slipping at 4 km and above. This model also produces strong subsidence of nearly 1 cm/year about 70 km from the coast and uplift of about 0.7 cm/year along the coast.

The final model represents a fully locked subduction zone. Figure 6.4 shows maps of the locking and expected vertical rate, and plots along our profile. The plate interface is locked from 20 km up to the trench, or 0 km depth. In this scenario, small subsidence rates less than 0.5 cm/year extend offshore from the coast. A moderate uplift rate of about 0.7 m/year along the coast is expected.

Figure 6.5 shows the backslip and vertical deformation rates for each of the three modeled scenarios along our profile in a single plot for comparison.

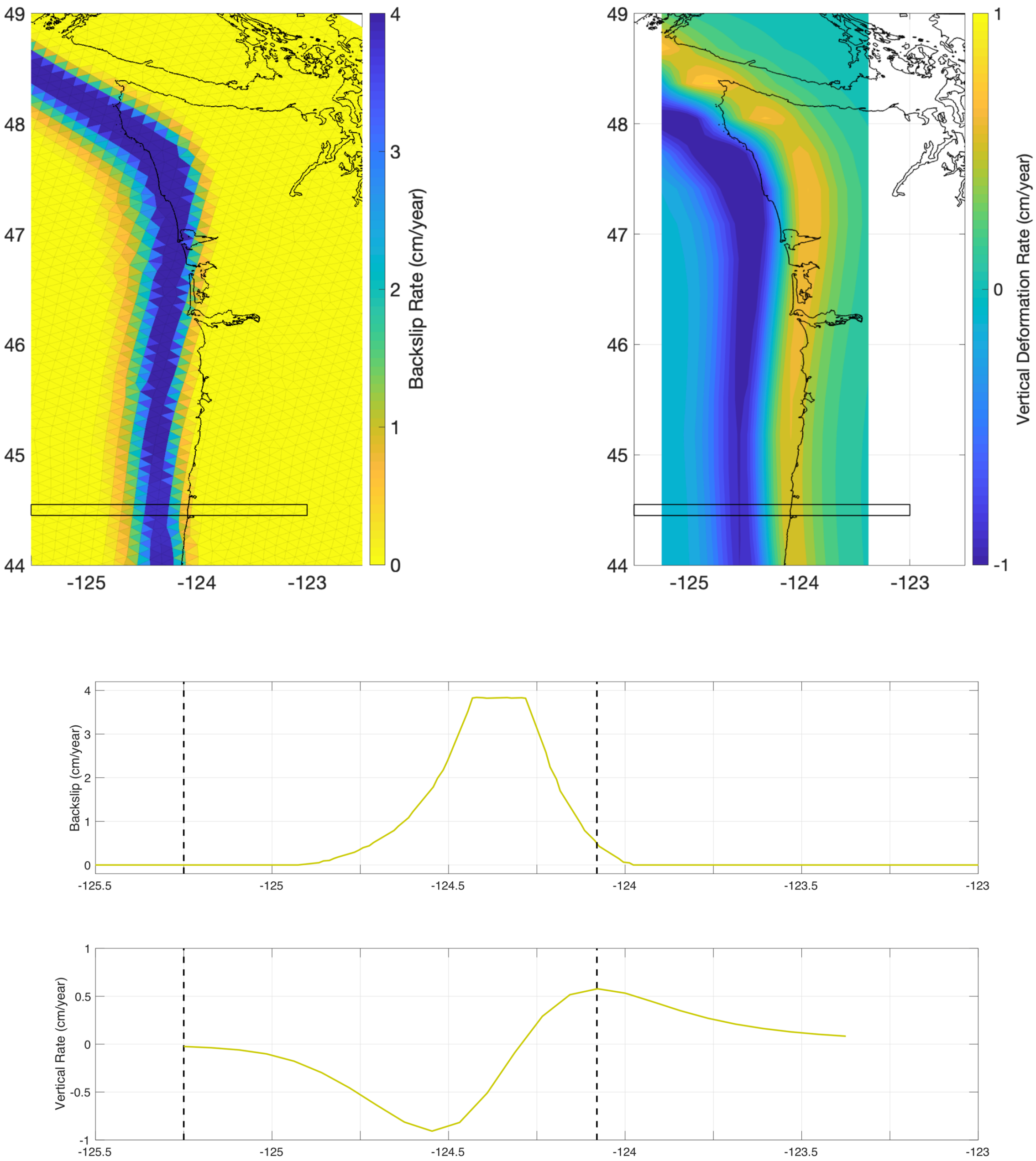

Figure 6.2 A model for a narrow locked zone scenario. The left map plots the backslip rate, the middle map plots the vertical deformation rate, and the two graphs below plot the backslip and vertical deformation for the profile along 44.5 °N.

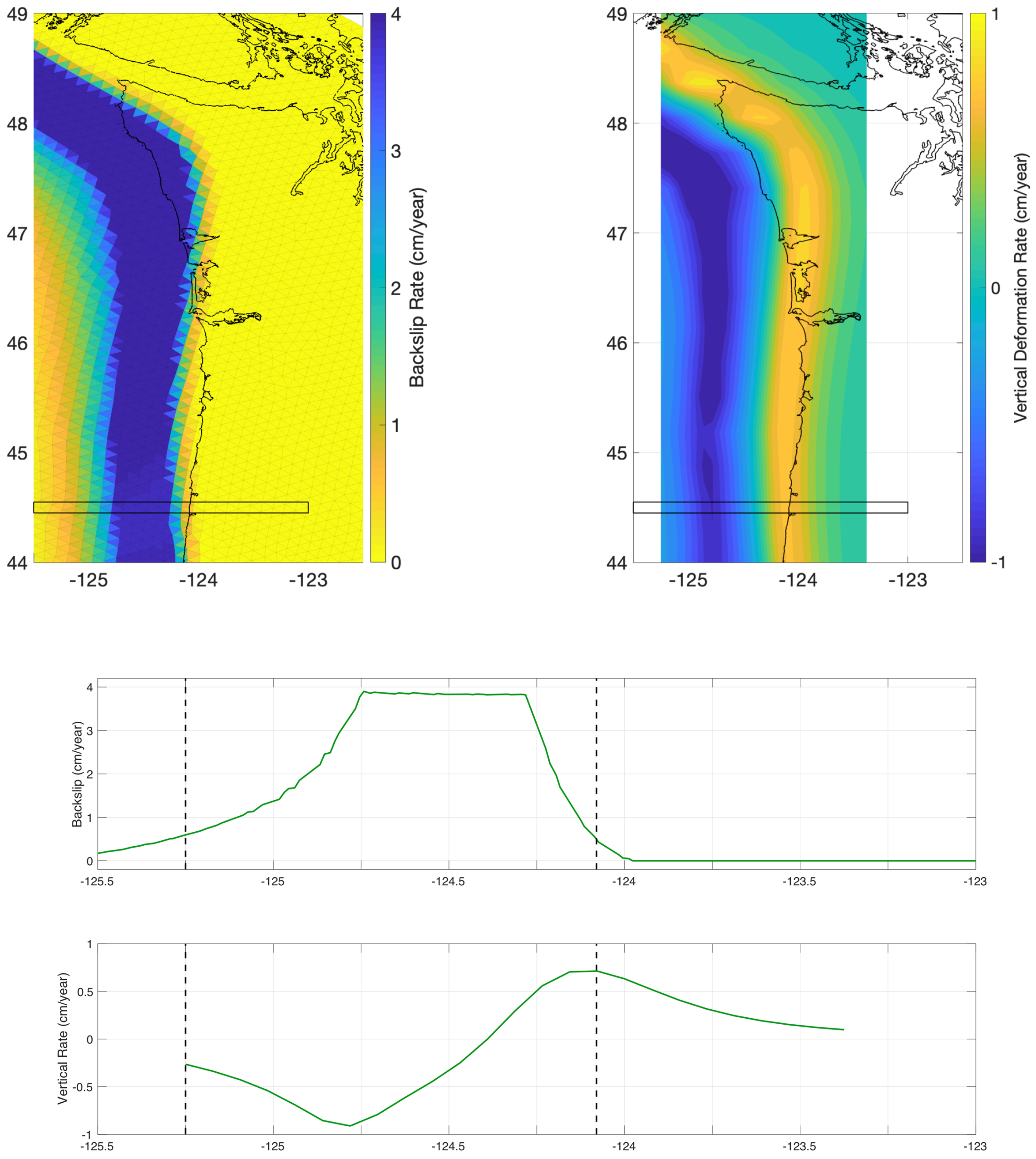

Figure 6.3 A model for a medium locked zone scenario. The left map plots the backslip rate, the middle map plots the vertical deformation rate, and the two graphs below plot the backslip and vertical deformation for the profile along 44.5 °N.

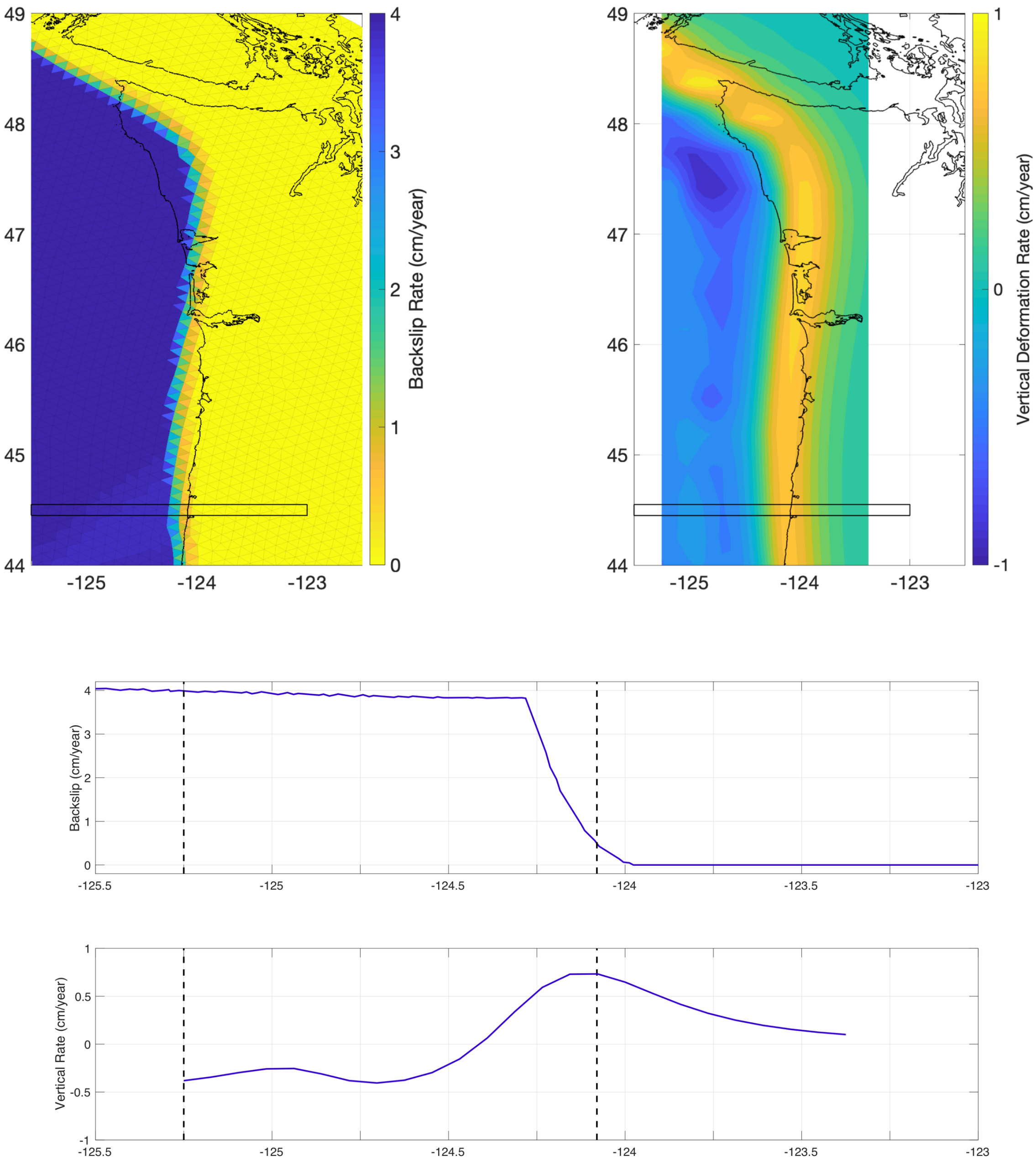

Figure 6.4 A model for a fully locked zone (to the trench) scenario. The left map plots the backslip rate, the middle map plots the vertical deformation rate, and the two graphs on the right plot the backslip and vertical deformation for the profile along 44.5 °N.

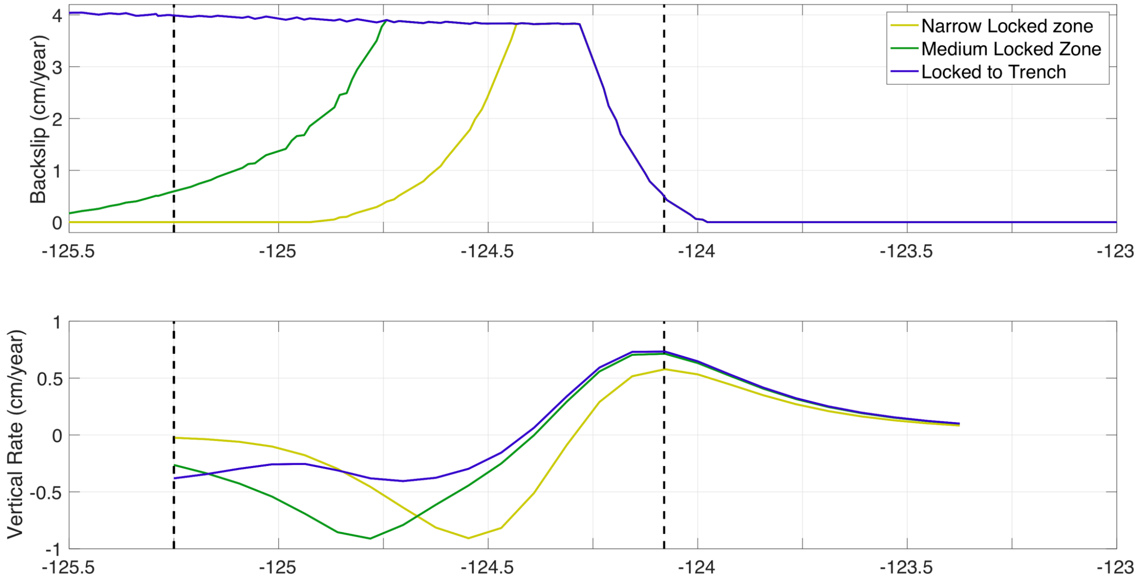

Figure 6.5 The plot in the top shows the backslip rate (locking) along our profile for the three cases of a narrow locked zone (yellow), medium locked zone (green), and locked to the trench (blue). The lower plot corresponds to the expected vertical deformation rates for each of the scenarios. The dashed black lines represent the trench and the coastline.

6.1.2 Conclusions

The models generated are useful for illustrative comparisons with our ASCPR data but are not comprehensive. Variations in the along-strike locking distribution, the lower locking limit, and incorporation of slow slip and tremor would provide more insights into the full range of expected outcomes and have been investigated in the context of the Cascadia subduction zone (e.g., Frankel et al., 2018; Wirth et al., 2018). These results provide a baseline of deformation that we may expect to detect in long-term marine geodetic measurements and can help guide the deployment or permanent installation of seafloor instruments. The modeled scenarios (Figure 6.5) highlight the need for more and greater accuracy offshore measurements: along the coast and on land (landward of -124 °E), the deformation rates converge to the same value, but offshore, the predicted rates can vary between subsidence and uplift by a few mm/year. High-accuracy and long-term geodetic measurements can provide improved constraints and be used to discriminate between different models.

6.2 Structure-from-Motion Photogrammetry

Photogrammetry is a technique that uses overlapping sequences of photographs to invert for a three-dimensional spatial model of the region within the photo survey area. This technique and its extension structure-from-motion (SfM), which simultaneously inverts for camera positions and generates 3D spatial data and a 3D model, are widely used on land and in the air and are capable of cm-level precision over areas up to tens of meters. These surveys can be performed over relatively short periods of time, i.e., hours (Westoby et al., 2012). This method has made its way into the marine setting by way of scuba, ROV-, and AUV-based surveys, primarily in the context of mapping. However, its use in the marine environment is still relatively nascent and so far, has been limited to archaeological, biological, and relatively coarse mapping (Bennecke et al., 2016; Burns et al., 2015; Drap et al., 2015; Kwasnitschka et al., 2012; Westoby et al., 2012). Photogrammetry surveys with similar levels of precision and durations would provide a great utility to and reduce the costs of surveying and monitoring geodetic benchmarks, instruments, and field sites. In conjunction with other geodetic methods in the marine environment, it also has the potential to improve large-scale mapping, imaging, and navigation (Escartin et al., 2008; Kwasnitschka et al., 2016).

The number of marine geophysical and geodetic measurements has grown considerably in the last decade and continues to increase. Some methods, such as the GPS-Acoustic and ASCPR methods, can be more cost- and time-efficient by replacing and relocating sensors or performing campaign-style surveys to capture long-term time series (Chadwell and Spiess, 2008; Fujita et al., 2006; Gagnon and Chadwell, 2007). These methods require benchmarks installed on the seafloor for accurate re-positioning. Other methods could benefit from the installation of more permanent geodetic monuments that serve as fiducial markers and references for other studies.

One component of uncertainty in benchmark surveys depends on the stability of the benchmark. Errors are propagated into the measurements if a benchmark is disturbed from its initial position, either due to settling in sediment or an external perturbation. Some studies have observed little to no changes in benchmark placement and orientation of a cm or less over many years (Chadwick et al., 2006; Fujimoto et al., 2011; Stenvold et al., 2006), while others have seen larger disturbances due to the collapse of substrate or being pushed by ROV (Chadwick et al., 2006). Although changes in benchmark position on the order of several mm/year may not be significant in regions with considerable deformation rates of tens of cm/year such as volcanoes or resource reservoirs (Chadwick et al., 2006; Stenvold et al., 2006), the same is not true in subduction zones or other regions where secular rates are on the order of a few cm/year or less (Burgette et al., 2009; Savage, 1995). Studies that span decades in regions with small secular rates will require careful assessments of benchmark stability since its contribution could be a considerable amount of the expected rate. The SfM photogrammetry method, when conducted in repeated surveys spanning several years or more could provide useful constraints on the stability of benchmarks and relative changes within the photo surveyed site.

6.2.1 Survey Design

Our survey site was located at the O2 site along the ASCPR profile on the continental margin of Oregon. It included two geodetic monuments with known length scales installed on a sedimented seafloor a few meters apart (Figure 6.6). The primary monument was the circular concrete benchmark used for ASCPR pressure surveys. It measures 76.2 cm in diameter, 15.2 cm thick, and weighs 319 lb. in air or 147 lb. in water. It includes two visual markers - an orange ring around the outside edge and three black radial lines at 120° spacing - to improve instrument placement and orientation consistency. The second monument consisted of a total of 4 m of aluminum pipe inserted 3 m deep into the seafloor sediment so that 1 meter extended above the seafloor. The first 2 m-long pipe had a nozzle at the bottom tip that expelled water pumped through the top of the pipe as it was pushed into the sediment. The second 2 m-long pipe was connected by a fire hose coupling to the first section and the pair was pushed down an additional 1 m. The pipe is coupled to the sediment at depth, which provides a stable, useful reference that is resilient to erosion, deposition, and perturbations at the seafloor surface, analogous to GPS monuments anchored at depth. It was painted with alternating 15.0 cm-long black and yellow stripes to increase visibility and provide a vertical length scale that was easily resolvable in images at distances up to a few meters. A 15.3 cm x 40.3 cm metal plate with yellow-painted edges was fastened to the top of the pipe with a firehose coupling to accommodate the MPR. Yellow was chosen as the primary color since it is bright and does not attenuate as strongly as red-hued colors; black was chosen since it offers high contrast to both yellow and the bare aluminum.

6.2.2 Photogrammetry and Pressure Survey Methods

We used Agisoft Photoscan Pro software to produce a 3D model of the site that includes known control points, height scales, and length scales, which were compared to known dimensions. As a further check, each monument was designed to accommodate a pressure sensor. The pressure difference between the two monuments provided a precise measure of the height difference to within 1.1 cm, which served as a second, high accuracy validation of the photogrammetry results.

Many software suites that perform photogrammetry and SfM processing are freely or commercially available. We used Agisoft Photoscan Pro (v1.2.3.2331), which uses a pixel-matching inversion to generate 3D spatial data and models. The software can establish a relative coordinate system without any ancillary information about the position and orientation of the photos. An absolute coordinate frame can be established with the addition of location and orientation data from GPS-enabled or inertial systems. Alternatively, user-defined ground control points (GCPs) defined by known parameters within the survey area are required to generate an absolute coordinate frame. The GCPs also provide crucial information for creating model scale. Model uncertainty is inferred from the RMS misfit of the model to the GCPs based on pixel error and pixel size.

The photo survey was performed with the ROV Jason. A series of 115 12-megapixel digital images were collected with a Sony HD camcorder, which was the standard digital still image camera on Jason, as the ROV circled the test site at different altitudes of 2 to 3 m and distances of 2 to 4 m. The camera had an intervalometer function set to capture 1 image every 5 seconds for the duration of the 10-minute survey. The camera's pan, tilt, and zoom were set such that most of the ROV body and manipulators were outside of the photograph frame. The pan and tilt were not changed during the photo survey, although this would be allowed since Agisoft Photoscan Pro does not necessarily require consistent orientation or orientation information. The zoom was fixed to prevent different amounts of geometric lens distortion, which would have required additional processing. The photos were processed with Adobe Photoshop CS6 for sharpness and contrast to improve image quality for the software processing. A generic Sony camera wide-angle lens correction was used to mitigate the geometric distortion, the frames were cropped to remove the ROV body from the image, and the contrast was adjusted to improve image sharpness and clarity.

The ROV disturbed the sediment on the seafloor during the photogrammetry survey, which led to many suspended particles being captured in the photographs. We set the pixel-matching inversion to an intermediate setting that allowed misfit greater than the minimum possible to produce smoother meshes more representative of the seafloor and benchmarks rather than the suspended particles. We used the diameter of the concrete benchmark to establish a horizontal scale and the width of the painted stripes on the pipe to establish a vertical scale. The concrete benchmark tilt was measured with the MPR and a second pressure recorder equipped with a tilt sensor and the pole tilt was measured with the MPR and a second, independent tilt sensor. The tilt measurements provided constraints for solving for the real coordinate system orientation.

Pressure measurements can be used to measure vertical height changes or relative height differences because a 0.1 kPa pressure change is easily and reliably measured and corresponds to a 1 cm seawater or seafloor height change. The measured pressure difference between the two platforms was used to determine the height difference between the two points. The pressure surveys were conducted over a couple hours, so the inherent pressure sensor drift was negligible. We used an MPR with two redundant Paroscientific pressure sensors and an internal tilt sensor to record the pressure and the extrinsic tilt of the two platforms.

The MPR was placed on the reference pole plate and the concrete seafloor benchmark in an alternating order. The two monuments were occupied three times each for 10-minute intervals. The instrument's lateral placement and orientation were kept constant to within a cm and 0.1° respectively.

6.2.3 Results

Agisoft Photoscan Pro produced the 3D spatial model shown in Figure 6.6 alongside a photograph from the same perspective. The model space coordinate frame was generated using GCPs defined by the face of the benchmark and without any camera position and orientation information, which was not collected by the ROV. Since the GCPs were defined such that the benchmark face was assumed to be a horizontal plane, so the *z*-axis was aligned with the vector normal to the benchmark face. The benchmark was slightly tilted in the seafloor, so the modeled space differed from the true, physical space in an amount of the benchmark tilt. The tilt of the modeled reference frame biased the height difference by a small amount and required a rotation to correctly determine the height difference. We used in situ tilt measurements to rotate the model to a true vertical system that was aligned with the gravity vector and recover the height difference.

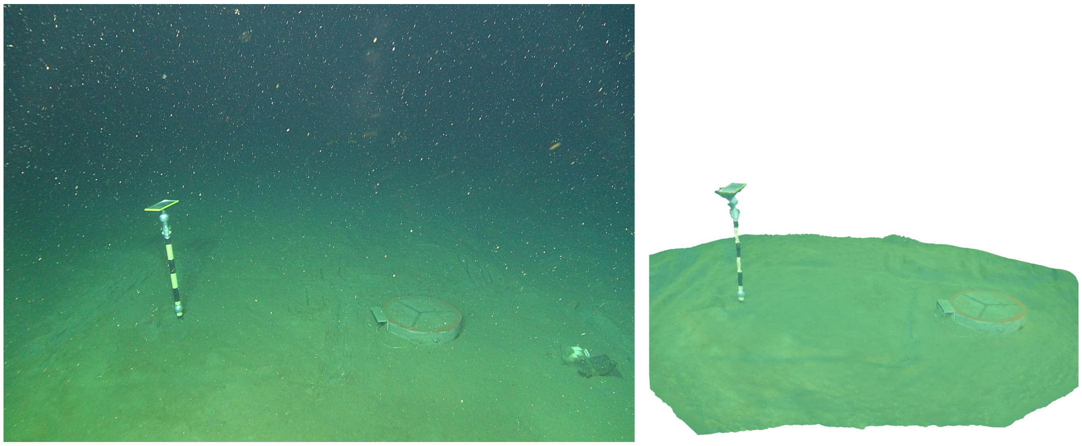

Figure 6.6 The left is a photograph of the seafloor site with the reference pole and ASCPR benchmark. The right is the 3D spatial model of the site from the same perspective.

Figure 6.7 is a schematic drawing of the seafloor site, with the relevant geometry and values to calculate the height difference between the benchmark and plate. Coordinates and angular measurements in the true, physical space coordinate frame are denoted by a non-prime system by

Z, L, θ, and ϕ. Values in the modeled, benchmark-normal space coordinate frame are denoted by a prime system by Z', L', a', and θ'. Since we only need to rotate along the line-of-sight (LOS) between the benchmark and the pole and not the entire system (Figure 6.7), we can use a simplified geometric correction described by a series of equations to calculate the height difference in the true vertical reference frame, Z.

$$B = L' tan(\theta_{\mathrm{LOS}}) \tag{6.1}$$

$$A = Z' - B \tag{6.2}$$

$$Z = Acos(\theta_{\mathrm{LOS}}) \tag{6.3}$$

$$Z = \left[Z' - L' tan(\theta_{\mathrm{LOS}})\right] cos(\theta_{\mathrm{LOS}}) \tag{6.4}$$

The correction only required the tilt, or dip angle, of the benchmark in the LOS direction between the two monuments, θ_{LOS}. The tilt of the pole, ϕ, is not needed because the height of the point at the top of the pole is independent of its angle. The azimuths of the benchmark tilt, α_{bench}, and pole tilt, α_{pole}, were not measured in situ, so we solved for them using a system of equations:

$$sin(\theta)\, cos(\alpha_{\mathrm{bench}h}) \ - \ sin(\phi)\, cos\left(\alpha_{\mathrm{pole}}\right) = sin\left(\theta'\right) \tag{6.5}$$

$$\alpha'_{\mathrm{bench}} + \alpha'_{\mathrm{pole}} = \Delta\alpha \tag{6.6}$$

Equation 6.5 imposed the condition that the difference between the LOS-projection of the measured tilts matched the modeled difference and equation 6.6 required that the difference of the true azimuths matched the modeled value. The LOS benchmark tilt was calculated to be 2.2 ± 0.8°.

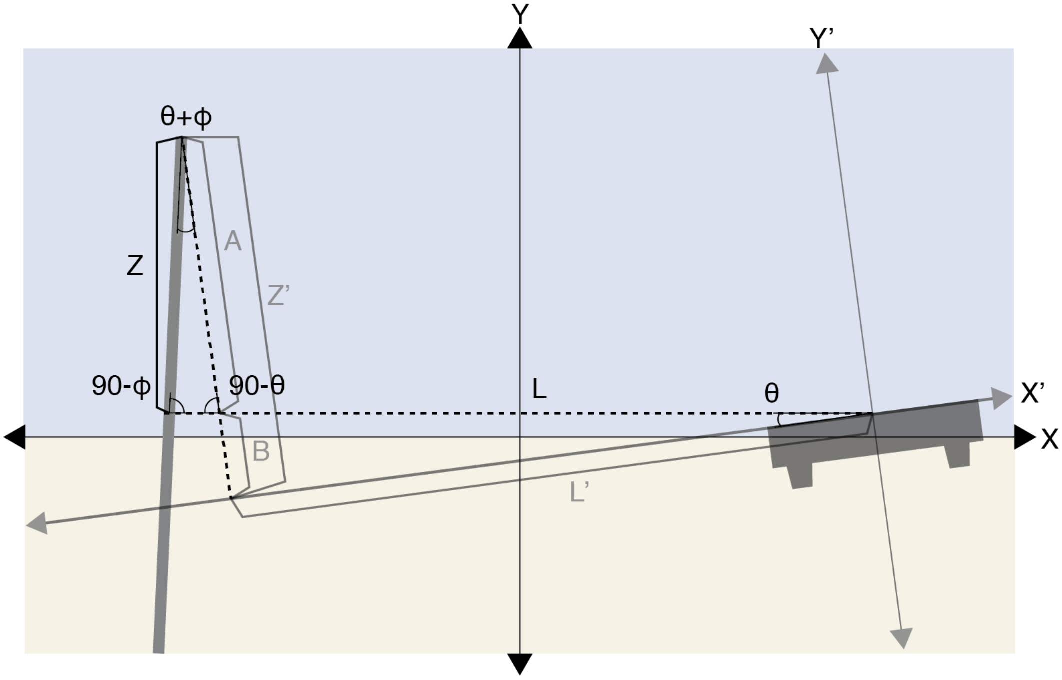

Figure 6.7 A schematic drawing of the projection of the model coordinate frame onto a true, gravity-normal coordinate frame. Variables denoted with a prime (e.g., L' and Z') are measurements made in the modeled space. Non-prime variables represent the true, physical space coordinate frame.

The software calculated a distance between the benchmark and pole, *L'*, of 243.0 ± 2.3 cm and a height difference, *Z'*, of 111.7 ± 2.3 cm. These uncertainties represent the 95% CI of the misfit. After applying the geometric correction to *Z'*, the true height difference between the benchmark and pole, *Z*, was determined to be 102.2 ± 6.0 cm.

The MPR data were first corrected for ocean tides using a computed tide model generated by SPOTL software, and then with linear least squares to minimize the difference between the measured pressures on the plate and benchmark (Agnew, 2012). The best-fit pressure difference was 9.97 ± 0.11 kPa, which is equivalent to a height difference of 99.7 ± 1.1 cm. The uncertainty represents a 95% CI.

6.2.4 Conclusions

The results show that commercially available photogrammetry software can produce a good 3D model of a seafloor site based on a relatively limited photo survey with a consumer-grade camera. The pressure survey height difference of 99.7 ± 1.1 cm falls within the range of the photogrammetry modeled height difference of 102.2 ± 6.0 cm, so the photogrammetry survey is accurate within its uncertainty range.

We completed one photogrammetry survey to establish an initial model of the site. Multiple photogrammetry surveys would allow us to measure relative changes within the site over time. Changes to the benchmarks, camera, and survey designs should improve accuracy and model results. In this work, some areas of the model were incomplete and over-modeled due to the inherent challenge of resolving thin, long, and complex structures as opposed to large, broad structures. Additional limitations included color inaccuracy and limited visibility range, an insufficient number of low, high, far, and near viewpoints, and few visual targets for the software to register. These considerations could be accommodated by using different high contrast paints (e.g., orange instead of yellow) and employing more known references, markers, or coded targets, which can be generated by the software. Given consistent camera resolution, density of control points, and camera distance from the scene, we would expect comparable uncertainties over larger survey areas of tens of meters at the cost of ROV time and computing resources.

Several survey-based geodetic methods require stable benchmarks to reliably measure secular crustal motion and deformation. Pressure surveys can be useful for assessing the vertical benchmark motion and settling but they can be time consuming. We believe that photogrammetric SfM surveys could be used as a cost-effective method to monitor benchmark stability over areas of several meters. Separating the signals attributed to benchmark movements and perturbations from tectonic signals would improve the fidelity of repeat pressure or GPS-Acoustic surveys and could allow measurements made at a disturbed benchmark to be corrected and tied to measurements made at the originally undisturbed benchmark. At the current level of accuracy, it is limited to regions of significant expected ground motion or disturbance, such as areas that may be trawled, or to regions where the rate of motion may be small but could accumulate over longer periods of time such as several years. On their own, repeated photogrammetry surveys can detect relative changes within the photo scene. However, they can also provide more complete spatial coverage than individual measurements and are complementary to other mapping methods being used and developed to capture changes in geodetic monuments and benchmarks, geologic outcrops, slope failures, hydrothermal vents, seafloor instruments and cables, and so on. The absolute pressure or GPS-Acoustic measurements could also be used to tie a photogrammetry survey to an absolute reference frame or multiple photogrammetry surveys together. Our results confirm the viability of the method without the use of special cameras or other equipment for studies of marine geologic, biological, and archaeological processes. Including the use of orientation or inertial navigation sensors, higher resolution cameras, and coded targets could improve results, making them sufficient for monitoring geodetic instrumented sites over periods of a few years.

While photogrammetry can routinely be done with high levels of accuracy on land, it is significantly more challenging in water. We found that incorporating standard consumer-grade cameras and simple survey designs can achieve several cm-level results that have applications and utility in the context of geophysical and geodetic research. However, we also recognize that the development and investment of specialized or dedicated equipment, such as LIDAR, can be done to achieve better cm-scale results.

6.3 Characterizing Oceanographic Noise for Geodetic Studies

Noise driven by physical oceanographic processes is a persistent problem in offshore datasets. It can easily mask geodetic signals due to tectonic changes such as secular strain accumulation or slow slip, or climate-driven changes such as sea level rise. Several processes are at work, from currents and eddies to El Niño Southern Oscillation and longer, decadal events. These contribute several centimeters of noise at periods ranging from hours to decades.

Simple methods such as examining differences between stations in an array or lowpass filtering are able to reduce these contributions, but they indiscriminately reduce or remove all signals, including possible tectonic signals of interest (Wallace et al., 2016; Frederickson et al., 2018). Other techniques to characterize oceanographic variability using satellite-based methods have been suggested and preliminarily investigated by a number of researchers (Ballu et al., 2011; Hughes et al., 2018; Piecuch et al., 2015). These either use or assimilate satellite sea surface height (SSH) measurements, gravity measurements, and other data types to characterize non-tectonic signals. Additionally, global ocean models have greatly improved in the recent years and are approaching temporal and spatial resolutions that will be useful for assessing local and regional variability. Both of these have potential for improving our ability to reliably detect and characterize tectonic deformation of the seafloor.

6.3.1 Global Ocean Models

Global scale ocean models, such as ECCO (Estimation of the Circulation and Climate of the Ocean) and HYCOM (Hybrid Coordinate Ocean Model), exist and provide either cumulative or vertically layered data that can be converted into an ocean bottom pressure (OBP) equivalent. They provide temporal resolution on the order of 1 day and hind- and forecasts are nominally available between 2004 and present. Most models provide spatial resolution on the order of 10 km with global coverage. The benefit of these is that they typically assimilate SSH, wind forcing, fresh water input, or a combination of measurements.

The Gravity Recovery and Climate Experiment (GRACE) project has also provided insights into mass distributions around the world, including over the oceans. Mass concentration solutions are used to determine the total quantity and distribution of mass in the oceans and also produce an OBP data product (Watkins et al., 2015). However, GRACE OBP data are more spatially and temporally limited than SSH and global models. Daily values are interpolated but the spacing between points is ~300 km and single locations should not be used to evaluate local signals. The data can provide constraints on basin-scale processes, which likely influence pressure variability on timescales of several weeks and longer.

I used the ECCO global model version 4 release 3 to investigate the long-period variability in seafloor pressure (Fukumori et al., 2017). The ECCO OBP product is an interpolated and re-gridded version of the GRACE OBP product, so only very large-scale pressure anomalies and corresponding timescales of weeks or more should be recovered. A seafloor pressure record near our pressure survey station O1 was used to evaluate the ECCO OBP product in reducing oceanographic noise. The seafloor pressure was de-tided and then the ECCO OBP was removed. Figure 6.8 shows the time series of the ECCO products used (OBP and SSH) and Figure 6.9 shows the pressure results using those products as corrections. Figure 6.10 shows the power spectra of the records. The ECCO OBP reduced the variance at periods between 2 to 10 days but increased the variance at periods of 30 days and longer.

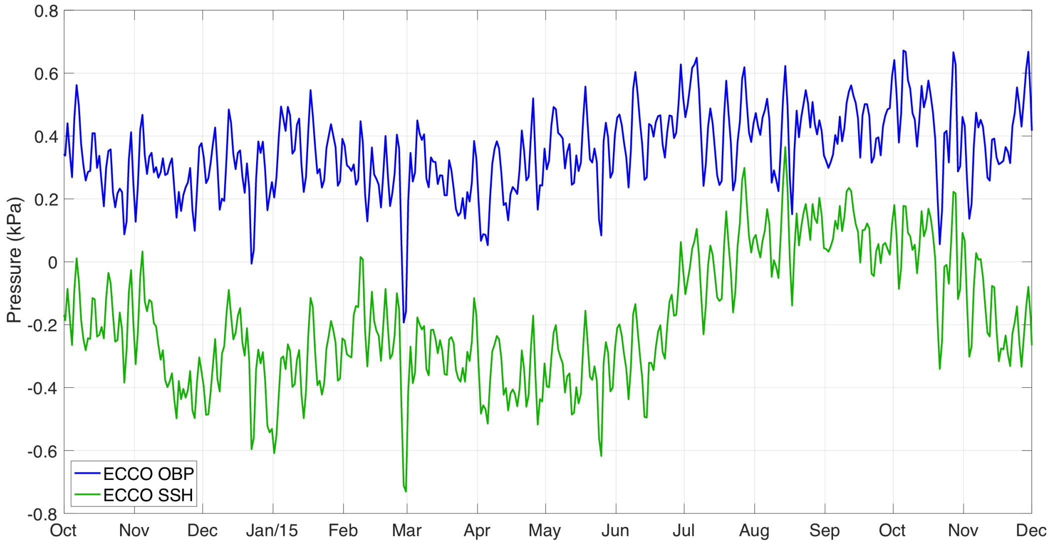

Figure 6.8 The ECCO OBP and SSH time series for the period coinciding with continuous pressure data near station O1. The OBP is plotted in blue and the SSH is plotted in green.

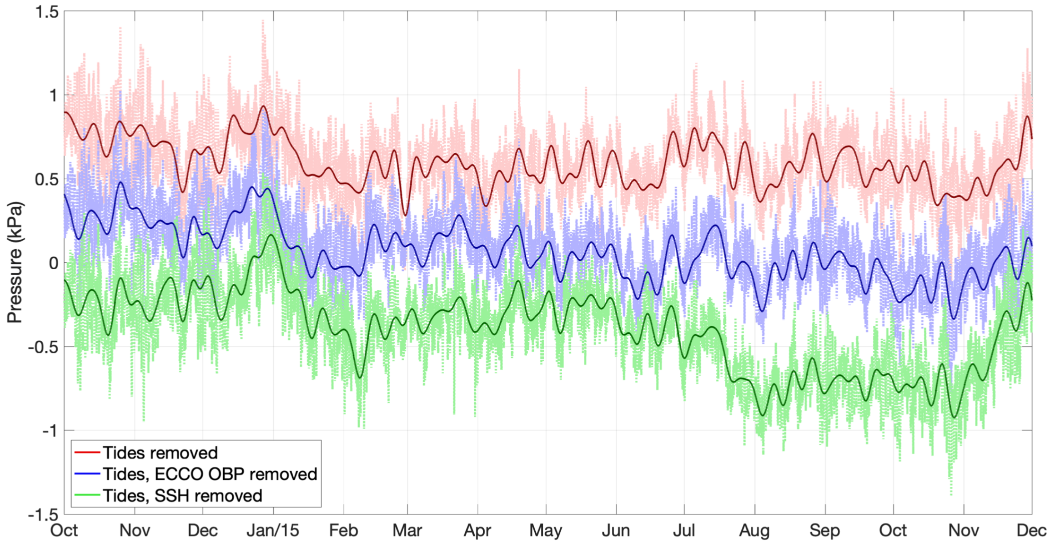

Figure 6.9 A plot of the seafloor pressure record near station O1. The de-tided pressure is plotted in red; the de-tided pressure with the ECCO OBP removed is plotted in blue; and the de-tided pressure with the satellite SSH removed is plotted in green. Lowpass-filtered records are plotted on top in dark red, blue, and green respectively.

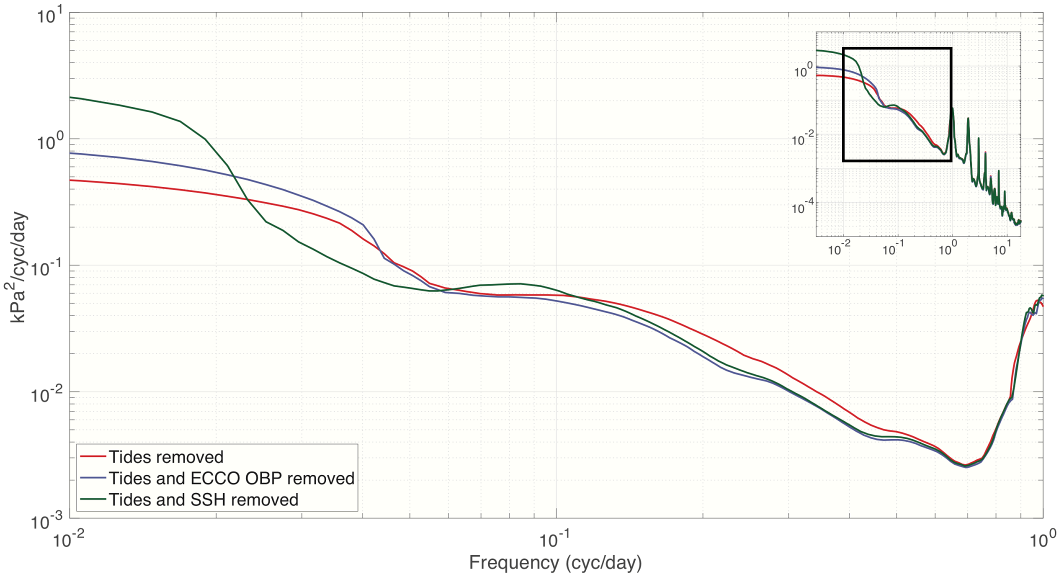

Figure 6.10 Power spectra for the pressure records with various tide, OBP, and SSH corrections. The plot shows frequencies up to 1 cycle per day, which is the sampling rate of the ECCO OBP and the SSH product.

6.3.2 Satellite Data

Satellite data, notably SSH altimetry measurements, are considered to have strong potential to extract oceanographic signals from OBP and other datasets and recover tectonic signals. Satellites run tracks around the globe in ascending and descending orbits with relatively limited spatial resolution – approximately 150 – 300 km between adjacent tracks varying with latitude. Measurements are also temporally limited, with repeated tracks occurring every 10 to 14 days. These factors make aliasing a challenge; however, the globally gridded and interpolated data can still provide useful constraints and variance reduction of ocean variability at longer periods of 20 days or more (Gille and Hughes, 2001). Since satellite altimetry SSH measurements are made from orbit, the data require solid Earth, steric, and height-to-pressure corrections. Earth tides and steric components, which are not captured in OBP records, are typically provided or can be extracted separately. A number of other products are available, including mean dynamic topography and steric corrections, which would be used to identify and separate barotropic and baroclinic effects.

I also used the ECCO SSH product, which includes the mean dynamic sea level and a steric correction for this comparison. The ECCO SSH product interpolates and grids altimetry data from multiple satellites. The same de-tided seafloor pressure record was used as the initial time series and then the SSH product was converted to pressure and removed. The resulting time series and power spectrum are shown in Figure 6.8 and Figure 6.9. The SSH product provided better variance reduction between about 3 to 10 days and 20 to 60 days. However, it did contribute a considerable additional signal at longer periods.

6.3.3 Conclusions

Remote sensing and global models have the potential to help reduce oceanographic noise in many marine geophysical and geodetic measurements. Presently, using either of these methods would require much more investigation as to how to handle and process the data. I found that neither the ECCO OBP nor SSH provided a clear solution to reduction of noise in a year-long seafloor pressure record. Cross-spectral analyses showed that the magnitude squared coherences between pressure and OBP and pressure and SSH were very weak and inconsistent at nearly all periods below 30 days.

Neither of the products were able to address persistent signals with a period of about 14 days that is observed in the seafloor pressure. It is unlikely that this signal is caused by imperfect tidal corrections or a beating frequency due to the magnitude of the signal, the fact that tidal constituents are very well-known, and its persistence when using different tidal corrections. However, the OBP and SSH data were able to effectively capture a single, notable transient. In late December 2015, a week-long, 10 cm pressure change was observed by the BPR. It was also well-captured by both the ECCO OBP and SSH, and thus shows no distinct signal in Figure 6.8.

While it is clear that the ECCO OBP is not the ideal data product for this study, the HYCOM could provide a better solution. It is more detailed and assimilates more data than the ECCO OBP. The HYCOM model was outside the scope of this project but could be useful in the future. In addition, the SSH product used could be improved on. AVISO (Archiving, Validation and Interpretation of Satellite Oceanographic Data) provides a greater number of products, which could be interpreted separately. Additionally, individual tracks or track crossing points close to the regions of interest could be identified and those specific datasets could be evaluated.

6.4 Acknowledgements

Chapter 6, in part, is currently in revision for publication in Earth and Space Science as: **Cook, M. J., and J. B. DeSanto (2019), Validation of geodetic seafloor benchmark stability using structure-from-motion and seafloor pressure data, *Earth and Space Science*, *in revision*.** The dissertation author is the primary investigator and author of this material.

We thank Mark Zumberge and Glenn Sasagawa for scientific support, technical assistance, and mentoring throughout the project. We acknowledge the crews of the R/V Roger Revelle and the R/V Sally Ride, and the ROV Jason team for their assistance and encouragement. We would also like to acknowledge Bruce Appelgate for additional ship time through the UC Ship Funds program to conduct tests offshore La Jolla, CA. Ship time was supported by the National Science Foundation under award OCE-1558468.

I would like to thank David Schmidt for providing the *Poly3D* code and extensive assistance and guidance in producing useful models. I would also like to thank Donna Blackman and the Paul G. Silver Young Researcher Enhancement Award committee for providing generous support to travel to meet and work with David Schmidt.

Chapter 7

Conclusions

7.1 Summary of the Dissertation

In this dissertation I addressed the state of ocean bottom pressure instrumentation in the context of marine geodesy. We have successfully demonstrated the SCPR drift correction method at Axial Seamount and established the ASCPR absolute pressure survey method in the Cascadia subduction zone. We were able to make some of the first measurements of the vertical seafloor deformation uncontaminated by pressure sensor drift. I also have investigated new and complementary method to improve the fidelity and integrity of marine geodetic measurements.

Axial Seamount is an active area of research due to its ongoing activity. In 2013, we deployed an SCPR in the southwestern area of the caldera. We were able to characterize and correct the sensor drift of two independent sensors to recover a drift-free vertical deformation estimate. Over a 17-month period from September 2013 to November 2014, we measured 60 cm of uplift, corresponding to an average uplift rate of 42.4 cm/year. After that demonstration, the SCPR was successfully funded to be connected to the OOI Cabled Array at Axial Seamount to provide continuous, real-time seafloor pressure data. We identified key issues encountered in the previous deployment, notably the galvanic corrosion and electronic controller, and modified the instrument to make it suitable for a longer deployment on the seafloor. The SCPR was connected to the OOI Cabled Array in July 2018 and has been recording data continuously and in real-time since then. We have conducted over a dozen calibrations over the last 9 months to characterize and remove the drift of the two pressure sensors. Our drift-corrected pressure time series reveal an average uplift rate of about 44.0 cm/year. The SCPR will continue to provide real-time, continuous data and will serve as a useful long-term geodetic comparison for other drift correction methods being used and developed.

We also used the SCPR in a different capacity to make absolute pressure measurements in campaign-style surveys in the Cascadia subduction zone. Between 2014 and 2017, we to conducted absolute pressure surveys with the ASCPR at seven seafloor benchmarks along a trench-perpendicular profile off the coast of central Oregon. In this context, we required a greater attention to the details, metrology, and accuracy of the instrument to make true, instrument-independent, absolute seafloor pressure measurements. We performed a number of calibrations and tests of the various measurement parameters to determine and verify their values. We established the first absolute reference pressure values and used them both to calibrate co-located pressure sensors and as individual points in long-term time series. We corrected the drift in three of our co-located continuous pressure records, and then estimated secular vertical deformation rates from the continuous records. We found that the individual points did not provide reliable estimates of the secular deformation due to the short amount of time our surveys span. Signals driven by physical oceanography contribute a considerable amount of noise that was aliased over the four-year period, which limited our ability to infer a secular rate based on our four surveys. However, many of the oceanographic signals will be averaged out over the span of decades and a longer time series would allow a reliable estimate of the secular rate to be made.

Finally, I investigated a number of avenues to improve the fidelity of geodetic measurements and monitor the integrity of geodetic monumentation on the seafloor. Models of Cascadia were produced to provide illustrative comparisons for measurements and guide future considerations. We installed a new geodetic seafloor monument, which provides a more stable reference because it is coupled to the sediment at depth. We validated structure-from-motion photogrammetry as a method to measure distances and length scales underwater that has applications to monitoring the stability of benchmarks or monuments within the local site. Oceanographic noise is a prevalent issue in pressure data, especially for detecting slow slip events or secular deformation. I investigated the viability of global ocean models

7.2 Future Directions

Since marine geodesy is a nascent field, there are many avenues to pursue towards the development of new methods and tools and the improvement of existing ones. Further investigations into pressure sensor behaviors would provide valuable insights into future instruments. Continued pressure measurements would provide better constraints on geophysical systems and encourage comparisons of drift correction methods. Finally, calibrated pressure measurements and other methods can be used to better characterize oceanographic noise or tie complementary measurements together.

The root cause of pressure sensor drift is not well-known. While physical mechanisms such as outgassing, loading, and aging, have been proposed, they have not been definitively verified or quantified. Investigations into the physical mechanisms behind drift would provide valuable insights as to how to measure and mitigate drift. Additionally, there is an often-overlooked temperature rate dependence in pressure sensors when large temperature changes are encountered (Boss and González, 1995; Chiswell, 1991). This effect was avoided for our studies because we chilled pressure sensors to a temperature close to the seafloor temperature. However, this would still be a valuable avenue to investigate for other methods and studies.

While we are presently acquiring data from the SCPR installed on the OOI Cabled Array, continued and different types of geodetic measurements will provide very valuable insights into the efficacy of various drift correction methods. Our results from two studies in different areas of Axial Seamount both showed significantly higher deformation rates than the current MPR survey paradigm. Future MPR surveys will likely incorporate our co-located SCPR measurements as a comparison against the standard reference MPR station, which is assumed to be stable. Furthermore, the addition of an A0A instrument co-located with the SCPR in the caldera center will provide another reference for comparison and validation of all of the methods.

We made initial measurements in the Cascadia subduction zone that will serve as instrument-independent fiducial values far into the future. The accumulation of tectonic deformation increases, and the estimated uncertainties improve, as the time span between measurements grows, so future measurements will be valuable for secular estimates of deformation. The absolute pressure measurements made throughout this dissertation will contribute to a legacy of measurements in the area and can be referenced in future studies of the area. We also plan to establish additional profiles in Cascadia. The ASCPR and absolute pressure survey method also provides a great utility for intermittently calibrating co-located pressure sensors connected to permanent infrastructure.

Finally, as more marine measurements are collected, the ways the data are processed and analyzed will improve. One of the preeminent issues with marine geophysical data is the presence of environmental noise. A considerable amount of it is driven by physical oceanographic processes, which are often left unaddressed or handled in a non-deterministic way, such as through filtering. However, many – not all – of these processes are studied, modeled, and understood by physical oceanographers whose expertise will become important and valuable. Global ocean models continue to incorporate more types and amounts of data and continue to offer better spatial and temporal resolutions. As geophysical and geodetic measurements move into new domains, interdisciplinary collaborations will become increasingly important and valuable to identifying and separating various signals. Marine geodetic measurements could see an evolution similar to terrestrial GPS, which was once limited by noise in the atmosphere and ionosphere to meter-scale accuracies. Today, GPS is capable of mm-level accuracies and has broad applications to not only tectonic motions, but also hydrologic, atmospheric, and ionospheric studies.

References

Agnew, D. C. (2012), SPOTL: Some Programs for Ocean-Tide Loading, *SIO Technical Report*, UC San Diego: Scripps Institution of Oceanography, https://escholarship.org/uc/item/954322pg.

Arnulf, A. F., A. J. Harding, G. M. Kent, S. M. Carbotte, J. P. Canales, and M. R. Nedimović (2014), Anatomy of an active submarine volcano, *Geology*, 42(8), 655-658, https://doi.org/10.1130/G35629.1.

Arnulf, A. F., A. J. Harding, G. M. Kent, and W. S. D. Wilcock (2018), Structure, Seismicity, and Accretionary Processes at the Hot Spot-Influenced Axial Seamount on the Juan de Fuca Ridge, *J. of Geophys. Res.: Solid Earth*, 123(6), 4618-4646, https://doi.org/10.1029/2017JB015131.

Atwater, B. F., A. R. Nelson, J. J. Clague, G. A. Carver, D. K. Yamaguchi, P. T. Bobrowsky, J. Bourgeois, M. E. Darienzo, W. C. Grant, E. Hemphill-Haley, H. M. Kelsey, G. C. Jacoby, S. P. Nishenko, S. P. Palmer, C. D. Peterson, and M. A. Reinhart (1995), Summary of Coastal Geologic Evidence for Past Great Earthquakes at the Cascadia Subduction Zone, *Earthquake Spectra*, 11(1), 1-18, https://doi.org/10.1193/1.1585800.

Ballu, V., P. Bonnefond, S. Calmant, M.-N. Bouin, B. Pelletier, O. Laurain, W.C. Crawford, C. Baillard, and O. de Viron (2012), Using altimetry and seafloor pressure data to estimate vertical deformation offshore: Vanuatu case study, *Adv. Space Res.*, 51 (8), 1335-1351, https://doi.org/10.1016/j.asr.2012.06.009.

Bean, V. E. (1994), NIST Pressure Calibration Service, *U. S. Department of Commerce, CODEN: NSPUE2*, U. S. Government Printing Office, Washington, D. C., USA, *Nat. Inst. Stand. Technol. Spec. Publ.*, 250-39.

Bennecke, S., T. Kwasnitschka, A. Metaxas, and W.-C. Dullo (2016), In situ growth rates of deep-water octocorals determined from 3D photogrammetric reconstructions, *Coral Reefs*, 35(4), 1227-1239, https://doi.org/10.1007/s00338-016-1471-7.

Blum, J. A., S. L. Nooner, and M. A, Zumberge 2008), Recording Earth strain with optical fibers. *IEEE Sensors Journal*, 8(7), 1152-1160, https://doi.org/10.1109/JSEN.2008.926882.

Boss, E. F., and F. I. González (1995), Corrections to bottom pressure records for dynamic temperature response, *J. of Atmos. and Ocean. Tech.*, 12(4), 915-922, https://doi.org/10.1175/1520-0426(1995)012%3C0915:CTBPRF%3E2.0.CO;2.

Burgette, R. J., R. J. Weldon II, and D. A. Schmidt (2009), Interseismic uplift rates for western Oregon and along-strike variation in locking on the Cascadia subduction zone, *J. Geophys. Res.*, 114, B01408, https://doi.org/10.1029/2008JB005679.

Burgmann, R., and D. Chadwell (2014), Seafloor Geodesy, *Annual Review of Earth and Planetary Sciences*, 42(1), 509-534, https://doi.org/10.1146/annurev-earth-060313-054953.

Burns, J. H. R., D. Delparte, R. D. Gates, and M. Takabayashi (2015), Integrating structure-from-motion photogrammetry with geospatial software as a novel technique for quantifying 3D ecological characteristics of coral reefs, *PeerJ*, 3, https://doi.org/10.7717/peerj.1077.

Caplan-Auerbach, J., R. P. Dziak, J. Haxel, D. R. Bohnenstiehl, and C. Garcia (2017), Explosive processes during the 2015 eruption of Axial Seamount, as recorded by seafloor hydrophones, *Geochem. Geophys. Geosyst.*, 18, 1761–1774, https://doi.org/10.1002/2016GC006734.

Caress, D. W., D. A. Clague, J. B. Paduan, J. F. Martin, B. M. Dreyer, W. W. Chadwick Jr, A. Denny, and D. S. Kelley (2012), Repeat bathymetric surveys at 1-metre resolution of lava flows erupted at Axial Seamount in April 2011, *Nat. Geosci.*, 5(7), 483, https://doi.org/10.1038/ngeo1496.

Chadwell, C. D., and F. N. Spiess (2008), Plate motion at the ridge-transform boundary of the south Cleft segment of the Juan de Fuca Ridge from GPS-Acoustic data, *J. Geophys. Res.*, 113, B04415, https://doi:10.1029/2007JB004936.

Chadwell, C. D. (2016), Initiation of GPS-Acoustics Measurements on the Continental Slope of the Cascadia Subduction Zone, Abstract T31C-2907 presented at the 2016 AGU Fall Meeting, San Francisco, CA, 12-16 Dec.

Chadwick Jr, W. W., S. L. Nooner, M. A. Zumberge, R. W. Embley, and C. G. Fox (2006), Vertical deformation monitoring at Axial Seamount since its 1998 eruption using deep-sea pressure sensors, *J. of Volc. and Geotherm. Res.,* 150(1-3), 313-327, https://doi.org/10.1016/j.jvolgeores.2005.07.006.

Chadwick Jr, W. W., S. L. Nooner, D. A. Butterfield, and M. D. Lilley (2012), Seafloor deformation and forecasts of the April 2011 eruption at Axial Seamount, *Nat. Geosci.*, 5(7), 474, https://doi.org/10.1038/ngeo1464.

Chiswell, S. M. (1991), Dynamic response of CTD pressure sensors to temperature, *J. of Atmos. and Ocean. Tech.*, 8(5), 659-668, https://doi.org/10.1175/1520-0426(1991)008%3C0659:DROCPS%3E2.0.CO;2.

Cook, M. J. (2015), Characterizing Thermal Expansion of the Piston Gauge in the Absolute Self-Calibrating Pressure Recorder, University of California San Diego, La Jolla, CA, https://escholarship.org/uc/item/0hm620n8.

Drap, P., D. Merad, B. Hijazi, L. Gaoula, M. M. Nawaf, M. Saccone, B. Chemisky, J. Seinturier, J.-C. Sourisseau, T. Gambin, and F. Castro (2015), Underwater Photogrammetry and Object Modeling: A Case Study of Xlendi Wreck in Malta, *Sensors*, 15, 30351-30384, https://doi:10.3390/s151229802.

Escartín, J., R. García, O. Delaunoy, J. Ferrer, N. Gracias, A. Elibol, X. Cufi, L. Neumann, D.J. Fornari, S.E. Humphris, and J. Renard (2008), Globally aligned photomosaic of the Lucky Strike hydrothermal vent field (Mid-Atlantic Ridge, 37°18.5′N): Release of georeferenced data, mosaic construction, and viewing software, *Geochem. Geophys. Geosyst.*, 9(Q12009), https://doi.org/10.1029/2008GC002204.

Frankel, A. D., E. A. Wirth, N. Marafi, J. E. Vidale, and W. J. Stephenson (2018), Broadband synthetic seismograms for magnitude 9 earthquakes on the Cascadia megathrust based on 3D simulations and stochastic synthetics, Part 1: Methodology and overall results, *Bull. of the Seis. Soc. of Am.*, 108(5A), 2347-2369, https://doi.org/10.1785/0120180034.

Frederickson, E. K., Wilcock, W. S. D., P. MacCready, E. C. Roland, D. A. Schmidt, M. A. Zumberge, G. S. Sasagawa, and A. L. Kurapov (2018), The Detectability of Offshore Slow Slip Earthquakes with Seafloor Pressure Sensors: A Sensitivity Analysis for the Cascadia Subduction Zone, Abstract T44C-06 presented at 2018 AGU Fall Meeting, Washington, DC, 10-14 Dec.

Fujimoto, H., M. Kido, Y. Osada, K. Tadokoro, T. Okuda, Y. Matsumoto, and K. Kurihara (2011), Long-Term Stability of Acoustic Benchmarks Deployed on Thick Sediment for GPS/Acoustic Seafloor Positioning, *Modern Approaches Solid Earth Sci.*, 8, 263-272, https://doi.org/10.1007/978-90-481-8885-7_13.

Fujita, M., T. Ishikawa, M. Mochizuki, M. Sato, S.-I. Toyama, M. Katayama, K. Kawai, Y. Matsumoto, T. Yabuki, A. Asada, and O.L. Colombo (2006), GPS/Acoustic seafloor geodetic observation: method of data analysis and its application, *Earth Planets Space*, 58, 265-275, https://doi.org/10.1186/BF03351923.

Fukumori, I., O. Wang, I. Fenty, G. Forget, P. Heimbach, and R. M. Ponte (2017), ECCO version 4 release 3.

Gagnon, K. L., and C. D. Chadwell, Relocation of a seafloor transponder—Sustaining the GPS-Acoustic technique, *Earth Planets Space*, 59, 327-336, https://doi.org/10.1186/BF03352692.

Gille, S. T. and C. W. Hughes (2001), Aliasing of high-frequency variability by altimetry: Evaluation from bottom pressure recorders, *Geophys. Res. Lett.,* 28(9), 1755-1758, https://doi.org/10.1029/2000GL012244.

Goldfinger, C., C. H. Nelson, A. Morey, J. E. Johnson, J. Patton, E. Karabanov, J. Gutiérrez-Pastor, A. T. Eriksson, E. Gràcia, G. Dunhill, R. J. Enkin, A. Dallimore, and T. Vallier (2012), Turbidite Event History: Methods and Implications for Holocene Paleoseismicity of the Cascadia Subduction Zone, US Geological Survey Professional Paper 1661-F, Reston, Virginia, US Geological Survey, https://pubs.usgs.gov/pp/pp1661f/.

Goldfinger, C., C. H. Nelson, J. E. Johnson, and S. S. Party (2003), Holocene earthquake records from the Cascadia subduction zone and northern San Andreas fault based on precise dating of offshore turbidites, *Ann. Rev. of Earth and Planet. Sci.*, 31(1), 555-577.

Götze, H. J. (2011), International gravity formula, *Encyclopedia of Solid Earth Geophysics*, 611-612, https://doi.org/10.1007/978-90-481-8702-7_102.

Hill, D. P. (2006), Unrest in Long Valley Caldera, California, 1978–2004, *Spec. Publ. Geol. Soc.*, 269, 1-24, https://doi.org/10.1144/GSL.SP.2006.269.01.02.

Hughes, C. W., J. Williams, A. Blaker, A. Coward, and V. Stepanov (2018), A window on the deep ocean: The special value of ocean bottom pressure for monitoring the large-scale, deep-ocean circulation, *Progress in Oceanography*, 161, 19-46, https://doi.org/10.1016/j.pocean.2018.01.011.

Jain, K., W. Bowers, and J. W. Schmidt (2003), A primary dead-weight tester for pressures (0.05–1.0) MPa, *J. of res. of the Nat. Inst. of Stand. and Tech.*, 108(2), 135, https://dx.doi.org/10.6028%2Fjres.108.013.

Kwasnitschka, T., H. Hansteen, C. W. Devey, and S. Kutterolf (2012), Doing fieldwork on the seafloor: Photogrammetric techniques to yield 3D visual models from ROV video, *Computers & Geosci.*, 52, 218-226, https://doi.org/10.1016/j.cageo.2012.10.008.

Kwasnitschka, T., K. Köser, J. Sticklus, M. Rothenbeck, T. Weiß, E. Wenzlaff, T. Schoening, L. Triebe, A. Steinführer, C. Devey and J. Greinert (2016), DeepSurveyCam - A Deep Ocean Optical Mapping System, *Sensors*, 16(2), https://doi:10.3390/s16020164.

Li, S., K. Wang, Y. Wang, Y. Jiang, and S. E. Dosso (2018), Geodetically inferred locking state of the Cascadia megathrust based on a viscoelastic Earth model, *J. of Geophys. Res.: Solid Earth*, 123(9), 8056-8072, https://doi.org/10.1029/2018JB015620.

McCrory, P. A., J. L. Blair, F. Waldhauser, and D. H. Oppenheimer (2012), Juan de Fuca slab geometry and its relation to Wadati-Benioff zone seismicity, *J. of Geophys. Res.: Solid Earth*, 117(B9), https://doi.org/10.1029/2012JB009407.

Nelson, A. R., H. M. Kelsey, and R. C. Witter (2006), Great earthquakes of variable magnitude at the Cascadia subduction zone, *Quat. Res.*, 65(3), 354-365, https://doi.org/10.1016/j.yqres.2006.02.009.

Nishimagi, Y., Y. Ohta, R. Hino, S. Suzuki, M. Sato, H. Kajikawa, and T. Kobata (2018), Quantitative assessment of the “A-0-A” method based on the laboratory experiments: toward the accurate long-term OBP sensor drift estimation, Abstract T41F-0368 presented at the 2018 AGU Fall Meeting, Washington, D. C., 10-14 Dec.

Nooner, S. L., and W. W. Chadwick Jr. (2016), Inflation-predictable behavior and co-eruption deformation at Axial Seamount, *Science*, 354(6318), 1399-1403, https://doi.org/10.1126/science.aah4666.

Nooner, S. L., and W. W. Chadwick Jr. (2009), Volcanic inflation measured in the caldera of Axial Seamount: Implications for magma supply and future eruptions, *Geochem. Geophys. Geosyst.*, 10(2), https://doi.org/10.1029/2008GC002315.

Okaji, M., H. and Imai (1984), A practical measurement system for the accurate determination of linear thermal expansion coefficients. *J. of Phys. E: Sci. Instr.*, 17(8), 669, https://doi.org/10.1088/0022-3735/17/8/011.

Paros, J. M., and T. Kobayashi (2015a), Mathematical Models of Quartz Sensor Stability, Tech. Note G8095, Paroscientific Inc., Redmond, Wash.

Paros, J. M., and T. Kobayashi (2015b), Root Causes of Quartz Sensor Drift, Tech. Note G8101, Paroscientific Inc., Redmond, Wash.

Pavlis, N. K., S. A. Holmes, S. C. Kenyon, and J. K. Factor (2012), The development and evaluation of the Earth Gravitational Model 2008 (EGM2008), *J. Geophys. Res.*, 117, B04406, https://doi.org/10.1029/2011JB008916.

Pawlowicz, R., B. Beardsley, and S. Lentz (2002), Classical tidal harmonic analysis including error estimates in MATLAB using T_TIDE, *Comp. and Geosci.*, 28(8), 929-937, https://doi.org/10.1016/S0098-3004(02)00013-4.

Piecuch, C. G., I. Fukumori, R. M. Ponte, and O. Wang (2015), Vertical structure of ocean pressure variations with application to satellite-gravimetric observations, *J. Atmos. And Oceanic Tech.,* 32(3), 603-613, https://doi.org/10.1175/JTECH-D-14-00156.1.

Poland, M. P., A. Miklius, A. J. Sutton, and C. R. Thornber (2012), A mantle-driven surge in magma supply to Kilauea Volcano during 2003– 2007, *Nat. Geosci.*, 5, 295–300, https://doi.org/10.1038/NGEO1426.

Polster, A., M. Fabian, and H. Villinger (2009), Effective resolution and drift of Paroscientific pressure sensors derived from long-term seafloor measurements, *Geochem. Geophys. Geosyst.*, 10, Q08008, https://doi.org/10.1029/2009GC002532.

Sasagawa, G., and M. A. Zumberge (2013), A self-calibrating pressure recorder for detecting seafloor height change, IEEE *J. of Ocean. Eng.,* 38(3), 447-454, https://doi.org/10.1109/JOE.2012.2233312.

Sasagawa, G., M. J. Cook, and M. A. Zumberge (2016), Drift-corrected seafloor pressure observations of vertical deformation at Axial Seamount 2013–2014, *Earth and Space Science*, 3(9), 381-385, https://doi.org/10.1002/2016EA000190.

Sasagawa, G. S., M. A. Zumberge, and M. J. Cook (2018), Laboratory Simulation and Measurement of Instrument Drift in Quartz-Resonant Pressure Gauges, *IEEE Access*, 6, 57334-57340, https://doi.org/10.1109/ACCESS.2018.2873479.

Savage, J. C. (1995), Interseismic uplift at the Nankai subduction zone, southwest Japan, 1951–1990, J. *Geophys. Res.: Solid Earth*, 100(B4), 6339-6350.

Schmalzle, G. M., R. McCaffrey, and K. C. Creager (2014), Central Cascadia subduction zone creep, *Geochem. Geophys. Geosyst.*, 15(4), 1515-1532, https://doi.org/10.1002/2013GC005172.

Segawa, J., and H. Fujimoto (1988), Observation of an ocean bottom station installed in the Sagami Bay and replacement of the acoustic transponder attached to it, *JAMSTECTR Deepsea Research*, 256.

Spiess, F. N., C. D. Chadwell, J. A. Hildebrand, L. E. Young, G. H. Purcell Jr, and H. Dragert (1998), Precise GPS/Acoustic positioning of seafloor reference points for tectonic studies. *Physics of the Earth and Planetary Interiors*, 108(2), 101-112, https://doi.org/10.1016/S0031-9201(98)00089-2.

Stenvold, T., O. Eiken, M. A. Zumberge, G. S. Sasagawa, and S. L. Nooner (2006), High-precision relative depth and subsidence mapping from seafloor water pressure measurements, *SPE Journal*, 11(03), 380-389, https://doi.org/10.2118/97752-PA.

Thomas, A. L. (1993), Poly3D: A Three-Dimensional, Polygonal Element, Displacement Discontinuity Boundary Element Computer Program with Applications to Fractures, Faults, and Cavities in the Earth's Crust, Stanford University, Stanford, CA.

Wallace, L. M., S. C. Webb, Y. Ito, K. Mochizuki, R. Hino, S. Henrys, S. Y. Schwartz, and A. F. Sheehan, (2016), Slow slip near the trench at the Hikurangi subduction zone, New Zealand, *Science*, 352(6286), 701-704, https://www.doi.org/10.1126/science.aaf2349.

Watkins, M. M., D.N. Wiese, D.-N. Yuan, C. Boening, and F.W. Landerer (2015), Improved methods for observing Earth's time variable mass distribution with GRACE using spherical cap mascons, *J. Geophys. Res. Solid Earth*, 120, 2648–2671, https://doi:10.1002/2014JB011547.

Watts, D. R., and H. Kontoyiannis (1990), Deep-ocean bottom pressure measurement: Drift removal and performance, *J. of Atmos. and Ocea. Tech.*, 7(2), 296-306, https://doi.org/10.1175/1520-0426(1990)007%3C0296:DOBPMD%3E2.0.CO;2.

Westoby, M. J., J. Brasington, N. F. Glasser, M. J. Hambrey, and J. M. Reynolds (2012), 'Structure-from-Motion' photogrammetry: a low-cost, effective tool for geoscience applications, *Geomorphology*, 179(2012), 300-314, https://doi.org/10.1016/j.geomorph.2012.08.021.

Wilcock, W. S. D., D. A. Manalang, M. J. Harrington, G. Cram, E. K. Frederickson, J. Tilley, J. Burnett, D. Martin, J. M. Paros, and T. Kobayashi (2018), Self-Calibrating Resonant Quartz Crystal Technology Sensors for Seafloor Geodesy and Oceanographic Applications, Abstract OS21E-1615 presented at 2018 AGU Fall Meeting, Washington, D. C., 10-14 Dec.

Wirth, E. A., A. D. Frankel, N. Marafi, J. E. Vidale, and W. J. Stephenson (2018), Broadband synthetic seismograms for magnitude 9 earthquakes on the Cascadia megathrust based on 3D simulations and stochastic synthetics, Part 2: Rupture parameters and variability, *Bull. of the Seis. Soc. of Am.*, 108(5A), 2370-2388, https://doi.org/10.1785/0120180029.

Zumberge, M. A., and E. L. Canuteson (1995), An ocean bottom absolute gravity meter, *Gravity and Geoid*, 7-16, Springer, Berlin, Heidelberg.

Zumberge, M. A., H. Alnes, O. Eiken, G. S. Sasagawa, and T. Stenvold (2008), Precision of seafloor gravity and pressure measurements for reservoir monitoring, *Geophysics*, 73(6), WA133-WA141, https://doi.org/10.1190/1.2976777.

Zumberge, M. A., W. Hatfield, and F. K. Wyatt (2018), Measuring Seafloor Strain with an Optical Fiber Interferometer, *Earth and Space Science*, 5(8), 371-379, https://doi.org/10.1029/2018EA000418.